

CATALOGED BY ASTIA 402360  
AS AD NO.

ARL 62-360

Part I

402 360

## FEASIBILITY OF A SOLAR ENERGY DEVICE

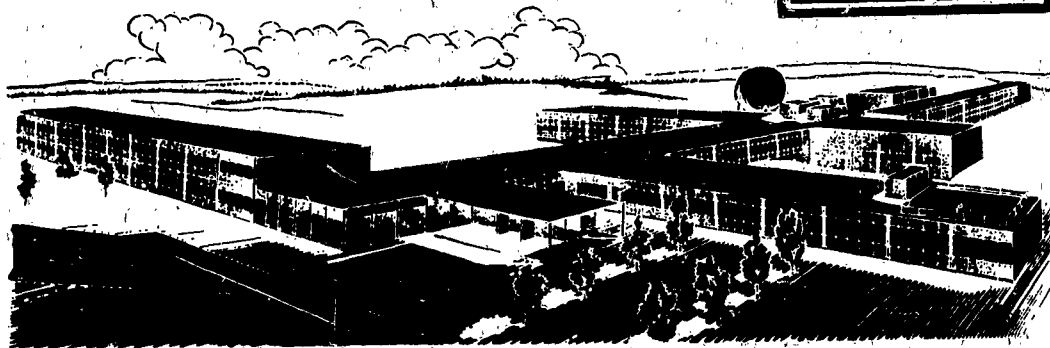
### Part I: DESIGN AND PERFORMANCE CONSIDERATIONS

FREDERIC E. FULLER

ELECTRO-OPTICAL SYSTEMS, INC.  
PASADENA, CALIFORNIA

JUNE 1962

AERONAUTICAL RESEARCH LABORATORIES  
OFFICE OF AEROSPACE RESEARCH  
UNITED STATES AIR FORCE



## NOTICES

When Government drawings, specifications, or other data are used for any purpose other than in connection with a definitely related Government procurement operation, the United States Government thereby incurs no responsibility nor any obligation whatsoever; and the fact that the Government may have formulated, furnished, or in any way supplied the said drawings, specifications, or other data, is not to be regarded by implication or otherwise as in any manner licensing the holder or any other person or corporation, or conveying any rights or permission to manufacture, use, or sell any patented invention that may in any way be related thereto.

- - - - -

Qualified requesters may obtain copies of this report from the Armed Services Technical Information Agency, (ASTIA), Arlington Hall Station, Arlington 12, Virginia.

- - - - -

This report has been released to the Office of Technical Services, U. S. Department of Commerce, Washington 25, D. C. for sale to the general public.

- - - - -

Copies of ARL Technical Documentary Reports should not be returned to Aeronautical Research Laboratory unless return is required by security considerations, contractual obligations, or notices on a specific document.

**ARL 62-360**

**Part I**

# **FEASIBILITY OF A SOLAR ENERGY DEVICE**

## **Part I: DESIGN AND PERFORMANCE CONSIDERATIONS**

**FREDERIC E. FULLER  
ELECTRO-OPTICAL SYSTEMS, INC.  
PASADENA, CALIFORNIA**

**JUNE 1962**

**CONTRACT AF 33(616)-5977  
PROJECT 7116  
TASK 7116-02**

**AERONAUTICAL RESEARCH LABORATORIES  
OFFICE OF AEROSPACE RESEARCH  
UNITED STATES AIR FORCE  
WRIGHT-PATTERSON AIR FORCE BASE, OHIO**

## FOREWORD

This report was prepared by Electro-Optical Systems, Inc, Pasadena, California on Air Force Contract AF 33(616)-5977 under Task No. 7116-02, "Research in Energy Conversion Techniques", of Project No. 7116, "Energy Conversion Research". The contract was monitored by Messrs. Ken Vickers and E. D. Stephens, of the Aeronautical Research Laboratories.

The investigation began 6 June 1958 and was accomplished by the Advanced Power Systems Division of EOS.

In its first phase, as reported in WADC TN59-184, the work was done by Mr. Donald H. McClelland, Project Supervisor under the direction of Dr. J. H. Fisher, Division Manager. In its second phase, as reported here, the work was done by Dr. Frederic E. Fuller, Project Supervisor under the direction of Mr. Donald H. McClelland, Manager, Energy Conversion and Regulation Department. This is the final report of the second phase of this investigation.

The research reported herein is exploratory. The concept treated was first proposed by Mr. Elmer Johnson of ARL and was reported in WADC TR 56-182 by Mr. Robert Hunter.

# **ABSTRACT**

The feasibility of a solar powered aircraft is investigated. The configuration reached is a high aspect ratio flying wing with ramjet thrust. A statement is made with respect to feasibility with a recommendation of a program for further work. The statement of feasibility is supported by experimental investigation of solar radiation collection and inlet air diffusion and finally by design and performance analyses.

## CONTENTS

1.	INTRODUCTION	1
2.	THE AIRCRAFT CONFIGURATION	2
3.	THE AIRCRAFT FLIGHT CONDITIONS	4
4.	INTRODUCTORY DISCUSSION OF THE AIRCRAFT PERFORMANCE	5
5.	THE PLAN AND BASIS FOR THE AIRCRAFT PERFORMANCE CALCULATIONS	8
6.	PRIOR DESIGN AND PERFORMANCE ANALYSIS OF THE SOLAR POWERED AIRCRAFT	11
7.	RESULTS OF SOLAR POWERED AIRCRAFT DESIGN AND PERFORMANCE ANALYSIS	12
8.	VALIDITY OF THE RESULTS OF PERFORMANCE ANALYSIS	14
9.	THE UNSYMMETRICAL TWO-SHOCK INLET DIFFUSER	15
10.	ELEMENTARY CONSIDERATIONS OF TOTAL THRUST AND REYNOLDS ANALOGY	16
	10.1 Discussion of the Total Thrust	16
	10.2 Relation Between Pressure Loss and Heat Transfer	17
11.	DEVELOPMENT OF METHOD OF ANALYSIS	18
	11.1 Performance of the Radiation Collector Heat Transfer Section	18
	11.1.1 The Equations of Energy Flux in the Collector-Transfer Section	18
	11.1.2 Radiant Energy Transfer in the Collector-Transfer Section	19
	11.1.3 The Temperature Change Along the Internal Stream	23
	11.1.4 One Dimensional Channel Flow in the Radiation Collector-Heat Transfer Section	24

## CONTENTS (cont)

11.1.5	Heat Flux by Convection from the Collector-Transfer Foils to the Internal Stream	25
11.1.6	Momentum Transfer Between Collector-Transfer Foils and the Internal Stream	26
11.1.7	Estimation of the Momentum and Convective Heat Transfer of the Collector-Transfer Section Walls to the Internal Stream	27
11.1.8	Heat Transfer from Upper and Lower Wing Surfaces to the External Stream	28
11.1.9	The Performance Equations of the Collector-Transfer Section	30
11.2	Performance of the Inlet Diffuser	42
11.3	Design of the Jet Nozzle and the Determination of Net Thrust	43
11.4	Estimation of the Drag of the Wing External Surface	44
11.5	Determination of Lengths of Inlet Diffuser, Collector-Transfer and Jet Nozzle Section for Maximum $w/x_c$	47
12.	PERFORMANCE ANALYSIS SEQUENCE	50
13.	SOLAR ENERGY COLLECTION	68
13.1	General Characteristics of Solar Energy Collectors	68
13.2	Spectrally Selective Surfaces	72
13.2.1	Theoretical Discussion	74
13.2.2	Description and Preparation of Surfaces	78
13.2.3	Spectral Evaluation of Surfaces	91
13.2.4	Conclusions Regarding Suitability of Surfaces	101
13.3	Radiation Traps	102
13.3.1	Energy Losses from Geometric Radiation Traps	103
13.3.2	Laboratory Test Traps	106
13.4	Interference Filters	111
13.4.1	Literature Survey	111
13.4.2	Theory of Thin Film Interference Filters	112
13.4.3	Three-Layer Film	113
14.	CONCLUSIONS AND RECOMMENDATIONS	115
	REFERENCES	116

## ILLUSTRATIONS

### Tables

I	Flight conditions for twenty-four hour earth satellite solar powered aircraft	118
II	Input data for performance computations	119
III	Summary of results of performance computations	120
IV	Comparison of properties for the best opaque spectrally selective surfaces	121

### Figures

1	Solar powered aircraft configuration - wing cross section (Secret)	122
2	Wing loading vs altitude for various values of chord length (from TN 59-184)	122
3a	Solar powered aircraft configurations (wing cross sections)	123
3b	Solar powered aircraft configurations (wing cross sections)	123

### Notation for Figures 4 through 15

4	Details of performance computation results, Case I	125
5	Details of performance computation results, Case II	125
6	Details of performance computation results, Case III	126
7	Details of performance computation results, Case IV	126
8	Details of performance computation results, Case V	127
9	Details of performance computation results, Case VI	127
10	Details of performance computation results, Case VII	128
11	Details of performance computation results, Case VIII	128
12	Details of performance computation results, Case X	129
13	Details of performance computation results, Case XI	129
14	Details of performance computation results, Case XII	130
15	Details of performance computation results, Case XIII	130

### Notation for Figures 16 through 19

16	Details of performance computation results, Case XIV	132
----	------------------------------------------------------	-----



## ILLUSTRATIONS (cont)

Figures		
17	Energy flux details, Case VIII	132
18	Energy flux details, Case XI	133
19	Energy flux details, Case XII	133
20	Inlet diffuser configuration	134
21	Arrangement of radiation collector-heat transfer foils in the collector-transfer section	134
22	Elementary radiation collector consisting of infinite parallel surfaces	135
23	Radiant energy exchange between infinite parallel surfaces	135
24	"Green House" effect between infinite parallel surfaces	135
25	Air, viscosity	136
26	Air, thermal conductivity	136
27	Air, Prandtl number	137
28	Absorption-emission characteristics of solar energy absorbing surfaces	137
29	Trapping efficiency (f) vs cutoff wavelength ( $\lambda_c$ ) for an ideal collector	138
30	Sprayed coatings are evenly applied to test samples by use of cam-oscillated nozzle and traveling hot-plate	138
31	Comparison of various types of black surfaces	139
32	Reflectance of Nesa glass, 0.25 $\mu$ -14 $\mu$ (Sample No. P-6)	139
33	Transmittance of Nesa glass, 0.25 $\mu$ -14.0 $\mu$ (Sample P-6)	140
34	Transmission characteristic of gold smoke filters	140
35	Optimum emissivity vs absorptivity reference	141
36	Transmittance of Pyrex and Nesa glass	141
37	Cupric oxide on aluminum by the Unger process	142
38	Cupric oxide on aluminum prepared by Thomas A. Unger	142
39	Reflectance of uncoated aluminum	143
40	Spectral response of cupric oxide on copper by the "Ebonol" process	143

## ILLUSTRATIONS (cont)

### Figures

41	Black nickel-iron oxide on steel by the "nickel penetrate" process	144
42	Black nickel on copper	144
43	Black nickel on copper showing the extremes in spectral characteristic $0.35\mu$ - $13\mu$	145
44	Black nickel on nickel and nickel-plated copper	145
45	Platinum black on platinum	146
46	Carbon black on aluminum	146
47	Reflectance of Nesa and Corning glass	147
48	Reflectance of Nesa glass	147
49	Transmittance of Nesa glass, thickness $1/8"$	148
50	Transparent surfaces	148
51	Fresnel lens and NESA-glass radiation traps fit into test frame for mounting in solar test facility	149
52	Solar collector characteristic for space application	149
53	Three-layer interference filter	150

## NOMENCLATURE

### English Letters

$A, A_{()}$	Duct area ( $\text{ft}^2$ )
$a$	Sonic velocity ( $\text{ft}/\text{sec}$ )
$C_{()}, C_{()()}$	(With literal subscripts) Convective heat transfer rate ( $\text{ft lbs}/\text{sec ft}$ )
$C_{()}$	(With numerical subscripts) Various constants defined in Section 12.8
$C_D$	Drag coefficient
$C_{Da}$	Allowable drag coefficient
$C_{Df}$	Friction drag coefficient
$C_{Do}$	Zero lift drag coefficient
$C_{Dp}$	Pressure drag coefficient
$C_L$	Lift coefficient
$C_P$	Specific heat at constant pressure ( $\text{ft lbs}/\text{slug } ^\circ\text{R}$ )
$C_V$	Specific heat at constant volume ( $\text{ft lbs}/\text{slug } ^\circ\text{R}$ )
$D$	Drag per unit span ( $\text{lbs}/\text{ft}$ )
$F$	Thrust per unit span ( $\text{lbs}/\text{ft}$ )
$f_{()}$	(With numerical subscripts) Various functions defined in Section 12.9
$g$	Local acceleration due to gravity ( $\text{ft}/\text{sec}^2$ )
$h$	Local heat transfer coefficient ( $\text{ft lbs}/\text{ft}^2 \text{ sec } ^\circ\text{R}$ )
$k$	Thermal conductivity ( $\text{ft lbs}/\text{ft sec } ^\circ\text{R}$ )
$L$	Lift per unit span, $\text{lbs}/\text{ft}$

# NOMENCLATURE (cont)

$l_{()}$	(With numerical subscripts) Certain lengths defined in Section 11.5
M	Mach number
$\bar{m} (M)$	Mass flow function
m	Hydraulic radius, ft.
$N_R$	Reynolds number
$(N_{R/x})_{()}$	Reynolds number per foot ( $ft^{-1}$ )
$(N_P)_{()}$	Prandtl number
P	Pressure ( $lbs/ft^2$ )
Q	Total heat transfer rate per unit span to the internal airstream ( $ft\ lbs/sec\ ft$ )
$q_{()}, q_{()()}$	Radiative heat fluxes defined in Section 11.1.1 ( $ft\ lbs/sec\ ft$ )
q	Free stream dynamic pressure ( $lbs/ft^2$ )
R	Radiative heat loss ( $ft\ lbs/sec\ ft$ )
$R_{()}, R_{()()}$	Total temperature and total pressure performance ratios
S	Sutherland constant = $216^{\circ}R$
T	Temperature ( $^{\circ}R$ )
v	Velocity ( $ft/sec$ )
w	Aircraft weight per unit span ( $lbs/ft$ )
x	Chordwise coordinate ( $ft$ )
$x_f$	Length of collector-transfer foil ( $ft$ )
$x_p$	Length of collector Fresnel lens ( $ft$ )
y	Vertical coordinate ( $ft$ )
Z	Altitude above sea level, ft

## NOMENCLATURE (cont)

### Greek Letters

$\alpha$	Angle of attack
$\alpha_{()}()$	Radiation absorptivity
$\Gamma_{()}()$	Constants defined in Section 11.4
$\gamma_{()}()$	Functions defined in Sections 11.1.5 and 11.1.8
$\gamma$	Ratio of specific heats = $C_p/C_v$
$\Delta, \delta$	Small variation
$\epsilon$	Thermal emissivity
$\eta_o$	Fraction percent of incident solar radiation absorbed by the collector-transfer foils
$\theta$	Semi-divergence angle of the subsonic diffuser
$\lambda_{()}()$	Characteristic radiation
$\lambda$	Lagrange multiplier
$\mu_{()}()$	Air viscosity (lb sec/ft <sup>2</sup> )
$\rho_{()}()$	Air density (slug/ft <sup>3</sup> )
$\rho_{()}()$	Radiation reflectivity
$\tau_{()}()$	Radiation fraction percent transmitted
$\sigma$	Stefan-Boltzmann constant = $374 \times 10^{-12}$ (ft lb/sec °R <sup>4</sup> )

### Subscripts

### English Letters

a	Allowable
c	Chord
d	Diffuser
e	Boundary layer stagnation condition
ext	Exterior
f	Collector-transfer foil

## NOMENCLATURE (cont)

h	Collector-transfer section
i, j	Integers
int.	Interior
l	Lower wing surface
n	Jet nozzle section
opt.	Optimum
P	Pressure
s	Solar
T	Temperature
u	Upper wing surface
w	Wall

### Greek Letters

$\lambda_{()}$	Characteristic radiation
----------------	--------------------------

### Numbers

1, 1t, 2, 3, 4, 4t Chord stations shown in Fig. 2

### Superscripts

\* Dimensionless ratio defined in Section 12.9

## 1. INTRODUCTION

The use of solar energy as a power source has always been intriguing because of its inexhaustibility. Since the advent of the space flight concept, scientists and engineers have sought methods for adapting the solar source of radiant energy to the propulsion of spacecraft. In recent years, another concept has gained consideration - the solar powered aircraft.

The application of solar energy to aircraft propulsion is particularly interesting, because it would make possible a device that could circle the earth continuously, in the same manner as a satellite, only at a much lower altitude and velocity. The fundamental object of research and development conducted under this contract was to investigate problems concerning the feasibility of flight, employing a solar powered ramjet.

This report is in three major parts; the experimental investigation of radiation trapping, the experimental investigation of the subsonic part of the inlet air diffusion, and finally, the design and performance analysis development. These investigations are brought to culmination in a statement on the technical feasibility of the solar powered aircraft. A recommendation is offered for the direction of further investigation.

The experimental investigation of radiation trapping is reported in Section 13 of Part I. The material of this section has been directly transferred from WADC TN59-184 for ready reference. The experimental investigation of the inlet diffuser is reported in Part II. In Sections 2 through 13 of Part I, is presented the solar powered aircraft design development and performance analysis with configurations and estimated performance all in support of the feasibility statement and the recommendation for further investigation.

---

Manuscript released by author 14 April 1961 for publication as an ARL Technical Report

## 2. THE AIRCRAFT CONFIGURATION

The configuration of the solar powered aircraft as developed in this study is shown on Figure 1. This particular configuration emerged in the course of the work on the basis of the following considerations:

1. High wing span to chord length aspect ratio.
2. High Reynolds number based on flight speed, the wing chord length, and the free stream air viscosity.
3. High ratio of area of solar beam cross-section to wing area.
4. Optimum areas of the internal stream and of the free stream entering the internal stream.
5. Optimum compromise of pressure loss in the internal stream with lift and pressure drag in the external stream.
6. The two-shock, unsymmetrical supersonic diffuser.
7. The diagonal array of heat transfer elements in the internal stream.
8. The spectrally selective surfaces: upper wing surfaces, both inner and outer; the lower wing surface, both inner and outer and the heat transfer foils.

The high aspect ratio and Reynolds number tend toward low induced and friction drags, respectively. The high ratio of solar radiation beam cross-section to wing area tends toward maximum power loading. The use of the entire span of the wing leading edge for inlet to the internal stream yields maximum internal airflow consistent with the drag of the external stream. As will be discussed later, this choice may not be optimum with respect to pressure loss in the internal stream. By use of the maximum cross-section of the internal stream otherwise consistent with the external drag and the internal pressure loss, the pressure loss due to heat transfer is minimized. In Sections 10.1 and 10.2 analyses are presented in support of the last two points: the first of these, based on a consideration of propulsive efficiency, suggests including the percent of span to be used as diffuser inlet width as a design parameter; the second of these, based on a consideration of the Reynolds analogy, confirms the choice of maximum internal stream cross-section.

With respect to the compromise of pressure losses in the internal stream with lift and drag in the external stream: these effects are



critically dependent on the length and slopes of the upper and lower wing surfaces. In the design analysis, the lengths and slopes of the inlet diffuser, the heat transfer and jet nozzle section are determined for maximum wing loading of the aircraft.

The advantages of the two-shock unsymmetrical supersonic diffuser are discussed in Section 9. These advantages are: a high pressure recovery in the supersonic diffuser and the delivery of the inlet airstream to the subsonic diffuser entrance with minimum disturbance of the internal and external streams.

The diagonal array of heat transfer elements in the internal stream permits intercepting the solar beam by equal or greater area of absorbing surface but with both foil lengths and diagonal spacing available to be determined for best design. Of course, as the diagonal spacing varies the slope of the diagonals also varies accordingly.

The spectrally selective surfaces serve to trap solar radiation energy within the aircraft wing where it is delivered to the internal stream. The spectrally selective surfaces are used as follows:

1. A "green house effect" on the wing upper surface where the wing upper surface has high transmittance for solar radiation and high reflectance for the characteristic thermal radiation of the heat transfer foils.
2. Heat transfer foils with high absorptivity for the solar radiation and low emissivity for their characteristic thermal radiation.
3. Wing inner surfaces highly reflective to the heat transfer foil characteristic thermal radiation.
4. Wing outer surfaces of low emissivity for their own characteristic thermal radiation.

### 3. THE AIRCRAFT FLIGHT CONDITIONS

The flight conditions most favorable for feasibility were chosen. These conditions are determined by the requirements: first, that the sun be directly overhead the aircraft, and second, that the altitude be optimum.

Conditions of a 24 hour period earth satellite at constant altitude are given in Table I. The atmospheric properties used are given in Ref. 1, the ARDC Model Atmosphere. In Table I, the quantities of special interest are:

$Z$  = altitude

$M$  = aircraft flight Mach number

$v/v_1$  = aircraft flight Reynolds number per foot.

$\left(\frac{v}{v}\right)_2$  = Reynolds number per foot of the internal flow at the diffuser outlet.

The aircraft optimum performance and configuration depend critically on the flight altitude.

#### 4. INTRODUCTORY DISCUSSION OF THE AIRCRAFT PERFORMANCE

The aircraft configuration is shown in Fig. 1 and a summary discussion of the basis for the choice of this configuration is given in Section 2. In the following, an elementary discussion of the aircraft flight processes will be given.

The vector sum of all the surface normal and tangential forces over the exterior and interior surface of the aircraft yield the usual equations for the equilibrium of lift, total weight, drag and net thrust. The net thrust is, by definition, the vector sum of all aerodynamic forces on the interior surfaces of the aircraft; the net thrust is also the equal and opposite of the net change of momentum of the internal stream.

Let us consider now three streams of airflow: one over the upper surface of the wing, another the internal stream, and third, the flow over the lower surface of the wing. The internal stream after passing through an oblique shock attached to the leading edge of the upper wing surface and through a normal shock just upstream of the leading edge of the lower wing surface arrives at the entrance of the subsonic diffuser with but small total pressure loss. The internal flow enters the subsonic diffuser with a disturbance on the upper surface due to the boundary layer and the normal shock, and a disturbance on the lower surface due to the vorticity of a curved normal shock. The process of subsonic diffusion has these notable features: the aforementioned disturbances at the inlet, the low Reynolds number of the flow and the low divergence angle and long lengths of the diffuser channel. The divergence angle and length of the diffuser channel is the result of the compromise in the design for maximum wing loading between wing profile drag and diffuser pressure loss on the one hand, and increased lift and decreased wing pressure drag on the other hand. The wing profile drag, the diffuser pressure loss and the wing lift increase with diffuser length; the wing pressure drag decreases as the diffuser section divergence angle decreases. The internal stream arrives at the entrance of the heat transfer section with vorticity and turbulence due to upstream flow conditions and including, in particular, the boundary layer effects in the diffuser. It is expected that due to the low Reynolds number of the diffuser flow and the low divergence angle of the diffuser channel that separation will not occur.

In the heat transfer section there is pressure loss due to heat transfer, somewhat according to the Reynolds analogy. There is also a pressure loss due to heating, accordingly as the flow is accelerated with decreasing density. Both of these effects increase sharply with increase of Mach number. The Mach number of the heat transfer section flow as a function of distance along the heat transfer section is critically dependent on the diffuser section outlet Mach number. The diffuser section outlet Mach number is most critically dependent in this case, on the diffuser outlet to inlet area ratio. This ratio of areas also effects the divergence angle and length of the diffuser section. Besides the pressure loss in the heat transfer section at the heat transfer foils due to heat transfer and accelerated flow, there is the pressure loss at the channel walls. This pressure loss also increases with the local Mach number.

The rate at which the Mach number increases along the heat transfer channel and hence the rate at which pressure loss occurs with friction and heat addition depends critically on the length of the heat transfer foils and the divergence angle of the heat transfer section. The effect of the divergence angle is that of subsonic diffusion. The shorter the heat transfer foil, the higher the heat transfer coefficient but also the higher the drag coefficient. There exists, however, for each design case an optimum combination of heat transfer channel divergence and heat transfer foil length for the compromise of pressure drag in the external stream and pressure loss in the internal stream with heat transfer in the internal stream.

The optimum length of the heat transfer section is reached when with the increase of the internal stream Mach number and with the increase of the internal stream and heat transfer-foil temperatures the rates of internal stream pressure loss and rate of radiation loss from the aircraft are so large that no increase of wing loading occurs with increase of heat transfer section lengths.

The areas of the jet nozzle throat and outlet are determined by the stream conditions at the entrance of the jet nozzle throat and by the requirement that the static pressure in the jet at the outlet be equal to the atmospheric pressure.

This requirement, to a good approximation for the condition of the solar powered aircraft jet, determines the nozzle areas for maximum thrust. The length of the jet nozzle section is determined for optimum wing loading by a compromise of wing pressure and profile drags with the internal stream pressure loss. The dominant effect is sufficient length and hence sufficiently small divergence angle that the pressure drag in the external stream is small. It appears as is demonstrated in the section on the results of design and performance calculation that the need for small pressure drag in the external stream is so severe that the divergence angles of both the subsonic diffuser and the jet nozzle sections are far smaller than optimum for the internal stream flow.

The problem of the design and performance of the wing in the external stream for the upper surface is familiar and likewise for the lower surface except for the spillage flow from the subsonic diffuser at the leading edge.

A detailed account is given in the following of the derivation with assumptions and approximations, of the method of design and performance analysis.

## 5. THE PLAN AND BASIS FOR THE AIRCRAFT PERFORMANCE CALCULATIONS

The aim of this analysis is to determine a valid estimate of the performance of a solar powered aircraft. The simplifying assumptions and approximations made in this analysis are designed for either negligible error or for small over-estimation of performance. The performance estimated will be the performance at best. The purpose of the performance calculations is to provide a basis for a definitive statement of the feasibility of a solar powered aircraft.

The configuration on which this analysis is based is shown in Fig. 1 and is discussed in Section 2. The flight conditions of the aircraft for this analysis are shown on Table I and are discussed in Section 3. The processes by which the aircraft flies are discussed in elementary terms in Section 4.

For convenience the aircraft is considered in three major parts: the inlet diffuser from Station 1 to Station 2, the radiation collector-heat transfer section from Station 2 to Station 3, and finally, the jet nozzle section from Station 3 to Station 4. The diffuser section is considered in two parts: a supersonic diffuser from Station 1 to Station 1t and a subsonic part from Station 1t to Station 2.

The physical basis and major assumptions of the aircraft performance analysis are as follows:

1. The aircraft basic configuration
2. The aircraft flight conditions
3. Estimated pressure recovery ratios for the supersonic and subsonic diffusers.
4. The averages of the flow conditions along the collector-transfer section are computed as if the flow were one-dimensional.
5. The pressure loss and heat transfer at the heat transfer foils are estimated by flat plate laminar boundary theory.

6. The pressure loss and heat transfer at the internal channel walls are estimated by assuming the boundary layers to be just at transition from laminar to turbulent.
7. The profile drag and heat transfer in the external stream at the wing upper and lower surfaces are estimated by assuming the boundary layers to be laminar.
8. The pressure drag of the wing in the external stream is computed by the Busemann theory.
9. A simplified model is adopted for the analysis of the radiant heat transfer to and from the heat transfer foils. By means of this theory and the optical properties of the various surfaces involved a performance method is evolved for the estimation of the radiant heat transfer.
10. Estimated pressure recovery ratio for the jet nozzle.

These physical bases and major assumptions are adopted for the purpose of estimating the best performance of the aircraft which may be expected.

The critical item of performance sought is the attainable wing loading

$$\left( \frac{w}{x_c} \right)_a$$

The performance analysis method is derived in Section 11.

The performance analysis sequence of computations is given in Section 12.

Briefly, the analysis procedure is:

1. Choose the input data

Z	=	flight altitude
y <sub>1</sub>	=	inlet diffuser inlet height
b	=	percent of span to be used as diffuser width
R <sub>pd</sub>	=	diffuser pressure recovery ratio
R <sub>ps</sub>	=	jet pressure recovery ratio
M <sub>2</sub>	=	collector-transfer section inlet Mach number

$y/y_2$  = collector-transfer section divergence function

$x_f/y$  = heat transfer foil chord length ratio

and the quantities  $\eta_0$ ,  $E_{ff}$ ,  $E_{uu}$ ,  $E_{ll}$ ,  $E_{uf}$ ,  $E_{lf}$ ,  $E_{su}$  which refer to the radiation transmitting, reflecting, absorbing and emitting properties of the heat transfer foils and the inner and outer surfaces of the aircraft.

2. Proceed with the operations of the analysis sequence in Section 12. These operations yield, besides much detailed information, the dimensions  $y_2$ ,  $y_3$ ,  $y_4$  and  $x_c$  as well as the dimensional ratios  $l_1/x_c$ ,  $l_2/x_c$ ,  $l_3/x_c$ , all with the performance results: the excess thrust coefficient

$\left\{ \frac{F}{q x_c} - C_D \right\}$  and the attainable wing loading  $\left( w/x_c \right) a$ . The dimensions and dimensional ratios are determined for the maximum value of the wing loading  $\left( w/x_c \right) a$ .

3. Repeat step (2) for various values of  $M_2$ ,  $y/y_2$ ,  $x_f/y$ , and  $b$  until the set of these is determined for maximum wing loading  $\left( w/x_c \right) a$ .

4. Repeat steps (2) and (3) for various altitudes until the altitude is determined for the maximum wing loading,  $\left( w/x_c \right) a$ .

The validity of these results of performance computation depend critically on the validity of the data: the diffuser and jet recovery ratios,  $R_{pd}$  and  $R_{pj}$ , the radiant energy transfer parameters  $\eta_0$ ,  $E_{ff}$ ,  $E_{uu}$ ,  $E_{ll}$ ,  $E_{uf}$ ,  $E_{lf}$ , and  $E_{su}$  and on the validity of the physical basis and assumptions (4), (5), (6) and (7) which determine the estimates of heat and momentum transfers to the internal stream in the collector-transfer section and to the external stream on the upper and lower wing surfaces.



6. The pressure loss and heat transfer at the internal channel walls are estimated by assuming the boundary layers to be just at transition from laminar to turbulent.
7. The profile drag and heat transfer in the external stream at the wing upper and lower surfaces are estimated by assuming the boundary layers to be laminar.
8. The pressure drag of the wing in the external stream is computed by the Busemann theory.
9. A simplified model is adopted for the analysis of the radiant heat transfer to and from the heat transfer foils. By means of this theory and the optical properties of the various surfaces involved a performance method is evolved for the estimation of the radiant heat transfer.
10. Estimated pressure recovery ratio for the jet nozzle.

These physical bases and major assumptions are adopted for the purpose of estimating the best performance of the aircraft which may be expected.

The critical item of performance sought is the attainable wing loading

$$\left( \frac{w}{x_c} \right)_a$$

The performance analysis method is derived in Section 11.

The performance analysis sequence of computations is given in Section 12.

Briefly, the analysis procedure is:

1. Choose the input data

Z	=	flight altitude
y <sub>1</sub>	=	inlet diffuser inlet height
b	=	percent of span to be used as diffuser width
R <sub>pd</sub>	=	diffuser pressure recovery ratio
R <sub>ps</sub>	=	jet pressure recovery ratio
M <sub>2</sub>	=	collector-transfer section inlet Mach number

$y/y_2$  = collector-transfer section divergence function

$x_f/y$  = heat transfer foil chord length ratio

and the quantities  $\eta_0$ ,  $E_{ff}$ ,  $E_{uu}$ ,  $E_{ll}$ ,  $E_{uf}$ ,  $E_{lf}$ ,  $E_{su}$  which refer to the radiation transmitting, reflecting, absorbing and emitting properties of the heat transfer foils and the inner and outer surfaces of the aircraft.

2. Proceed with the operations of the analysis sequence in Section 12. These operations yield, besides much detailed information, the dimensions  $y_2$ ,  $y_3$ ,  $y_4$  and  $x_c$  as well as the dimensional ratios  $l_1/x_c$ ,  $l_2/x_c$ ,  $l_3/x_c$ , all with the performance results: the excess thrust coefficient

$\left\{ \frac{F}{q x_c} - C_D \right\}$  and the attainable wing loading  $\left( w/x_c \right)_a$ . The dimensions and dimensional ratios are determined for the maximum value of the wing loading  $\left( w/x_c \right)_a$ .

3. Repeat step (2) for various values of  $M_2$ ,  $y/y_2$ ,  $x_f/y$ , and  $b$  until the set of these is determined for maximum wing loading  $\left( w/x_c \right)_a$ .

4. Repeat steps (2) and (3) for various altitudes until the altitude is determined for the maximum wing loading,  $\left( w/x_c \right)_a$ .

The validity of these results of performance computation depend critically on the validity of the data: the diffuser and jet recovery ratios,  $R_{pd}$  and  $R_{pj}$ , the radiant energy transfer parameters  $\eta_0$ ,  $E_{ff}$ ,  $E_{uu}$ ,  $E_{ll}$ ,  $E_{uf}$ ,  $E_{lf}$ , and  $E_{su}$  and on the validity of the physical basis and assumptions (4), (5), (6) and (7) which determine the estimates of heat and momentum transfers to the internal stream in the collector-transfer section and to the external stream on the upper and lower wing surfaces.

## 6. PRIOR DESIGN AND PERFORMANCE ANALYSIS OF THE SOLAR POWERED AIRCRAFT

In WADC TN59-184, the final report of the first phase of this work, the results of a simpler but less valid analysis are presented. These results are shown in Table 2.6-1 of WADC TN59-184 and in Fig. 2 of this report. The design and performance results of Table 2.6-1 of WADC TN59-189 led to the choice of the parameters:

$$\begin{aligned}M_1 &= 1.5 \\M_2 &= 0.3 \\\eta_c &= 0.6 \\\epsilon_f &= 0.03 \\R_{pd} &= 0.93\end{aligned}$$

for the design of the optimum solar powered aircraft; the results of the performance analysis of designs based on these parameters are shown in Fig. 2. The performance results in Fig. 2 are shown here not in direct support of a statement of the feasibility of a solar powered aircraft but as an indication of the optimum altitude for a very large solar powered aircraft. The choice of the altitude, 200,000 ft. for the design and performance analyses of this report is based on Fig. 2. It is believed that the trends of chord length, altitude and wing loading in Fig. 2 are significant but that the magnitude of the attainable wing loadings are greatly overestimated. The particular assumptions of the prior method of design and performance analysis which led to the simple computation procedure with its extensive but insufficiently valid results are:

1. The heat transfer airfoil temperature,  $T_f$ , is constant along the collector-transfer section and equal to  $1133^\circ\text{K}$ .
2. The air temperature at the outlet of the collector transfer section,  $T_3$ , is equal to  $T_f$ .
3. The pressure recovery ratio across the heat transfer section,  $P_{s3}/P_{s2} = R_{ph}$  is estimated as if the Mach number were constant along the heat transfer section.

The design and performance method of this report was devised as a major step toward sufficient validity.

## 7. RESULTS OF SOLAR POWERED AIRCRAFT DESIGN AND PERFORMANCE ANALYSIS

The input data are shown in Table II; certain design and performance results are listed in Table III. The corresponding aircraft configurations are indicated in Figs. 3a and 3b. A brief description of the computational procedure is given in Section 5; the details procedure is set forth in Section 12.

The optimum aircraft for 200,000 feet altitude and diffuser inlet height of 20 feet is indicated by the third configuration of Case XI; the attainable wing loading is .042 lbs/ft<sup>2</sup> for a chord length of 1700 feet. In the design and performance study of this report indicated by Table II, Table III, and Figs. 3a and 3b, the flight altitude  $Z_1$  and the diffuser inlet height  $y_1$  were held constant and the quantities:  $M_2$ , the Mach Number at the diffuser outlet,  $d/dx (y/y_2)$  the divergence of the collector-transfer section;  $x_f/y$ , the heat transfer foil length;  $x_c$ , the wing chord length, were varied until the optimum set of them was found. It is interesting to note from Tables II and III the critical dependence of the wing loading  $w/x_c$  upon the set of quantities:  $M_2$ ,  $d/dx (y/y_2)$ ,  $(x_f/y)$  and  $x_c$ . There is needed the repetition of this procedure for the same diffuser inlet height for other altitudes in order to find the optimum solar powered aircraft according to the methods of this report. The configurations shown in Figs. 3a and 3b are surprisingly slender. It is a clear result of the prior design and performance analyses shown in Table 2.6-1 of WADC TN59-184 that the wing thickness to chord length ratio for optimum configurations varies approximately inversely at the atmospheric density. It is expected, therefore, that the optimum solar powered aircraft according to the methods of this report will, when found, have higher wing thickness ratio than shown in Figs. 3a and 3b for 200,000 feet flight altitude.

In Figs. 4,5,6,7,8,9,10,11,12,13,14,15,16 for Cases I,II,III,IV,V,VI,VII,VIII,X,XI,XII,XIII,XIV there is plotted the thrust,  $F$ , in lbs., the Mach number  $M$ , the temperature ratios:

$$T_f^*$$

$$T_u^*$$

$$T_\ell^*$$

$$T_s^*$$

each ratio relative to  $T_{s2}$ , the internal stream stagnation temperature at the

inlet of the collector transfer section and  $f_2$ , the fractional part of the incident solar energy transferred to the internal stream, all as functions of the distance  $x$  from the wing leading edge.

A survey of the curves in Figs. 4,5,6,7,8,9,10,11,12,13,14,15, and 16 reveal the critical dependence of  $F$ , the total thrust, upon  $T_s^*$ ,  $p_s^*$ , and  $M_3$  and the critical relation between  $p_s^*$  and  $M_3$ . Further consideration of these curves reveal that the most favorable condition for maximum  $(w/x_c)a$  occurs with  $M_3$  small and substantially constant with increasing  $x$ . This condition is obtained with the proper set of quantities  $d/dx (y/y_2)$  and  $s_f/y$ . These effects are due to the extremely critical dependence of the total thrust on the process of convective heat transfer and pressure loss due to friction occurring in the internal stream at the collector transfer foils and the extremely critical dependence of this heat transfer-pressure loss process on the parameters  $d/dx (y/y_2)$  and  $(x_f/y)$ . The parameter  $d/dx (y/y_2)$  is also critical with respect to drag of the external stream.

In Figs. 17, 18, and 19 for cases VIII, XI, and XII, are plotted the terms of Eq. (6) for the energy flux to the internal stream. The values of  $\eta_0 = 0.915$  indicates that 91.5 percent of the insolation on the collector-transfer section is absorbed by the heat transfer foils; it is estimated that loss of foil emission by transmission through the upper wing surface is negligible. The loss of energy at wing upper and lower surfaces is principally by emission; the loss there by convection to the external stream is small. The heat transfer to the wing surfaces is principally by radiative exchange between the collector transfer foils and the wing surfaces; the heat transfer by convection from the internal stream to the wing surfaces is negligible. And, of course, the heat transfer from the collector-transfer foils to the internal stream is by convection. The very significant effect to be noted here, is that a major loss of energy occurs by radiation from the collector-transfer foils to the wing upper and lower surface and hence by emission to space.

## 8. VALIDITY OF THE RESULTS OF PERFORMANCE ANALYSIS

The results of the performance analysis are summarized in Table III. These results were reached by well considered methods of analysis using such experimental results as were available and applicable. There is much to be desired, however, in the correspondence of both the simple models used as a basis of the performance analysis and the elementary experimental results with the configurations and processes of a real solar powered aircraft. In spite of these doubts there remains the results of Table III. The most significant result in Table III is the third configuration of Case XI; the attainable wing loading estimated is  $0.042 \text{ lbs/ft}^2$  for a chord length of 1700 ft. flying at air altitude of 200,000 ft. It is suggested that better performance with shorter chord length will be obtained at a higher altitude less than 220,000 ft.

Without consideration of the value of the solar powered aircraft, the results shown in Table III are judged from a technical point of view to be of sufficient validity to justify the following steps:

1. More Complete Design and Performance Analysis:
  - a. Revise and develop in detail the performance methods of this report.
  - b. Seek extensively and assiduously experimental results in the literature for the support of the input data of design and performance analyses.
  - c. Accomplish design and performance analyses over a sufficient range of the parameters:
    - $Z$ ; the flight altitude;  $y_1$ , the diffuser inlet height;  $M_2$ , the diffuser outlet Mach number  $d/dx$ ,  $(y/y_2)$  the divergence of the collector transfer section.
    - $x_f/y_1$ , the heat transfer foil length ratio
    - $x_c$ , the wing chord length.

## 9. THE UNSYMMETRICAL TWO-SHOCK INLET DIFFUSER

The unsymmetrical two-shock inlet diffuser is described and discussed in Refs. 2 and 3. In particular, attention is directed in Ref. 2 to Section 7 and Figs. 7.01 and 7.19. A sketch of the unsymmetrical two-shock inlet diffuser with its shock wave configuration for the design Mach number of 1.5 is shown in Fig. 20. The stagnation pressure ratio across the two-shock system from free stream  $M = 1.50$  to inlet  $M = 0.860$  is 0.9867. The stagnation pressure ratio just downstream of the normal shock is slightly less than 0.9867, due to the boundary layer on the upper surface. The advantages of this design are:

1. There is no swallowing problem since the entrance section and throat are identical.
2. In the supersonic part of the diffusion, from free stream to within the normal shock, there is boundary layer effect on only one surface.
3. The unsymmetrical condition due to the boundary layer at the normal shock on the upper surface insures that the unsymmetrical boundary layer thickening, turbulence and separation effects, which occur even in symmetrical subsonic diffusers, will occur in this case on the upper surface, and a more favorable boundary layer may be maintained on the lower surface.

The prospect of localizing the turbulence and separation in the subsonic diffuser on the upper surface suggests starting a diagonal array of heat transfer foils from the upper surface and from within the subsonic diffuser. Thus the turbulence occurring in this region will be utilized for heat transfer and the spread of large scale eddies will be reduced by means of the heat transfer foils acting as vanes.

## 10. ELEMENTARY CONSIDERATIONS OF TOTAL THRUST AND REYNOLDS ANALOGY

### 10.1 Discussion of the Total Thrust

The Equation 124 estimates the total thrust per unit span for the solar powered aircraft. Let us derive an expression for the total thrust per unit span as in Section 11.3 but in this case:

1. Utilizing only a fraction  $b$  of the span for diffuser inlet, and
2. Estimating the temperature  $R_T$  as

$$\begin{aligned} R_T &= \frac{T_{s3}}{T_{s1}} = 1 + \frac{tg_s \eta_s x_c}{p_{1\ell\ell} b y_1 C_p T} \\ &= 1 + \frac{g_s \eta_s x_c}{(N_R)_1 b (N_p)_1 R T_1} \end{aligned} \quad (1)$$

where  $\eta_s$  is the net fraction of the incident insolation which is delivered to the internal stream and is not lost. Then,

$$\begin{aligned} F &= 2gby_1 \left\{ \sqrt{2 \left[ 1 + \frac{g_s \eta_s x_c}{b(N_R)_1 (N_p)_1 R T_1} \right]} \times \right. \\ &\quad \left. \sqrt{\left[ 1 + \frac{\gamma-1}{2} M_1^2 \right] - \left( \frac{1}{R_p} \right) \frac{\gamma-1}{\gamma} - 1} \right\} \end{aligned} \quad (2)$$

where

$$0 < b < 1$$

Thus,  $F$  is a function of the design parameters  $b$ ,  $x_c$ ,  $\eta_s$ ; it is a monotonically increasing function with all these parameters. The use of  $b = 1$  rather than a lower value will determine that the internal stream temperature will be lower. Also, due to the lower stream temperature the foil temperature will be lower and hence  $\eta_s$  will be higher since the loss of the heat delivered to the foils is chiefly by radiation to the upper and lower wing surfaces. Therefore, except as  $R_p$ , the pressure recovery ratio is related to  $b$ ,  $\eta_s$ , and  $x_c$ , the total thrust per unit span is maximum for  $b = 1$ . As we shall see in Section 10.2, the pressure recovery ratio is, however, related to  $b$ ,  $\eta_s$  and  $x_c$ .



## 10.2 Relation Between Pressure Loss and Heat Transfer

According to Eq. 63 of Ref. 7 in the notation of this report,

$$\frac{Q_f}{R(T_f - T_e)} = \frac{C_{df} Re_{xf}}{2} N_p^{1/3} \quad (3)$$

This equation expresses the Reynold's analogy relation between skin friction and heat transfer for a flat plate with constant surface temperature. The pressure loss per unit length is

$$\frac{\Delta P}{x_f} = \frac{\rho u^2 C_{df}}{y} \quad (4)$$

Then, from (3) and (4) with

$$P = \rho RT$$

$$\frac{\left( \frac{1}{x_f} \frac{\Delta P}{P} \right)}{\left( \frac{Q_f}{x_f} \right)} = \frac{\gamma M^2}{R(T_f - T_e) Re_y N_p^{1/3}} \quad (5)$$

The ratio of the rate of stagnation pressure loss to the rate of heat transfer in the collector-transfer duct increases as the square of the local Mach number, inversely as the temperature difference of the heat transfer foils and the internal stream and inversely as the local Reynolds number referred to stream height. Thus, reduced airflow by means of  $b < 1$  as discussed in Section 10.1 may allow such reduction in stagnation pressure loss as to yield increased thrust and finally increased wing loading. This matter is judged to be so involved, however, as to require the inclusion of  $b$  with the parameters to be varied in seeking the optimum design. Since,  $\frac{M^2}{Re_y}$  in (5) varies approximately as  $\frac{1}{y^2}$  it is clear that the maximum cross-section of the internal stream is consistent with the external drag is desirable for the reduction of the pressure loss in the internal stream.

## 11. DEVELOPMENT OF METHOD OF ANALYSIS

### 11.1 Performance of the Radiation Collector Heat Transfer Section

#### 11.1.1 The Equations of Energy Flux in the Collector-Transfer Section

The energy flux to the internal stream is

$$\frac{dQ}{dx} = \eta_o q_s - R - C_{ext} = C_f + C_{int} \quad (6)$$

where

- $q_s$  = energy flux from the sun
- $\eta_o q_s$  = energy flux from the sun absorbed by the collector-transfer section
- $R$  = energy flux lost by radiation
- $C_{ext}$  = energy flux lost by convection to the external stream
- $C_f$  = energy flux by convection from the collector-transfer foils to the internal stream
- $C_{int}$  = energy flux by convection from the collector-transfer wall surfaces to the internal stream,

and where the energy fluxes  $\eta_o q_s$ ,  $R$ ,  $C_{ext}$ ,  $C_f$ , and  $C_{int}$  are defined as energy per unit time per unit area normal to the solar beam. These energy fluxes are functions of position along the wing chord.

The condition that the net flux of energy to the upper and lower wing surfaces are each zero yields the equations:

$$q_{\lambda_f}(f \rightarrow u) - q_{\lambda_u}(u \rightarrow f) - C_{int_u} + (q_{\lambda_s u}) = C_{ext_u} + q_{\lambda_u u \rightarrow} + q_{\lambda_f u \rightarrow} \quad (7)$$

$$q_{\lambda_f}(f \rightarrow l) - q_{\lambda_l}(l \rightarrow f) - C_{int_l} = C_{ext_l} + q_{\lambda_l l \rightarrow} + q_{\lambda_f l \rightarrow} \quad (8)$$

where

- $q_{\lambda_f}(f \rightarrow u)$  = Collector-transfer surface thermal radiation energy absorbed by the wing upper surface.

- $q_{\lambda_u}(u \rightarrow f) =$  Wing upper surface thermal radiation energy absorbed by the collector-transfer surface.  
 $q_{\lambda_f}(f \rightarrow l) =$  Collector-transfer surface thermal radiation energy absorbed by the wing lower surface.  
 $q_{\lambda_l}(l \rightarrow f) =$  Wing lower surface thermal radiation energy absorbed by the collector-transfer surface.  
 $(q_{\lambda_s f}) =$  Solar radiation absorbed by the collector-transfer surface.  
 $(q_{\lambda_s u}) =$  Solar radiation absorbed by the wing upper surface.  
 $q_{\lambda_s u \rightarrow} =$  Solar radiation reflected externally at the upper wing surface.  
 $q_{\lambda_u u \rightarrow} =$  Wing upper surface thermal radiation emitted externally.  
 $q_{\lambda_l l \rightarrow} =$  Wing lower surface thermal radiation emitted externally.  
 $q_{\lambda_f u \rightarrow} =$  Collector-transfer surface thermal radiation energy transmitted by the wing upper surface.  
 $q_{\lambda_f l \rightarrow} =$  Collector-transfer surface thermal radiation energy transmitted by the wing lower surface.

#### 11.1.2 Radiant Energy Transfer in the Collector-Transfer Section

The arrangement of radiation collector-heat transfer foils under consideration for the solar powered aircraft is as shown in Fig. 21. The analysis of the radiant energy transfer in this configuration has proved very difficult. Therefore, in order to obtain a rational and an "at best" estimate of the radiant energy transfer, assume the collector-transfer foils to be equivalent to a plane sheet between the upper and lower surfaces of the wing as in Fig. 22, where

- $\epsilon, \rho, \alpha, \tau =$  emissivity, reflectance, absorptance and transmittance, respectively.  
 $s, u, f, l =$  subscripts referring to the sun, wing upper surface, collector-transfer surface and wing lower surface, respectively.

$\lambda_s, \lambda_u, \lambda_f, \lambda_l$  = subscripts referring to solar radiation, thermal radiation of wing upper surface, collector-transfer surface and wing lower surface, respectively.

In general,

$$\epsilon_{\lambda_i j} = \alpha_{\lambda_i j} \quad (9)$$

$$\rho_{\lambda_i j} + \alpha_{\lambda_i j} + \tau_{\lambda_i j} = 1 \quad (10)$$

Consider first, the radiant energy exchange between two parallel infinite plane surfaces as in Fig. 23. According to Ref. 4, Article 14.2, p. 403, the heat flux lost by surface 1 as radiation  $\lambda_1$  is

$$q_{\lambda_1}(1-2) = \frac{1 - \rho_{\lambda_1 2}}{1 - \rho_{\lambda_1 1} \rho_{\lambda_1 2}} \epsilon_{\lambda_1} \sigma T_1^4 \quad (11)$$

and the radiation lost by surface 2 as radiation  $\lambda_2$  is

$$q_{\lambda_2}(2-1) = \frac{1 - \rho_{\lambda_2 1}}{1 - \rho_{\lambda_2 2} \rho_{\lambda_2 1}} \epsilon_{\lambda_2} \sigma T_2^4 \quad (12)$$

Consider now, the "green house" effect between two parallel infinite plane surfaces as in Fig. 24. The  $\lambda_s$  energy flux retained by surface 2 is

$$(q_{\lambda_s 2}) = q_s \frac{\tau_{\lambda_s 1} (1 - \rho_{\lambda_s 2})}{1 - \rho_{\lambda_s 1} \rho_{\lambda_s 2}} \quad (13)$$

and the  $\lambda_s$  energy flux retained by surface 1 is

$$(q_{\lambda_s 1}) = q_s \alpha_{\lambda_s 1} \left\{ 1 + \frac{\tau_{\lambda_s 1} \rho_{\lambda_s 2}}{1 - \rho_{\lambda_s 1} \rho_{\lambda_s 2}} \right\} \quad (14)$$

Now, for the collector-transfer section, by use of Eqs. 11 and 12

$$q_{\lambda_f}(f \rightarrow u) = \frac{1 - \rho_{\lambda_f u}}{1 - \rho_{\lambda_f f} \rho_{\lambda_f u}} \epsilon_{\lambda_f} \sigma T_f^4 \quad (15)$$

$$q_{\lambda_u}(u \rightarrow f) = \frac{1 - \rho_{\lambda_u f}}{1 - \rho_{\lambda_u u} \rho_{\lambda_u f}} \epsilon_{\lambda_u} \sigma T_u^4 \quad (16)$$

$$q_{\lambda_f}(f \rightarrow 1) = \frac{1 - \rho_{\lambda_f 1}}{1 - \rho_{\lambda_f f} \rho_{\lambda_f 1}} \epsilon_{\lambda_f} \sigma T_f^4 \quad (17)$$

$$q_{\lambda_1}(1 \rightarrow f) = \frac{1 - \rho_{\lambda_1 f}}{1 - \rho_{\lambda_1 1} \rho_{\lambda_1 f}} \epsilon_{\lambda_1} \sigma T_1^4 \quad (18)$$

and by use of Eqs. 13 and 14

$$(q_{\lambda_s f}) = q_s \frac{\tau_{\lambda_s u} (1 - \rho_{\lambda_s f})}{1 - \rho_{\lambda_s u} \rho_{\lambda_s f}} \quad (19)$$

$$(q_{\lambda_s u}) = q_s \alpha_{\lambda_s u} \left\{ 1 + \frac{\tau_{\lambda_s u} \rho_{\lambda_s f}}{1 - \rho_{\lambda_s u} \rho_{\lambda_s f}} \right\} \quad (20)$$

finally

$$q_{\lambda_s u} = q_s \rho_{\lambda_s u} \quad (21)$$

$$q_{\lambda_u u} = \epsilon_{\lambda_u} \sigma T_u^4 \quad (22)$$

$$q_{\lambda_1 1} = \epsilon_{\lambda_1} \sigma T_1^4 \quad (23)$$

Assume

$$q_{\lambda_f u \rightarrow} = 0 = q_{\lambda_f l \rightarrow} \quad (24)$$

By definition of  $\eta_0 q_s$  with Eqs. 19 and 20

$$\begin{aligned} \eta_0 &= \frac{q_{\lambda_s f} + q_{\lambda_s u}}{q_s} \\ &= \frac{\tau_{\lambda_s u} (1 - \rho_{\lambda_s f})}{1 - \rho_{\lambda_s u} \rho_{\lambda_s f}} + \alpha_{\lambda_s u} \left\{ \frac{\tau_{\lambda_s u} \rho_{\lambda_s f}}{1 - \rho_{\lambda_s u} \rho_{\lambda_s f}} \right\} \end{aligned} \quad (25)$$

and by definition of R with Eqs. 22, 23 and 24

$$R = q_{\lambda_u} + q_{\lambda_l} = \epsilon_{\lambda_u} \sigma T_1^4 + \epsilon_{\lambda_l} \sigma T_1^4 \quad (26)$$

Assume, for example

$$\tau_{\lambda_s u} = .91$$

$$\alpha_{\lambda_s u} = .03 \quad \rho_{\lambda_s u} = .06$$

$$\rho_{\lambda_s f} = .03$$

$$\epsilon_{\lambda_f} = .06$$

$$\epsilon_{\lambda_u} = .03 = \epsilon_{\lambda_l}$$

$$\rho_{\lambda_f f} = .94$$

$$\rho_{\lambda_u u} = .97 = \rho_{\lambda_l l}$$

$$\rho_{\lambda_u f} = .94 = \rho_{\lambda_l f}$$

$$\rho_{\lambda_f u} = .97 = \rho_{\lambda_f l}$$

then

$$q_{\lambda_f}(f \rightarrow u) = .340 \epsilon_{\lambda_f} \sigma T_f^4$$

$$q_{\lambda_u}(u \rightarrow f) = .680 \epsilon_{\lambda_u} \sigma T_u^4$$

$$q_{\lambda_f}(f \rightarrow 1) = .340 \epsilon_{\lambda_f} \sigma T_f^4$$

$$q_{\lambda_1}(1 \rightarrow f) = .680 \epsilon_{\lambda_1} \sigma T_1^4$$

$$(q_{\lambda_s f}) = .883 q_s$$

$$(q_{\lambda_s u}) = .031 q_s$$

$$q_{\lambda_s u \rightarrow} = .050 q_s$$

$$\eta_o = .914$$

$$\frac{R}{q_s} = .1210 \left[ \left( \frac{T_u}{1000} \right)^4 + \left( \frac{T_1}{1000} \right)^4 \right]$$

$$\frac{q_{\lambda_f}(f \rightarrow u) - q_{\lambda_u}(u \rightarrow f)}{q_s} = .0823 \left[ \left( \frac{T_f}{1000} \right)^4 - \left( \frac{T_u}{1000} \right)^4 \right]$$

$$\frac{q_{\lambda_f}(f \rightarrow 1) - q_{\lambda_1}(1 \rightarrow f)}{q_s} = .0823 \left[ \left( \frac{T_f}{1000} \right)^4 - \left( \frac{T_1}{1000} \right)^4 \right]$$

#### 11.1.3 The Temperature Change Along the Internal Stream

It is assumed that the net energy flow to the internal airstream occurs uniformly across the stream. Hence,

$$\frac{dq}{dx} = y_{up} C_p \frac{dT_s}{dx} \quad (27)$$

where

$$\gamma u p = \gamma_2 u_2 p_2 \quad (28)$$

#### 11.1.4 One Dimensional Channel Flow in the Radiation Collector-Heat Transfer Section

The approximation of one dimensional channel flow is better as the arrangement of the collector-transfer foils tends toward a uniform density of foils across each cross-section thus tending toward uniform heat flux to the stream and uniform flow conditions across each section.

For one dimensional channel flow with heat addition, friction and area change, according to Ref. 5:

$$\frac{P_s}{P_{s_2}} \sqrt{\frac{T_{s_2}}{T_s}} = \frac{A_2}{A} \frac{M_2}{M} \left\{ \frac{1 + \frac{\gamma-1}{2} M^2}{1 + \frac{\gamma-1}{2} M_2^2} \right\}^{\frac{\gamma+1}{2(\gamma-1)}} \quad (29)$$

$$\log \left\{ \sqrt{\frac{T_s}{T_{s_2}}} \sqrt{\frac{1 + \frac{\gamma-1}{2} M_2^2}{1 + \frac{\gamma-1}{2} M^2}} \frac{M_2}{M} \frac{1 + \gamma M^2}{1 + \gamma M_2^2} \right\} \\ = \int_2 \frac{\gamma M^2}{1 + \gamma M^2} \left\{ \frac{dA}{\gamma M^2 A} - \frac{f}{2m} dx \right\} \quad (30)$$

where  $P_{s_2}$ ,  $T_{s_2}$ ,  $A_2$ ,  $M_2$  are stream conditions at Station 2. The subscript s refers to stagnation conditions.

$$P_s = P \left\{ 1 + \frac{\gamma-1}{2} M^2 \right\}^{\frac{\gamma}{\gamma-1}} \quad (31)$$

$$T_s = T \left\{ 1 + \frac{\gamma-1}{2} M^2 \right\} \quad (32)$$

where P and T are the stream conditions of pressure and temperature.



$$\begin{aligned}
M &= \text{Mach number} \\
m &= \frac{2 \times \text{Area of stream cross-section}}{\text{Wetted Perimeter of stream cross-section}} \\
m &= \text{hydraulic radius} \\
f &= \text{channel flow friction factor, such that}
\end{aligned} \tag{33}$$

$$\left( \frac{dp}{dx} \right)_{\text{due to friction}} = \frac{f}{2m} \cdot \rho v^2 \tag{34}$$

Equation 36 holds with or without either or both friction and heat addition. When  $T_s$ ,  $A$  and  $f/2m$  are known functions of  $x$ , the equations 36 and 37 may be solved for  $P_s$  and  $M$  as functions of  $x$ .

Equation 29 may be written in a form more convenient for use, as

$$\frac{A}{A_2} = \frac{Y}{Y_2} = \left\{ \frac{M_2}{M} \frac{1 + \frac{Y-1}{2} M^2}{1 + \frac{Y-1}{2} M_2^2} \right\}^{\frac{Y+1}{2(Y-1)}} \sqrt{\frac{T_s}{T_{s2}}} \left( \frac{P_s}{P_{s2}} \right) \tag{35}$$

where

$$\frac{M_2}{M} \left\{ \frac{1 + \frac{Y-1}{2} M^2}{1 + \frac{Y-1}{2} M_2^2} \right\}^{\frac{Y+1}{2(Y-1)}} = \frac{\bar{m}(M_2)}{\bar{m}(M)} = \frac{\left( \frac{A}{A^*} \right)}{\left( \frac{A_2}{A^*} \right)} \tag{36}$$

where  $A/A^*$  is tabulated in Ref. 6.

#### 11.1.5 Heat Flux by Convection from the Collector-Transfer Foils to the Internal Stream

Assume the heat transfer from the foils to the airstream is for each foil as if it were in conventional flat plate laminar flow. Then according to Eq. 53 of Ref. 7 and Eq. 14.68 of Ref. 8:

$$C_f = \frac{Q_f}{x_f} = \frac{1.1830k \sqrt{Y_f}}{x_f} \sqrt{N_{R_{x_f}}} (T_f - T_e) \tag{37}$$

where

$$N_{R_{x_f}} = \frac{x_f u_0}{\mu} \quad \text{Reynolds number} \quad (38)$$

$$T_e = T \left[ 1 + r_{(0)} \frac{\gamma - 1}{2} M^2 \right] \quad (39)$$

$$r_{(0)} = .845$$

$$\gamma_f = \sqrt{\frac{T_f}{T}} \frac{T + 216}{T_f + 216} \quad (40)$$

$Q_f$  = Net heat flow from a collector-transfer foil to internal stream per unit of wing span

$x_f$  = Chord length of the collector-transfer foils

$\gamma$  = Ratio of specific heats

$k, \mu, T, M$  = Thermal conductivity, coefficient of viscosity, temperature and Mach number of the internal stream, all assumed constant across each stream cross-section.

#### 11.1.6 Momentum Transfer between Collector-Transfer Foils and the Internal Stream

Assuming conventional flat plate laminar flow on the collector-transfer foils, then according to Eq. 58a of Ref. 8:

$$C_{Df} = \frac{1.328 \sqrt{\gamma_f}}{\sqrt{N_{R(x_f + x_p)}}} \quad (41)$$

For two sides of one foil

$$\frac{\Delta P}{\Delta x} = \frac{2 C_{Df}^{1/2} \rho v^2}{y} \quad (42)$$

By definition of  $f/2m$

$$\frac{dP}{dx} = \frac{f}{2m} \rho v^2 \quad (43)$$

Hence

$$\left(\frac{f}{2m}\right)_f = \frac{C_{Df}}{y} = \frac{1.328\sqrt{\gamma_f}}{y\sqrt{N_F(x_f + x_p)}} \quad (44)$$

$$N_{R(x_f + x_p)} = \frac{(x_f + x_p) u \rho}{\mu} \quad (45)$$

#### 11.1.7 Estimation of the Momentum and Convective Heat Transfer of the Collector-Transfer Section Walls to the Internal Stream

On the assumption that the drag and heat addition are uniformly distributed over the stream cross-sections and on the fact that the momentum transfer from the walls is small in comparison with that from the collector-transfer foils, the velocity distribution across the stream will tend to be uniform except near the walls. Therefore, it is assumed that the boundary layers are just fully developed turbulent throughout the channel and corresponding to the point.

$$N_R = \frac{\bar{u}d}{\nu} = 4000 \quad (46)$$

$$100 \lambda = 4$$

on Fig. 20.17, page 418 of Ref. 8. Then

$$\lambda \approx 2f \approx .04 \quad (47)$$

And further, according to empirical formulas of Dittus and Boelter cited on page 211 of Ref. 4

$$Nu_d = \frac{hd}{k} = .025 N_{R_d}^{.8} Pr^{.4} \quad (48)$$

$h$  = film heat transfer coefficient per unit area of channel surface. Hence, for

$$\left. \begin{array}{l} N_{R_d} = 4000 \\ N_p = .70 \end{array} \right\} \quad (49)$$

$$h = \frac{16k}{2m} \quad (50)$$

$$2m = \frac{4 \times \text{Area}}{\text{Wetted Perimeter}} = y_2 \frac{2 \frac{y}{y_2} \left( \frac{w}{y_1} \right) \left( \frac{y_1}{y_1} \right)}{\frac{y}{y_2} + \left( \frac{w}{y_1} \right) \left( \frac{y_1}{y_2} \right)} \quad (51)$$

w = width of duct

The heat flux by convection from the upper and lower surfaces of the wing to the internal stream are

$$\begin{aligned} C_{(int)_u} &= \frac{16k}{2m} (T_u - T_e) \\ C_{(int)_l} &= \frac{16k}{2m} (T_l - T_e) \end{aligned} \quad (52)$$

where

$T_u, T_l$  = temperature of the upper and lower wing surfaces, respectively

and

$$C_{int} = C_{(int)_u} + C_{(int)_l} \quad (53)$$

#### 11.1.8 Heat Transfer from Upper and Lower Wing Surfaces to the External Stream

According to Eq. 50 on page 557 of Ref. 7

$$q = \frac{k_{\infty} \tau_{\infty}}{2} \gamma_w \sqrt{\frac{U_{\infty} \rho_{\infty}}{\mu_{\infty} x \gamma_w}} \sum_{n=0}^{\infty} A_n x^{*n} Y_n^* (o) \quad (54)$$

where

q = local rate of heat transfer, per unit area  
subscripts

$\infty$  = condition outside the boundary layer

w = condition at the wing surface

e = equilibrium conditions for all insulated surface  
superscript

\* = dimensionless quantity

$$Re_x \approx \frac{U_\infty \rho_\infty}{\mu_\infty} \quad (55)$$

$$\gamma_w = \sqrt{\frac{T_w}{T_\infty} \frac{T_\infty + S}{T_w + S}} \quad (56)$$

$$\bar{\gamma}_w = \sqrt{\frac{\bar{T}_w}{T_\infty} \frac{T_\infty + S}{T_w + S}} \quad (57)$$

$$S = 216$$

$$\bar{T}_w = \text{wing surface average temperature}$$

$$x^* = x/x_c \quad (58)$$

$$\frac{T_e}{T_1} = T_e^* = 1 + r(0) \frac{\gamma-1}{2} M_\infty^2; r(0) = .845 \quad (59)$$

$$T_w^* = \frac{T_w}{T_\infty} = T_e^* + t(x^*) = \frac{T_e}{T_1} + \frac{T_w - T_e}{T_1} \quad (60)$$

where  $t(x^*)$  may be approximated by a polynomial

$$\left. \begin{aligned} t(x^*) &= \sum_{n=0}^{\infty} a_n x^{*n} \\ a_n &= t^{(n)}(0)/n! \end{aligned} \right\} \quad (61)$$

where

$n$	$Y_n^t(0)$
0	-0.5915
1	-0.9775
2	-1.1949

Assume skin temperature distribution to be linear with distance from the leading edge, where it has the free stream recovery temperature

$$T_e = T_w(0,0) = T_\infty \left[ 1 + .845 \frac{\gamma-1}{2} M_\infty^2 \right] \quad (62)$$

to a maximum at the wing trailing edge. Then,

$$T_w^* - T_e^* = t_{(x^*)} = a_1 x^* \quad (63)$$

$$a_0 = 0 = a_2 = a_3, \dots$$

and

$$q = \frac{k_{\infty}}{2} \frac{\gamma_w}{\sqrt{\gamma_w}} \sqrt{\frac{U_{\infty} \rho_{\infty}}{\mu_{\infty} x}} (T_w - T_e) \gamma_1' (0) \quad (64)$$

Hence, in the notation of this report

$$\left. \begin{aligned} C_{ext_u} &= .4897 k_1 \frac{\gamma_u}{\sqrt{\gamma_u}} \sqrt{\frac{u_1 \rho_1}{\mu_1 x}} (T_u - T_e) \\ C_{ext_l} &= .4897 k_1 \frac{\gamma_l}{\sqrt{\gamma_l}} \sqrt{\frac{u_l \rho_l}{\mu_l x}} (T_l - T_e) \end{aligned} \right\} \quad (65)$$

$$C_{ext} = C_{ext_u} + C_{ext_l} \quad (66)$$

#### 11.1.9 The Performance Equations of the Collector-Transfer Section

##### Collection of Results

$$\frac{dQ}{dx} = \eta_o q_s - R - C_{ext} = C_f + C_{int} \quad (67)$$

$$\frac{dQ}{dx} = y_{up} C_p \frac{dT_s}{dx} \quad (68)$$

$$y_{up} = y_2 u_2 \rho_2 \quad (69)$$

$$\eta_o = \frac{\tau_{\lambda_{su}} (1 - \rho_{2sf})}{1 - \rho_{\lambda_{su}} \rho_{\lambda_{sf}}} + \alpha_{\lambda_{su}} \left\{ 1 + \frac{\tau_{\lambda_{su}} \rho_{\lambda_{sf}}}{1 - \rho_{\lambda_{su}} \rho_{\lambda_{sf}}} \right\} \quad (70)$$

$$R = \epsilon_{\lambda_u} \sigma T_u^4 + \epsilon_{\lambda_1} \sigma T_1^4 \quad (71)$$

$$C_{ext} = C_{ext_u} + C_{ext_1} = .4897 k_1 \left\{ \frac{\gamma_u}{\sqrt{\gamma_u}} \sqrt{\frac{u_1 \rho_1}{\mu_1 x}} (T_u - T_e) \right. \\ \left. + \frac{\gamma_1}{\sqrt{\gamma_1}} \sqrt{\frac{u_1 \rho_1}{\mu_1 x}} (T_1 - T_e) \right\} \quad (65) \text{ and } (66) = (72)$$

$$\gamma_{u,1} = \sqrt{\frac{T_{u,1}}{T_1}} \frac{T_1 + 216}{T_{u,1} + 216}; \quad \bar{\gamma}_{u,1} = \sqrt{\frac{\bar{T}_{u,1}}{T_1}} \frac{T_1 + 216}{\bar{T}_{u,1} + 216}$$

$$T_{e_1} = T_1 \left\{ 1 + .845 \frac{\gamma-1}{2} M_1^2 \right\} \quad (73)$$

$$C_f = \frac{1.1830 k \sqrt{\gamma_f}}{x_f} \sqrt{N_{R_{x_f}}} (T_f - T_e) \quad (74)$$

$$N_{R_{x_f}} = \frac{x_f u \rho}{\mu} \quad (75)$$

$$T_e = T \left\{ 1 + .845 \frac{\gamma-1}{2} M^2 \right\} \quad (76)$$

$$\gamma_f = \sqrt{\frac{T_f}{T}} \frac{T + 216}{T_f + 216} \quad (77)$$

$$C_{int} = C_{(int)_u} + C_{(int)_1} = \frac{32k}{2m} \left\{ \frac{\bar{T}_u + T_1}{2} - T_s \right\} \quad (52) \text{ and } (53) = (78)$$

$$2m = y_2 \frac{2 \frac{\gamma}{y_2} \left( \frac{w}{y_1} \right) \left( \frac{y_1}{y_2} \right)}{\frac{\gamma}{y_2} + \left( \frac{w}{y_1} \right) \left( \frac{y_1}{y_2} \right)} \quad (79)$$

$$q_{\lambda_f(f \rightarrow u)} - q_{\lambda_u(u \rightarrow f)} - C_{(int)_u} + (q_{\lambda_s u}) = C_{(ext)_u} + q_{\lambda_u u} + q_{\lambda_f u} \quad (80)$$

$$q_{\lambda_f}(f \rightarrow 1) - q_{\lambda_1}(1 \rightarrow f) - C_{int_1} = C_{(ext)_1} + q_{\lambda_1} 1 \rightarrow + q_{\lambda_f} 1 \quad (81)$$

$$q_{\lambda_f}(f \rightarrow u) = \frac{1 - \rho_{\lambda_s u}}{1 - \rho_{\lambda_f f} \rho_{\lambda_s u}} \epsilon_{\lambda_f} \sigma T_f^4 \quad (82)$$

$$q_{\lambda_u}(u \rightarrow f) = \frac{1 - \rho_{\lambda_u f}}{1 - \rho_{\lambda_u u} \rho_{\lambda_u f}} \epsilon_{\lambda_u} \sigma T_u^4 \quad (83)$$

$$q_{\lambda_f}(f \rightarrow 1) = \frac{1 - \rho_{\lambda_f 1}}{1 - \rho_{\lambda_f f} \rho_{\lambda_f 1}} \epsilon_{\lambda_f} \sigma T_f^4 \quad (84)$$

$$q_{\lambda_1}(1 \rightarrow f) = \frac{1 - \rho_{\lambda_1 f}}{1 - \rho_{\lambda_1 1} \rho_{\lambda_1 f}} \epsilon_{\lambda_1} \sigma T_1^4 \quad (85)$$

$$(q_{\lambda_s u}) = q_s \alpha_{\lambda_s u} \left\{ 1 + \frac{\tau_{\lambda_s u} \rho_{\lambda_s f}}{1 - \rho_{\lambda_s u} \rho_{\lambda_s f}} \right\} \quad (86)$$

$$q_{\lambda_u u} \rightarrow \epsilon_{\lambda_u} \sigma T_u^4 \quad (87)$$

$$q_{\lambda_1 1} \rightarrow \epsilon_{\lambda_1} \sigma T_1^4 \quad (88)$$

$$q_{\lambda_f u} \rightarrow = 0 = q_{\lambda_f 1} \quad (89)$$

$$\frac{P_s}{P_{s2}} \sqrt{\frac{T_{s2}}{T_s}} = \frac{A_2}{A} \frac{M_2}{M} \left\{ \frac{1 + \frac{\gamma-1}{2} M^2}{1 + \frac{\gamma-1}{2} M_2^2} \right\}^{\frac{\gamma+1}{2(\gamma-1)}} \quad (90)$$



$$\log \left\{ \sqrt{\frac{T_s}{T_{s2}}} \sqrt{\frac{1 + \frac{\gamma-1}{2} M_2^2}{1 + \frac{\gamma-1}{2} M^2}} \frac{M_2}{M} \frac{1 + \gamma M^2}{1 + \gamma M_2^2} \right\} \\ = \int_2 \frac{\gamma M^2}{1 + \gamma M^2} \left\{ \frac{dA}{\gamma M^2 A} - \frac{f}{2m} dx \right\} \quad (44) \text{ and } (47) = \quad (91)$$

$$\frac{f}{2m} = \left( \frac{f}{2m} \right)_f + \left( \frac{f}{2m} \right)_w = \frac{1.328 \sqrt{\gamma f}}{\gamma \sqrt{N_R(x_f + x_p)}} + \frac{.02}{2m} \\ N_R(x_f + x_p) = \frac{(x_f + x_p) u \rho}{\mu} \quad (92)$$

By Sutherland's formula

$$\frac{\mu_2}{\mu} = \left( \frac{T_2}{T} \right)^{3/2} \frac{T + S}{T_2 + S} \quad (93)$$

$$S = 216$$

according to Ref. 7

From Eq. 6 with Eqs. 27, 28, 26, 65 and 66, 37, 52 and 53

$$\begin{aligned}
& \left( \frac{y_2 u_2 p_2}{\mu_2} \right) \left( \frac{\mu_2 C_p}{k_2} \right) \left( \frac{k_2 T_{s2}}{q_s} \right) \frac{d \left( \frac{T_s}{T_{s2}} \right)}{dx} = \eta_o \\
& - \frac{0.7 \times 10^{+12}}{q_s} \left( \frac{T_{s2}}{1000} \right)^4 \left\{ \epsilon_{\lambda_u} \left( \frac{T_u}{T_{s2}} \right)^4 + \epsilon_{\lambda_1} \left( \frac{T_l}{T_{s2}} \right)^4 \right\} \\
& - \frac{.4897}{\sqrt{x}} \left( \frac{k_2 T_{s2}}{q_s} \right) \left( \frac{k_1}{k_2} \right) \sqrt{\left( \frac{N_R}{x} \right)} \left\{ \frac{\gamma_u}{\sqrt{\gamma_u}} \left( \frac{T_u}{T_{s2}} - \frac{T_{e1}}{T_{s2}} \right) + \frac{\gamma_1}{\sqrt{\gamma_1}} \left( \frac{T_1}{T_{s2}} - \frac{T_{e1}}{T_{s2}} \right) \right\} \\
& = 1.1830 \left( \frac{k_2 T_{s2}}{q_s} \right) \sqrt{\frac{y_2 \left( \frac{N_R}{x} \right)}{y_2}} \frac{k}{k_2} \sqrt{\frac{\mu_2}{\gamma_f}} \frac{\left( \frac{T_f}{T_{s2}} - \frac{T_s}{T_{s2}} \frac{T_e}{T_s} \right)}{\sqrt{\frac{y}{y_2}} \sqrt{\frac{x_f}{y}}} \\
& + \frac{32}{2m} \left( \frac{k_2 T_{s2}}{q_s} \right) \left( \frac{k}{k_2} \right) \left\{ \frac{\frac{T_u}{T_{s2}} + \frac{T_1}{T_{s2}}}{2} - \frac{T_s}{T_{s2}} \right\} \quad (95)
\end{aligned}$$

From Eq. 7 with Eqs. 15, 16, 22, 24, 52, 20 and 65

$$\begin{aligned}
 & \frac{\sigma \times 10^{+12}}{q_s} \left( \frac{T_{s_2}}{1000} \right) \left\{ \frac{1 - \rho_{\lambda_f u}}{1 - \rho_{\lambda_f} \rho_{\lambda_f u}} \epsilon_{\lambda_f} \left( \frac{T_f}{T_{s_2}} \right)^4 \right. \\
 & \quad \left. - \frac{1 - \rho_{\lambda_u f}}{1 - \rho_{\lambda_u} \rho_{\lambda_u f}} \epsilon_{\lambda_u} \left( \frac{T_u}{T_{s_2}} \right)^4 \right\} \\
 & - \frac{16}{2m} \left( \frac{k_2 T_{s_2}}{q_s} \right) \left( \frac{k}{k_2} \right) \left( \frac{T_u}{T_{s_2}} - \frac{T_e}{T_{s_2}} \right) + \alpha_{\lambda_s u} \left\{ 1 + \frac{\tau_{\lambda_s u} \rho_{\lambda_s f}}{1 - \rho_{\lambda_s u} \rho_{\lambda_s f}} \right\} \\
 & = \frac{.4897}{\sqrt{x}} \left( \frac{k_2 T_{s_2}}{q_s} \right) \left( \frac{k_1}{k_2} \right) \sqrt{\frac{N_R}{x}} \frac{\gamma_u}{\sqrt{\gamma_u}} \left\{ \frac{T_u}{T_{s_2}} - \frac{T_{e1}}{T_{s_2}} \right\} \\
 & + \epsilon_{\lambda_u} \frac{\sigma \times 10^{+12}}{q_s} \left( \frac{T_{s_2}}{1000} \right)^4 \left( \frac{T_u}{T_{s_2}} \right)^4 \tag{96}
 \end{aligned}$$

From Eq. 8 with Eqs. 17, 18, 23, 24, 52 and 65

$$\begin{aligned}
 & \frac{\sigma \times 10^{+12}}{q_s} \left( \frac{T_{s_2}}{1000} \right)^4 \left\{ \frac{1 - \rho_{\lambda_f 1}}{1 - \rho_{\lambda_f f} \rho_{\lambda_f 1}} \epsilon_{\lambda_f f} \left( \frac{T_f}{T_{s_2}} \right)^4 - \frac{1 - \rho_{\lambda_1 f}}{1 - \rho_{\lambda_1 1} \rho_{\lambda_1 f}} \epsilon_{\lambda_1 1} \left( \frac{T_1}{T_{s_2}} \right)^4 \right\} \\
 & - \frac{16}{2m} \left( \frac{k_2 T_{s_2}}{q_s} \right) \left( \frac{k}{k_2} \right) \left( \frac{T_1}{T_{s_2}} - \frac{T_e}{T_{s_2}} \right) \\
 & = \frac{.4897}{\sqrt{x}} \left( \frac{k_2 T_{s_2}}{q_s} \right) \left( \frac{k}{k_2} \right) \sqrt{\frac{N_R}{x}} \frac{Y_1}{1 \sqrt{Y_1}} \left\{ \frac{T_1}{T_{s_2}} - \frac{T_{e1}}{T_{s_2}} \right\} \\
 & + \epsilon_{\lambda_1} \frac{\sigma \times 10^{+12}}{q_s} \left( \frac{T_{s_2}}{1000} \right)^4 \left( \frac{T_1}{T_{s_2}} \right)^4 \quad (97)
 \end{aligned}$$

From Section 11.1.4, Eq. 32 and Section 11.1.5, Eq. 39

$$\frac{T_{e1}}{T_{s_2}} \approx 1 \approx \frac{T_e}{T_s} \quad (98)$$

In the last term of the first part of Eq. 95 put

$$\left. \begin{aligned} \frac{Y_u}{\sqrt{Y_u}} &\approx \sqrt{Y_u} \\ \frac{Y_1}{\sqrt{Y_1}} &\approx \sqrt{Y_1} \end{aligned} \right\} \quad (99)$$

In the first term of the second part of Eq. 95 consider the factor

$$\frac{k}{k_2} \sqrt{\gamma_f \frac{\mu_2}{\mu}}$$

By definition of Prandtl number  $N_p$

$$\frac{\mu_2}{\mu} = \frac{k_2}{k} \frac{(N_p)_2}{N_p} \quad (100)$$

and from Eq. 40

$$\gamma_f = \frac{\left( \frac{T_f}{T_{s_2}} \right)}{\left( \frac{T}{T_s} \right) \left( \frac{T_s}{T_{s_2}} \right)} \frac{\frac{T}{T_s} \frac{T_s}{T_{s_2}} + \frac{216}{T_{s_2}}}{\frac{T_f}{T_{s_2}} + \frac{216}{T_{s_2}}}$$

Hence,

$$\frac{k}{k_2} \sqrt{\gamma_f \frac{\mu_2}{\mu}} = \sqrt{\frac{k}{k_2} \frac{(N_p)_2}{N_p}} \sqrt{\frac{\frac{T_s}{T_{s_2}} \frac{T}{T_s} + \frac{216}{T_{s_2}}}{\frac{T_f}{T_{s_2}} + \frac{216}{T_{s_2}}}} \sqrt{\frac{\left( \frac{T_f}{T_{s_2}} \right)}{\frac{T_s}{T_{s_2}} \left( \frac{T_f}{T_{s_2}} + \frac{216}{T_{s_2}} \right)}} \quad (101)$$

and since

$$\frac{T}{T_s} = \frac{1}{1 + \frac{\gamma-1}{2} M^2}$$

$$.3 \leq M \leq 1$$

then, to a sufficiently good approximation

$$\frac{k}{k_2} \sqrt{\gamma_f \frac{\mu_2}{\mu}} \approx \sqrt{\frac{k}{k_2} \frac{(N_P)_2}{N_P} \left( \frac{T_f}{T_{s_2}} \right)^{1/4} \sqrt{\frac{T_s}{T_{s_2}} + \frac{216}{T_{s_2}}} \over \left( \frac{T_s}{T_{s_2}} \right)^{1/4} \sqrt{\frac{T_f}{T_{s_2}} + \frac{216}{T_{s_2}}}} \quad (102)$$

The Eqs. 95, 96, and 97 by means of the approximations, Eqs. 98, 99, and 100, become

$$\begin{aligned} y_2 \left( \frac{N_R}{x} \right)_2 (N_P)_2 \left( \frac{k_2 T_{s_2}}{q_s} \right)^d \left( \frac{T_s}{T_{s_2}} \right) - \frac{dx}{dx} = \eta_0 - \frac{\sigma \times 10^{12}}{q_s} \left( \frac{T_{s_2}}{1000} \right)^4 \left\{ \epsilon_{\lambda_u} \left( \frac{T_u}{T_{s_2}} \right)^4 + \epsilon_{\lambda_1} \left( \frac{T_1}{T_{s_2}} \right)^4 \right\} \\ - \frac{.4897}{\sqrt{x}} \left( \frac{k_2 T_{s_2}}{q_s} \right) \left( \frac{k_1}{k_2} \right) \sqrt{\left( \frac{N_R}{x} \right)_1} \sqrt{\frac{\frac{T_1}{T_{s_2}} + \frac{216}{T_{s_2}}}{\left( \frac{T_1}{T_{s_2}} \right)^{1/4} \left\{ \frac{\left( \frac{T_u}{T_{s_2}} \right)^{1/4} \left( \frac{T_u}{T_{s_2}} - 1 \right)}{\sqrt{\frac{T_u}{T_{s_2}} + \frac{216}{T_{s_2}}}} \right.}} \\ \left. + \frac{\left( \frac{T_1}{T_{s_2}} \right)^{1/4} \left( \frac{T_1}{T_{s_2}} - 1 \right)}{\sqrt{\frac{T_1}{T_{s_2}} + \frac{216}{T_{s_2}}}} \right\} \\ - \frac{1.1830}{\sqrt{\frac{y}{y_2} \sqrt{\frac{x}{y}}}} \left( \frac{k_2 T_{s_2}}{q_s} \right) \frac{y_2 \left( \frac{N_R}{x} \right)_2}{y_2} \sqrt{\frac{k(N_P)_2}{k_2 N_P} \sqrt{\frac{T_s}{T_{s_2}} + \frac{216}{T_{s_2}}} \left( \frac{T_s}{T_{s_2}} \right)^{1/4} \frac{\left( \frac{T_f}{T_{s_2}} \right)^{1/4} \left( \frac{T_f}{T_{s_2}} - \frac{T_s}{T_{s_2}} \right)}{\sqrt{\frac{T_f}{T_{s_2}} + \frac{216}{T_{s_2}}}}} \\ + \frac{32}{y_2} \frac{y_2}{2m} \left( \frac{k_2 T_{s_2}}{q_s} \right) \left( \frac{k}{k_2} \right) \left\{ \frac{\frac{T_u}{T_{s_2}} + \frac{T_1}{T_{s_2}}}{2} - \frac{T_s}{T_{s_2}} \right\} \end{aligned} \quad (103)$$

$$\begin{aligned}
& \frac{\sigma \times 10^{-12}}{q_s} \left( \frac{T_{s_2}}{1000} \right)^4 \left\{ \frac{1 - \rho_{\lambda_f u}}{1 - \rho_{\lambda_f f} \rho_{\lambda_f u}} \epsilon_{\lambda_f} \left( \frac{T_f}{T_{s_2}} \right)^4 \right. \\
& \quad \left. - \frac{1 - \rho_{\lambda_u f}}{1 - \rho_{\lambda_u u} \rho_{\lambda_f f}} \epsilon_{\lambda_u} \left( \frac{T_u}{T_{s_2}} \right)^4 \right\} \\
& - \frac{16}{y_2} \frac{y_2}{2m} \left( \frac{k_2 T_{s_2}}{q_s} \right) \left( \frac{k}{k_2} \right) \left( \frac{T_u}{T_{s_2}} - \frac{T_s}{T_{s_2}} \right) \alpha_{\lambda_s u} \left\{ 1 + \frac{\epsilon_{\lambda_s u} \rho_{\lambda_f f}}{1 - \rho_{\lambda_s u} \rho_{\lambda_f f}} \right\} \\
& = \frac{.4897}{\sqrt{x}} \left( \frac{k_2 T_{s_2}}{q_s} \right) \left( \frac{k_1}{k_2} \right) \left( \frac{N_R}{x} \right) \frac{\sqrt{\frac{T_1}{T_{s_2}} + \frac{216}{T_{s_2}}}}{\left( \frac{T_1}{T_{s_2}} \right)^{1/4}} \frac{\left( \frac{T_u}{T_{s_2}} \right)^{1/4} \left( \frac{T_u}{T_s} - 1 \right)}{\sqrt{\frac{T_u}{T_{s_2}} + \frac{216}{T_{s_2}}}} \\
& + \epsilon_{\lambda_u} \frac{\sigma \times 10^{+12}}{q_s} \left( \frac{T_{s_2}}{1000} \right)^4 \left( \frac{T_u}{T_{s_2}} \right)^4
\end{aligned} \tag{104}$$

$$\begin{aligned}
& \frac{\sigma \times 10^{+12}}{q_s} \left( \frac{T_{s_2}}{1000} \right)^4 \left\{ \frac{1 - \rho_{\lambda_f 1}}{1 - \rho_{\lambda_f f} \rho_{\lambda_f 1}} \epsilon_{\lambda_f} \left( \frac{T_f}{T_{s_2}} \right)^4 \right. \\
& \quad \left. - \frac{1 - \rho_{\lambda_1 f}}{1 - \rho_{\lambda_1 1} \rho_{\lambda_1 f}} \epsilon_{\lambda_1} \left( \frac{T_1}{T_{s_2}} \right)^4 \right\} \\
& - \frac{16}{y_2} \frac{y_2}{2m} \left( \frac{k_2 T_{s_2}}{q_s} \right) \left( \frac{k}{k_2} \right) \left( \frac{T_1}{T_{s_2}} - \frac{T_s}{T_{s_2}} \right) \\
& = \frac{.4897}{\sqrt{x}} \left( \frac{k_2 T_{s_2}}{q_s} \right) \frac{k_1}{k_2} \sqrt{\left( \frac{N_R}{x} \right)} \frac{\sqrt{\frac{T_1}{T_{s_2}} + \frac{216}{T_{s_2}}}}{\left( \frac{T_1}{T_{s_2}} \right)^{1/4}} \frac{\left( \frac{T_1}{T_{s_2}} \right)^{1/4} \left( \frac{T_1}{T_{s_2}} - 1 \right)}{\sqrt{\frac{T_1}{T_{s_2}} + \frac{216}{T_{s_2}}}} \\
& + \epsilon_{\lambda_1} \frac{\sigma \times 10^{+12}}{q_s} \left( \frac{T_{s_2}}{1000} \right)^4 \left( \frac{T_1}{T_{s_2}} \right)^4
\end{aligned} \tag{105}$$



The approximations, Eqs. 98, 99, and 100, achieve an important simplification by rendering Eqs. 103, 104 and 105 independent of Mach number.

From Eqs. 29, 30

$$\frac{P_s}{P_{s_2}} \sqrt{\frac{T_s}{T_{s_2}}} = \frac{A_2}{A} \frac{M_2}{M} \left\{ \frac{1 + \frac{\gamma-1}{2} M^2}{1 + \frac{\gamma-1}{2} M_2^2} \right\}^{\frac{\gamma+1}{2(\gamma-1)}} \quad (106)$$

$$\log \left\{ \sqrt{\frac{T_s}{T_{s_2}}} \sqrt{\frac{1 + \frac{\gamma-1}{2} M_2^2}{1 + \frac{\gamma-1}{2} M^2}} \frac{M_2}{M} \frac{1 + \gamma M^2}{1 + \gamma M_2^2} \right\}$$

$$= \int_2 \frac{\gamma M^2}{1 + \gamma M^2} \left\{ \frac{dA}{\gamma M^2 A} - \frac{f}{2m} dx \right\} \quad (107)$$

and from Eqs. 44, 47, and 94

$$\begin{aligned} \frac{f}{2m} &= \frac{1.328}{y_2 \sqrt{y_2 \left( \frac{N_R}{x} \right)}} \frac{\frac{T_2}{T_{s_2}} + \frac{216}{T_{s_2}}}{\left( \frac{T_2}{T_{s_2}} \right)^{1/4} \sqrt{1 + \frac{\gamma-1}{2} M_2^2}} \frac{\sqrt{1 + \frac{\gamma-1}{2} M^2}}{\frac{y}{y_2} \sqrt{\frac{x_f}{y}} \sqrt{1 + \frac{x_p}{x_f}}} \\ &\times \frac{\left( \frac{T_f}{T_{s_2}} \right)^{1/4}}{\sqrt{\frac{T_f}{T_{s_2}} + \frac{216}{T_{s_2}}}} \sqrt{\frac{T_s}{T_{s_2}}} + \frac{.02}{2m} \end{aligned} \quad (108)$$

$$\frac{dA}{A} = \frac{\frac{d}{dx} \left( \frac{y}{y_2} \right)}{\frac{y}{y_2}} dx \quad (109)$$

The solution of Eqs. 103, 104 and 105 with Eq. 51 determine  $T_s$ ,  $T_u$ ,  $T_1$ , and  $T_f$  as functions of  $x$ . Then Eq. 30 determines  $M$  as a function of  $x$ ; finally, Eq. 29 determined  $P_s$  also as a function of  $x$ . These results complete the analysis of the collector-transfer section except with respect to the drag of the external stream and with respect to the optimum length of the collector-transfer section.

#### 11.2 Performance of the Inlet Diffuser

The inlet diffuser configuration considered is shown in Fig. 20 and is discussed in Ref. 9. The critical performance parameter of the diffuser is the stagnation pressure ratio between the stations 1 and 2,

$$R_{Pd} = \frac{P_{s_2}}{P_{s_1}} \quad (110)$$

In this analysis,  $R_{Pd}$  is assumed to be a known constant. The flow is assumed adiabatic from station 1 to station 2, thus

$$T_{s_2} = T_{s_1} \quad (111)$$

By means of Eq. 35

$$\frac{y_2}{y_1} = \frac{\bar{m}(M_1)}{\bar{m}(M_2)} \frac{1}{R_{Pd}} \quad (112)$$

The geometry of the asymmetrical inlet and the subsonic diffuser yield

$$x_d = y_1 \left\{ \left( \frac{x_{1t}}{y_1} \right) + \frac{\left( \frac{y_2}{y_1} \right) - 1}{2 \tan \theta_d} \right\} \quad (113)$$

### 11.3 Design of the Jet Nozzle and the Determination of Net Thrust

For the flow from station 3 to the jet outlet at station 4

$$\frac{P_4}{P_1} = R_P \left\{ \frac{1 + \frac{\gamma-1}{2} M_1^2}{1 + \frac{\gamma-1}{2} M_4^2} \right\}^{\frac{\gamma}{\gamma-1}} \quad (114)$$

$$R_P = \frac{P_{s4}}{P_{s1}} = R_{P_d} R_{P_h} R_{P_n} \quad (115)$$

$$\frac{T_4}{T_1} = R_{T_h} \frac{1 + \frac{\gamma-1}{2} M_1^2}{1 + \frac{\gamma-1}{2} M_4^2} \quad (116)$$

$$R_{T_h} = \frac{T_{s3}}{T_{s2}} \quad (117)$$

$$y_{4t} = y_3 \bar{m} (M_3) \frac{1}{R_{P_{nc}}} \quad (118)$$

$$y_4 = y_1 \frac{\bar{m} (M_1) \sqrt{R_{T_h}}}{\bar{m} (M_4) R_P} \quad (119)$$

The net thrust per unit span due to the change of momentum of the internal stream from station 1 to station 4 is

$$F = \gamma_1 \rho_1 u_1 (u_4 - u_1) \quad (120)$$

$$u_4 = M_4 a_1 \sqrt{\frac{T_4}{T_1}} \quad (121)$$

$$u_1 = M_1 a_1 \quad (122)$$

For convenience and near optimum performance

$$P_4 = P_1 \quad (123)$$

Hence, by means of Eqs. 114, 116, 121, 122, and 123, Eq. 120 becomes

$$F = 2q\gamma_1 \left\{ \sqrt{\frac{2R_T}{(\gamma-1) M_1^2}} \sqrt{\left[1 + \frac{\gamma-1}{2} M_1^2\right] - \left(\frac{1}{R_P}\right)^{\frac{\gamma-1}{\gamma}} - 1} \right\} \quad (124)$$

where

$$q = 1/2 \rho \cdot u_1^2 \quad (125)$$

#### 11.4 Estimation of the Drag of the Wing External Surface

The drag of the wing external surface is estimated as the sum of a pressure drag and a boundary layer friction. The pressure drag coefficient according to the Busemann theory as given in Ref. 10, Chapter 7, Eqs. 266 and 267 is

$$C_{D_p} = \frac{C_L^2}{4\Gamma_1} + \frac{\Gamma_2}{2\Gamma_1} (F_2 - D_2) C_L + C_{D_o} \quad (126)$$

$$C_{D_o} = 2\Gamma_1 (F_2 + D_2) + 2\Gamma_2 (F_3 - D_3) \quad (127)$$

where

$$\Gamma_1 = \frac{1}{\sqrt{M_1^2 - 1}} \quad (128)$$

$$\Gamma_2 = \frac{1}{M_1^2 - 1} \left[ \frac{(\gamma + 1)M_1^4}{4(M_1^2 - 1)} - 1 \right] \quad (129)$$

and where according to Eqs. 255 and 260 of Ref. 10 for the outside surfaces of the particular case of a symmetrical profile shown in Fig. 1

$$x_c F_2 = x_c D_2 = \left( \frac{y_2 - y_1}{2x_2} \right)^2 x_2 + \frac{1}{4} \left( \frac{y_3 - y_2}{x_3 - x_2} \right)^2 (x_3 - x_2) + \frac{1}{4} \left( \frac{y_4 - y_3}{x_4 - x_3} \right)^2 (x_4 - x_3) \quad (130)$$

$$x_c F_3 = x_c D_3 = \left( \frac{y_2 - y_1}{2x_2} \right)^3 x_2 + \frac{1}{8} \left( \frac{y_3 - y_2}{x_3 - x_2} \right)^3 (x_3 - x_2) + \frac{1}{8} \left( \frac{y_4 - y_3}{x_4 - x_3} \right)^3 (x_4 - x_3) \quad (131)$$

Hence,

$$C_{D_p} = \frac{C_L^2}{4\Gamma_1} + C_{D_o} \quad (132)$$

$$C_{D_o} = 4\Gamma_1 F_2 + 4\Gamma_2 F_3 \quad (133)$$

$$\begin{aligned}
C_{D_o} &= \Gamma_1 \frac{x_2}{x_c} \left( \frac{y_2 - y_1}{x_2} \right)^2 \left[ 1 + \frac{2}{2\Gamma_1} \frac{y_2 - y_1}{x_2} \right] \\
&+ \Gamma_1 \frac{x_3 - x_2}{x_c} \left( \frac{y_3 - y_2}{x_3 - x_2} \right)^2 \left[ 1 + \frac{\Gamma_2}{2\Gamma_1} \frac{y_3 - y_2}{x_3 - x_2} \right] \\
&+ \frac{x_c - x_3}{x_c} \left( \frac{y_4 - y_3}{x_3 - x_2} \right)^2 \left[ 1 + \frac{\Gamma_2}{2\Gamma_1} \frac{y_4 - y_3}{x_c - x_3} \right] \quad (134)
\end{aligned}$$

Assuming laminar boundary layers, as on a flat plate, on both the upper and lower surfaces of the wing.

$$C_{D_f} = \frac{2.656}{\sqrt{x_c} \sqrt{\left( \frac{N_R}{x} \right)_1}} \quad (135)$$

The total wing drag per unit span is

$$\frac{1}{2} \rho u_1^2 x_c C_D \quad (136)$$

where

$$C_D = C_{D_p} + C_{D_f} = \frac{C_L^2}{4\Gamma_1} + C_{D_o} + C_{D_f} \quad (137)$$

11.5 Determination of Lengths of Inlet Diffuser, Collector-  
Transfer and Jet Nozzle Section for Maximum  $w/x_c$

In a condition of steady flight

$$F = q x_c C_D \quad (138)$$

$$w = q x_c C_L \quad (139)$$

Where  $F$  and  $w$  are the thrust available and the aircraft weight both per unit span and where, from Eq. 137

$$C_D = \frac{C_L^2}{4 \Gamma_1} + C_{Do} + C_{Df} \quad (140)$$

On eliminating  $C_L$  between Eqs. 138, 139 and 140 we have

$$\frac{1}{4 \Gamma_1 q^2} \left( \frac{w}{x_c} \right)^2 = \frac{F}{q x_c} - C_{Do} - C_{Df} \quad (141)$$

As in Fig. 1, put

$$\left. \begin{aligned} l_2 &= x_2 \\ l_3 &= x_3 - x_2 \\ l_4 &= x_4 - x_3 \end{aligned} \right\} \quad (142)$$

where

$$l_2 + l_3 + l_4 = x_c$$

Now, collecting results

$$\left. \begin{aligned} F &= F(l_3) \\ C_{Do} &= C_{Do}(l_2, l_3, l_4, x_c) \\ C_{Df} &= C_{Df}(x_c) \\ l_2 + l_3 + l_4 &= x_c \end{aligned} \right\} \quad (143)$$

We seek now the set of  $l_2, l_3, l_4$  which maximize the quantity  $\frac{1}{4\Gamma_1 q^2} \left(\frac{w}{x_c}\right)^2$  and thus also maximizes the quantity  $\frac{w}{x_c}$  subject

to Eq. 141 and the restriction, Eq. 143. For this purpose put

$$F = \frac{F}{q x_c} - C_{Do} - C_{Df} + \lambda(l_2 + l_3 + l_4 - x_c) \quad (144)$$

$$\frac{\partial F}{\partial l_2} = - \frac{\partial C_{Do}}{\partial l_2} + \lambda = 0 \quad (145)$$

$$\frac{\partial F}{\partial l_3} = \frac{1}{q x_c} \frac{\partial F}{\partial l_3} - \frac{\partial C_{Do}}{\partial l_3} + \lambda = 0 \quad (146)$$

$$\frac{\partial F}{\partial l_4} = - \frac{\partial C_{Do}}{\partial l_4} + \lambda = 0 \quad (147)$$

$$\frac{\partial F}{\partial x_c} = - \frac{F}{q x_c^2} - \frac{\partial C_{Do}}{\partial x_c} - \frac{\partial C_{Df}}{\partial x_c} - \lambda = 0 \quad (148)$$

Where from Eq. 134

$$\frac{\partial C_{Do}}{\partial l_2} = - \frac{\Gamma_1}{x_c} \left(\frac{y_2 - y_1}{l_2}\right)^2 \left[ 1 + \frac{\Gamma_2}{1} \left(\frac{y_2 - y_1}{l_2}\right) \right] \quad (149)$$

$$\frac{\partial C_{Do}}{\partial l_3} = - \frac{\Gamma_1}{x_c} \left(\frac{y_3 - y_2}{l_3}\right)^2 \left[ 1 + \frac{\Gamma_2}{1} \left(\frac{y_3 - y_2}{l_3}\right) \right] \quad (150)$$

$$\frac{\partial C_{Do}}{\partial l_4} = - \frac{\Gamma_1}{x_c} \left(\frac{y_4 - y_3}{l_4}\right)^2 \left[ 1 + \frac{\Gamma_2}{1} \left(\frac{y_4 - y_3}{l_4}\right) \right] \quad (151)$$

$$\frac{\partial C_{Do}}{\partial x_c} = - \frac{C_{Do}}{x_c} \quad (152)$$



and from Eq. 135

$$\frac{\partial C_{Df}}{\partial x_c} = \frac{C_{Df}}{2 x_c} \quad (153)$$

From Eqs. 145, 147, 149 and 151

$$\frac{\partial C_{Do}}{\partial l_2} = \frac{\partial C_{Do}}{\partial l_4} \quad (154)$$

and

$$\frac{|y_2 - y_1|}{l_2} = \frac{|y_4 - y_3|}{l_4} \quad (155)$$

From Eqs. 146, 147, 148, with Eqs. 150, 151, 152 and 153

$$\frac{1}{q} \frac{\partial T}{\partial l_3} + \Gamma_1 \left( \frac{y_3 - y_2}{l_3} \right)^2 \left\{ 1 + \frac{\Gamma_2}{1} \left( \frac{y_3 - y_2}{l_3} \right) \right\} + \lambda x_c = 0 \quad (156)$$

$$\lambda x_c = -\Gamma_1 \left( \frac{y_4 - y_3}{l_4} \right)^2 \left\{ 1 + \frac{\Gamma_2}{1} \left( \frac{y_4 - y_3}{l_4} \right) \right\} \quad (157)$$

$$\frac{F}{q} - C_{Do} x_c - \frac{1}{2} C_{Df} x_c + \lambda x_c^2 = 0 \quad (158)$$

The Eqs. 155, 156, 157, 158, and 142 determine  $\lambda$ ,  $l_2$ ,  $l_3$ ,  $l_4$ , and  $x_c$  for  $\left( \frac{w}{x_c} \right)$  a maximum. Then,

$$\left( \frac{w}{x_c} \right)_a = 2q \sqrt{1 \left\{ \frac{F}{qx_c} - C_{Do} - C_{Df} \right\}} \quad (159)$$

## 12. PERFORMANCE ANALYSIS SEQUENCE

12.1 Throughout the analysis the following quantities are assumed constant:

$$q_g = 92.4 \text{ ft lb/ft}^2 \text{ sec}$$

$$\gamma = 1.40$$

$$C_{p, \text{air}} = 6.01 \times 10^3 \text{ ft lb/slug } ^\circ\text{R}$$

$$\sigma = 374 \times 10^{-12} \text{ ft lb/ft}^2 \text{ sec } ^\circ\text{R}^4$$

12.2 The properties of air

$$\mu = \text{viscosity (lb sec/ft}^2\text{)}$$

$$k = \text{thermal conducting (ft lb/ft sec } ^\circ\text{R)}$$

$$N_p = \text{Prandtl number}$$

are plotted from Ref. 11 in Figs. 25, 26, and 27.

12.3 Choose the following sets of quantities:

a.  $Z, M_1, y_1$

b.  $M_2, R_{pd}, w/y_1$

c.  $Y/y_2, x_f/y$  both as functions of distance along the collector-transfer section

d.  $x_p/x_f, \eta_o, E_{ff}, E_{uu}, E_{11}, E_{uf}, E_{1f}, E_{su}$

12.4 From the ARDC Standard Atmosphere obtain  $a_1, \mu_1, \rho_1, T_1$  and  $P_1$  corresponding to the altitude  $Z$ .

12.5 Compute  $u_1, (N_R/x)_1, T_{s_1} = T_{s_2}$

$$u_1 = M_1 a_1 \quad (160)$$

$$\left(\frac{N_R}{x}\right)_1 = \frac{u_1 \rho_1}{\mu_1} \quad (161)$$

$$T_{s_1} = T_{s_2} = T_1 \left\{ 1 + \frac{\gamma - 1}{2} M_1^2 \right\} \quad (162)$$

12.6 Compute  $y_2$ ,  $T_2$ ,  $u_2$ ,  $P_2/P_1$ ,  $\rho_2$

$$y_2 = y_1 \frac{\bar{m}(M_1)}{\bar{m}(M_2)} \frac{1}{R_{Pd}} \quad (163)$$

where  $\bar{m}(M) = 1/(A/A^*)$  and  $(A/A^*)$  is given in Table I of Ref. 6

$$T_2 = T_1 \frac{1 + \frac{\gamma - 1}{2} M_1^2}{1 + \frac{\gamma - 1}{2} M_2^2} \quad (164)$$

$$u_2 = M_2 a_1 \sqrt{\frac{T_2}{T_1}} \quad (165)$$

$$\frac{P_2}{P_1} = R_{Pd} \left( \frac{T_2}{T_1} \right)^{\frac{\gamma}{\gamma - 1}} \quad (166)$$

$$\rho_2 = \rho_1 \frac{P_2}{P_1} \frac{T_1}{T_2} \quad (167)$$

12.7 Obtain  $\mu_2$ ,  $k_1$ ,  $k_2$  and  $(N_p)_2$  from the properties of air in Figs. 25, 26, and 27.

12.8 Compute

$$\eta_o = \frac{\tau_{\lambda_s u} (1 - \rho_{\lambda_s f})}{1 - \rho_{\lambda_s u} \rho_{\lambda_s f}} + \alpha_{\lambda_s u} \left\{ 1 + \frac{\tau_{\lambda_s u} \rho_{\lambda_s f}}{1 - \rho_{\lambda_s u} \rho_{\lambda_s f}} \right\} \quad (168)$$

$$\left(\frac{N_R}{x}\right)_2 = \frac{u_2 \rho_2}{\pi \mu_2} \quad (169)$$

$$\frac{k_2 T_{s_2}}{q_s}, \quad \frac{k_1}{k_2} \quad (170)$$

$$C_1 = \frac{\sigma \times 10^{12}}{q_s} \left(\frac{T_{s_2}}{1000}\right)^4 E_{ff} \quad (171)$$

$$E_{ff} = \frac{1 - \rho_{\lambda_f u}}{1 - \rho_{\lambda_f f} \rho_{\lambda_f u}} \epsilon_{\lambda_f} \quad (172)$$

$$C_2 = \frac{\sigma \times 10^{12}}{q_s} \left(\frac{T_{s_2}}{1000}\right)^4 E_{uu} \quad (173)$$

$$E_{uu} = \epsilon_{\lambda_u} \quad (174)$$

$$C_3 = \frac{\sigma \times 10^{12}}{q_s} \left(\frac{T_{s_2}}{1000}\right)^4 E_{11} \quad (175)$$

$$E_{11} = \epsilon_{\lambda_1} \quad (176)$$

$$C_4 = \frac{\sigma \times 10^{12}}{q_s} \left(\frac{T_{s_2}}{1000}\right)^4 E_{uf} \quad (177)$$

$$E_{uf} = \frac{1 - \rho_{\lambda_u f}}{1 - \rho_{\lambda_u u} \rho_{\lambda_f f}} \epsilon_{\lambda_u} \quad (178)$$

$$C_5 = \frac{\sigma \times 10^{12}}{q_s} \left( \frac{T_{s_2}}{1000} \right)^4 E_{1f} \quad (179)$$

$$E_{1f} = \frac{1 - \rho_{\lambda_1 f}}{1 - \rho_{\lambda_1} \rho_{\lambda_1 f}} \epsilon_{\lambda_1} \quad (180)$$

$$C_6 = E_{su} = \alpha_{\lambda_s u} \left\{ 1 + \frac{\tau_{\lambda_s u} \rho_{\lambda_s f}}{1 - \rho_{\lambda_s u} \rho_{\lambda_s f}} \right\} \quad (181)$$

$$C_7 = 1.1830 \left( \frac{k_2 T_{s_2}}{q_s} \right) \frac{\sqrt{y_2 \left( \frac{N_R}{x} \right)_2}}{y_2} \quad (182)$$

$$C_8 = \frac{32}{y_2} \left( \frac{k_2 T_{s_2}}{q_s} \right) \quad (183)$$

$$C_9 = .4897 \left( \frac{k_2 T_{s_2}}{q_s} \right) \left( \frac{k_1}{k_2} \right) \sqrt{\left( \frac{N_R}{x} \right)_1} \frac{\sqrt{\frac{T_1}{T_{s_2}} + \frac{216}{T_{s_2}}}}{\left( \frac{T_1}{T_{s_2}} \right)^{1/4}} \quad (184)$$

$$C_{10} = y_2 \left( \frac{N_R}{x} \right)_2 \left( \frac{N_P}{P} \right)_2 \frac{k_2 T_{s_2}}{q_s} \quad (185)$$

The data required for the solution of the equations of Article 9 are: the constants  $\eta_o$ ,  $216/T_{s_2}$ ,  $C_1$ ,  $C_2$ ,  $C_3$ ,  $C_4$ ,  $C_5$ ,  $C_6$ ,  $C_7$ ,  $C_8$ ,  $C_9$ ,  $C_{10}$ ,  $x_d$ ,  $(w/y_1)$ ,  $y_1/y_2$ , the plots of  $k$ ,  $N_p$  and the functions

$$\frac{y}{y_2}, \quad \frac{x_f}{y}$$

12.9

$$\begin{aligned} C_{10} \frac{dT_s^*}{dx} &= \eta_o - \left[ C_2 T_u^{*4} + C_3 T_1^{*4} \right] \\ &- \frac{C_9}{\sqrt{x}} \left\{ \frac{T_u^{*1/4} (T_u^* - 1)}{\sqrt{T_u^* + \frac{216}{T_{s_2}}}} + \frac{T_1^{*1/4} (T_1^* - 1)}{\sqrt{T_1^* + \frac{216}{T_{s_2}}}} \right\} \\ &= \frac{C_7}{\sqrt{\frac{y}{y_2}} \sqrt{\frac{x_f}{y}}} \sqrt{\frac{k}{k_2}} \frac{(N_p)_2}{N_p} \frac{\sqrt{T_s^* + \frac{216}{T_{s_2}}}}{T_s^{*1/4}} \frac{T_f^{*1/4} (T_f^* - T_s^*)}{\sqrt{T_f^* + \frac{216}{T_{s_2}}}} \\ &+ C_8 \frac{y_2}{2m} \frac{k}{k_2} \left\{ \frac{T_u^* + T_1^*}{2} - T_s^* \right\} \end{aligned} \quad (186)$$

$$\begin{aligned} C_1 T_f^{*4} - (C_2 + C_4) T_u^{*4} - 1/2 C_8 \frac{y_2}{2m} \frac{k}{k_2} (T_u^* - T_s^*) + E_{su} \\ = \frac{C_9}{\sqrt{x}} \frac{T_u^{*1/4} (T_u^* - 1)}{\sqrt{T_u^* + \frac{216}{T_{s_2}}}} \end{aligned} \quad (187)$$

$$C_1 T_f^{*4} - (C_3 + C_5) T_1^{*4} - 1/2 C_8 \frac{y_2}{2m} \frac{k}{k_2} (T_1^* - T_s^*)$$

$$= \frac{C_9}{\sqrt{x}} \frac{T_1^{*1/4} (T_1^* - 1)}{\sqrt{T_1^* + \frac{216}{T_{s_2}}}} \quad (188)$$

$$\frac{y}{2m} = \frac{\frac{y}{y_2} + \left(\frac{w}{y_1}\right) \left(\frac{y_1}{y_2}\right)}{2 \frac{y}{y_2} \left(\frac{w}{y_1}\right) \left(\frac{y_1}{y_2}\right)} \quad (189)$$

In order to integrate the first equation in 186, it is necessary first to determine a solution  $T_u^*$ ,  $T_1^*$  and  $T_f^*$  for the last equation of 186 with 187 and 188. For the latter purpose, for given  $T_s$  at  $x$  and a trial value of  $T_u^*$ , compute

$$T_1^* = T_u^* + \Delta T_u^* \quad (190)$$

where

$$\Delta T_u^* = \frac{C_6}{\left(\frac{\partial f_1}{\partial T_u^*}\right)} \quad (191)$$

$$\frac{\partial f_1}{\partial T_u^*} = -4(C_2 + C_4) T_u^{*3} - 1/2 C_8 \frac{y_2}{2m} \frac{k}{k_2}$$

$$- \frac{C_9}{\sqrt{x}} \frac{T_u^{*1/4}}{\sqrt{T_u^* + \frac{216}{T_{s_2}}}} \left\{ 1 - 1/4 \frac{\left(T_u^* - \frac{216}{T_{s_2}}\right) (T_u^* - 1)}{T_u^* \left(T_u^* + \frac{216}{T_{s_2}}\right)} \right\} \quad (192)$$

Then, with the available data compute

$$(T_f^*)_{\text{corrected}} = (T_f^*)_{\text{trial}} + \Delta T_f^* \quad (193)$$

where

$$\Delta T_f^* = - \frac{f_3 - f_2}{\left( \frac{\partial(f_3 - f_2)}{\partial T_f^*} \right)} \quad (194)$$

$$f_2 = \eta_o - \left[ C_2 T_u^{*4} + C_3 T_1^{*4} \right]$$

$$- \frac{C_9}{\sqrt{x}} \left\{ \frac{T_u^{*1/4} (T_u^* - 1)}{\sqrt{T_u^* + \frac{216}{T_{s2}}}} + \frac{T_1^{*1/4} (T_1^* - 1)}{\sqrt{T_1^* + \frac{216}{T_{s2}}}} \right\} \quad (195)$$

$$f_3 = \frac{C_7}{\sqrt{\frac{y}{y_2}} \sqrt{\frac{x_f}{y}}} \sqrt{\frac{k}{k_2} \frac{(N_p)_2}{N_p}} \frac{\sqrt{T_s^* + \frac{216}{T_{s2}}}}{T_s^{*1/4}} \frac{T_f^{*1/4} (T_f^* - T_s^*)}{\sqrt{T_f^* + \frac{216}{T_{s2}}}} \\ + C_8 \frac{y_2}{2m} \frac{k}{k_2} \left[ \frac{T_u^* + T_1^*}{2} - T_s^* \right] \quad (196)$$



$$\frac{\partial(f_3 - f_2)}{\partial T_f^*} = \frac{c_7}{\sqrt{\frac{y}{y_2}}} \sqrt{\frac{x_f}{y}} \frac{k}{k_2} \frac{(N_P)_2}{N_P} \frac{\sqrt{T_s^* + \frac{216}{T_{s_2}}}}{T_s^* + 1/4} \frac{T_f^{*1/4}}{\sqrt{T_f^* + \frac{216}{T_{s_2}}}}$$

$$\times \left\{ 1 - 1/4 \frac{\left( T_f^* - \frac{216}{T_{s_2}} \right) (T_f^* - T_s^*)}{T_f^* \left( T_f^* + \frac{216}{T_{s_2}} \right)} \right\} \quad (197)$$

and iterate until  $\Delta T_f^* = 0$

Now, compute with the available data

$$(T_u^*)_{\text{corrected}} = (T_u^*)_{\text{trial}} + \Delta T_u^* \quad (198)$$

where

$$\Delta T_u^* = - \frac{f_1}{\left( \frac{\partial f_1}{\partial T_u^*} \right)} \quad (199)$$

$$f_1 = c_1 T_f^{*4} - (c_2 + c_4) T_u^{*4} - 1/2 c_8 \frac{y_2}{2m} \frac{k}{k_2} (T_u^* - T_s^*)$$

$$+ c_6 - \frac{c_9}{\sqrt{x}} \frac{T_u^{*1/4} (T_u^* - 1)}{\sqrt{T_u^* + \frac{216}{T_{s_2}}}} \quad (200)$$

and iterate until  $\Delta T_u^* = 0$ . Finally, iterate the process starting with 190 and ending with 200 until  $T_u^*$  corrected obtained from 198 is the same as the  $T_u^*$  introduced as a trial value in 190.

In case the procedure involving the set of equations 192 - 200 does not converge, then the following procedure may be more convenient. Instead of 194 and 199 use iteratively

$$\Delta T_f^* = \frac{-f_4 \left( \frac{\partial(f_3 - f_2)}{\partial T_u^*} \right) + (f_3 - f_2) \frac{\partial f_1}{\partial T_u^*}}{\Delta} \quad (201)$$

$$\Delta T_u^* = \frac{-(f_3 - f_2) \frac{\partial f_1}{\partial T_f^*} + f_1 \frac{\partial(f_3 - f_2)}{\partial T_f^*}}{\Delta} \quad (202)$$

where

$$\Delta = \frac{\partial f_1}{\partial T_f^*} \cdot \frac{\partial(f_3 - f_2)}{\partial T_u^*} - \frac{\partial f_1}{\partial T_u^*} \frac{\partial(f_3 - f_2)}{\partial T_f^*} \quad (203)$$

$$\begin{aligned} \frac{\partial(f_3 - f_2)}{\partial T_u^*} = & C_8 \frac{y_2}{2m} \frac{k}{k_2} + 4C_2 T_u^{*3} + 4C_3 T_1^3 \\ & + \frac{C_9}{\sqrt{x}} \left[ \frac{T_u^{*1/4}}{\sqrt{T_u^* + \frac{216}{T_{s2}}}} \left\{ 1 - \frac{1}{4} \frac{\left( T_u^* - \frac{216}{T_{s2}} \right) (T_u^* - 1)}{T_u^* \left( T_u^* + \frac{216}{T_{s2}} \right)} \right\} \right. \\ & \left. + \frac{T_1^{*1/4}}{\sqrt{T_1^* + \frac{216}{T_{s2}}}} \left\{ 1 - \frac{1}{4} \frac{\left( T_1^* - \frac{216}{T_{s2}} \right) (T_1^* - 1)}{T_1^* \left( T_1^* + \frac{216}{T_{s2}} \right)} \right\} \right] \quad (204) \end{aligned}$$

$$\frac{\partial f_1}{\partial T_f^*} = 4C_1 T_f^{*3} \quad (205)$$

These processes yield the set

$$x, T_x^*, T_u^*, T_1^*, T_f^*, f_2 \quad (206)$$

which for given  $T_s$  at  $x$  satisfy the set of equations: the last of 186, 187 and 188.

Plots of the function

$$\frac{\sqrt{T + \frac{216}{T_{s2}}}}{T^{1/4}} \quad (207)$$

is a valuable aid in the computation according to Article 12.9.

12.10 Compute

$$T_{s(i+1)} = T_{s(i)} \int_{x_i}^{x_{i+1}} \frac{f_2}{C_{10}} dx \quad (208)$$

by means of "predictors" and "correctors". The "predictors" and "correctors" appropriate to the points

$$\left. \begin{aligned} x_1 &= x_d, x_2 = x_1 + \delta x, x_3 = x_2 + \delta x \\ x_4 &= x_3 + \delta x, x_{i+1} = x_i + \delta x \end{aligned} \right\} \quad (209)$$

are listed below. The value of  $T_{x(i+1)}$  is first estimated by means of the "predictors." Then, with this as the given value of  $T_s$  in Article 12.9, the set 201 is computed and in particular  $f_{2(i+1)}$  is computed which substituted in the "corrector" yields a corrected value of  $T_s$ . Iteration of this process will yield a set 201 which satisfy 208, 209, and 210.

At the first point

$$x_1 = x_d, T_s^* = 1 \quad (210)$$

$$(T_u^*)_{\text{first trial}} = 1, (T_f^*)_{\text{first trial}} = 1$$

At the second point

$$x_2 = x_1 + \delta x \quad (211)$$

$$(T_u^*)_{\text{first trial}} = T_{u_1}^*, (T_f^*)_{\text{first trial}} = T_{f_1}^*$$

"Predictors"

$$T_{s_2}^* = T_{s_1}^* + \frac{(f_2)_1}{C_{10}} \delta x \quad (212)$$

$$T_{s_3}^* = T_{s_2}^* + \frac{(f_2)_2}{C_{10}} \delta x \quad (213)$$

$$T_{s_4}^* = T_{s_3}^* + T \frac{(f_2)_3}{C_{10}} \delta x \quad (214)$$

$$T_{s(i+1)}^* = T_{s(i-3)}^* + 4/3 \frac{\delta x}{C_{10}} \left[ 2(f_2)_i - (f_2)_{(i-1)} + 2(f_2)_{(i-2)} \right]$$

$$i \geq 4 \quad (215)$$

"Correctors"

$$T_{s_2}^* = T_{s_1}^* + \frac{\delta x}{2C_{10}} \left[ (f_2)_2 + (f_2)_1 \right] \quad (216)$$

$$T_{s(i+1)}^* = T_{s(i-1)}^* + \frac{\delta x}{3C_{10}} \left\{ (f_2)_{(i+1)} + 4(f_2)_i + (f_2)_{(i-1)} \right\} \quad (217)$$

$$i \geq 2$$

12.11 Compute:

$$\log \left\{ \sqrt{T_s^*} \sqrt{\frac{1 + \frac{\gamma-1}{2} M_2^2}{1 + \frac{\gamma-1}{2} M^2}} \frac{M_2}{M} \frac{1 + \gamma M_2^2}{1 + \gamma M^2} \right\} \quad (218)$$

$$= \int_{x=x_d}^x \frac{\gamma M^2}{1 + \gamma M^2} \left\{ \frac{\frac{d\left(\frac{y}{y_2}\right)}{dx}}{\gamma M^2 \frac{y}{y_2}} - \frac{f}{2m} \right\} dx$$

where

$$\frac{f}{2m} = \left( \frac{.020}{y_2} \right) \left( \frac{y_2}{2m} \right) + C_{11} \frac{\sqrt{1 + \frac{\gamma-1}{2} M^2}}{\frac{y}{y_2} \sqrt{\frac{x_f}{y_2}} \sqrt{1 + \frac{x_p}{x_f}}} \frac{T_f^{*1/4}}{\sqrt{T_f^* + \frac{216}{T_{s_2}}}} \sqrt{T_s^*} \quad (219)$$

$$C_{11} = \frac{1.328}{y_2 \sqrt{y_2 \left( \frac{N_R}{x} \right)_2 \sqrt{1 + \frac{\gamma-1}{2} M_2^2}}} \frac{\sqrt{T_2^* + \frac{216}{T_{s_2}}}}{T_2^{*1/4}} \quad (220)$$

$$\gamma = 1.40$$

and where  $T_s^*$  and  $T_f^*$  are known functions of  $x$  tabulated as results of Articles 12.9 and 12.10

The input data for Article 12.11 are besides  $T_s^*$  and  $T_f^*$ , the constants

$$\frac{216}{T_{s_2}}, x_d, M_2, T_2^* = \frac{T_2}{T_{s_2}}, y_2, \left(\frac{N_R}{x}\right)_2 \quad (221)$$

and the functions

$$\frac{y}{y_2}, \frac{d\left(\frac{y}{y_2}\right)}{dx}, \frac{x_f}{y}, \frac{x_p}{x_f} \quad (222)$$

Denote the quantity of the left of 218 by  $I$  and denote the integrand on the right by  $I'$ . At the first point  $x_1 = x_d$

$$\left. \begin{array}{l} M = M_2 \\ I = 0 \end{array} \right\} \quad (223)$$

The method of solution proceeds by estimating at  $x = x_r$  a trial value of  $I_r$  which also determines a trial value of  $M_r$  from which in turn  $I_r$  is computed. Then by means of a "corrector" formula an improved value of  $I_r$  is computed. This process is repeated iteratively until the improved values is identical with the trial value. The first trial values are estimated by means of "predictor" formulas.

#### "Predictors"

$$I_2 = I_1 + I_1' \delta x \quad (224)$$

$$I_3 = I_2 + I_2' \delta x \quad (225)$$

$$I_4 = I_3 + I_3' \delta x \quad (226)$$

$$I_{(i+1)} = I_{(i-3)} + \frac{4\delta x}{3} \left\{ 2I_i^* - I^*_{(i-1)} + 2I^*_{(i-2)} \right\} \quad (227)$$

$$i \geq 4$$

"Correctors"

$$I_2 = I_1 + \frac{\delta x}{2} (I_2^* + I_1^*) \quad (228)$$

$$I_{(i+1)} = I_{(i-1)} + \frac{\delta x}{3} \left\{ I^*_{(i+1)} + 4I_i^* + I^*_{(i-1)} \right\} \quad (229)$$

$$i \geq 2$$

In computing the value of M for a given value of I, the correction to be added to a trial value of M is

$$\delta M = - \frac{M(1 + \gamma M^2)(1 + \frac{\gamma-1}{2} M^2)}{M^2 - 1} \delta I \quad (230)$$

$$M_{(\text{corrected})} = M_{\text{trial}} + I_M \quad (231)$$

$$\delta I = I - I_{\text{trial}} \quad (232)$$

12.12

$$P_s^* = \frac{\sqrt{\frac{T_s^*}{y_2}}}{\frac{y}{y_2}} \frac{M_2}{M} \left\{ \frac{1 + \frac{\gamma-1}{2} M^2}{1 + \frac{\gamma-1}{2} M_2^2} \right\}^{\frac{\gamma+1}{2(\gamma-1)}} \quad (233)$$

where  $T_s$  and M are known functions of x.

The results of Articles 11 and 12 to be tabulated are,

$$\begin{array}{ccc} x, & M, & P^* \\ \downarrow & \downarrow & \downarrow \end{array} \quad (234)$$

Plots of the following functions

$$\frac{1 + \gamma M^2}{M \sqrt{1 + \frac{\gamma-1}{2} M^2}}, \quad \frac{\gamma M^2}{1 + \gamma M^2}, \quad M (1 + \gamma M^2) (1 + \frac{\gamma-1}{2} M^2),$$

$$\frac{\left[ 1 + \frac{\gamma-1}{2} M^2 \right] \frac{\gamma+1}{2(\gamma-1)}}{M} \quad (235)$$

are useful in performing the computations according to Articles 12.11 and 12.12.

12.13

At  $x = x_3$  identify

$$y_3, R_T = T_{s_3}^*, \quad R_{P_h} = P_{s_3}^*, \quad M_3$$

from the results of Articles 12.10, 12.11, 12.12 compute:

$$R_P, M_4, y_4, F, \frac{\delta F}{\delta x}$$

$$R_P = R_{P_d} R_{P_h} \quad (236)$$

$$M_4 = \sqrt{\frac{2}{\gamma-1} \left[ R_P \frac{\gamma-1}{\gamma} (1 + \frac{\gamma-1}{2} M_1^2) - 1 \right]} \quad (237)$$

$$y_4 = y_1 \frac{M_1}{M_4} \left[ \frac{(1 + \frac{\gamma-1}{2} M_4^2)}{(1 + \frac{\gamma-1}{2} M_1^2)} \right]^{\frac{\gamma+1}{2(\gamma-1)}} \sqrt{\frac{R_T}{R_P}} \quad (238)$$



$$F = 2qy_1 \left[ \sqrt{\frac{2R_T}{(\gamma-1)M_1^2}} \sqrt{\left[1 + \frac{\gamma-1}{2} M_1^2\right] - \left(\frac{1}{R_P}\right)^{\frac{\gamma-1}{\gamma}} - 1} \right] \quad (239)$$

$$q = \frac{1}{2} \rho_1 u_1^2 \quad (240)$$

$$\frac{\delta F}{\delta x} = \frac{1}{2\delta x} \left[ F_{i-2} - 4F_{i-1} + 3F_i \right] \quad (241)$$

In 241, the value of  $F_i$  occurs at  $x = x_3$  and the values  $F_i, F_{i-2}$  occur at the two previous stations  $x$ .

12.14 Determine  $l_2, l_3, l_4$  and  $x_c$  from the system of equations,

$$\frac{|y_2 - y_1|}{l_2} = \frac{|y_4 - y_3|}{l_4} \quad (242)$$

$$\frac{1}{q} \frac{\delta F}{\delta l_3} + \Gamma_1 \left( \frac{y_3 - y_2}{l_3} \right)^2 \left\{ 1 + \frac{\Gamma_2}{\Gamma_1} \frac{y_3 - y_2}{l_3} \right\} + \lambda x_c = 0 \quad (243)$$

$$\lambda x_c = -\Gamma_1 \left( \frac{y_4 - y_3}{l_4} \right)^2 \left\{ 1 + \frac{\Gamma_2}{\Gamma_1} \frac{y_4 - y_3}{l_4} \right\} \quad (244)$$

$$\frac{1}{q} F - C_{D_o} x_c - 1/2 C_{D_f} x_c + \lambda x_c^2 = 0 \quad (245)$$

$$l_2 + l_3 + l_4 = x_c \quad (246)$$

where

$$\begin{aligned}
C_{D_o} = & \Gamma_1 \frac{l_2}{x_c} \left\{ \frac{y_2 - y_1}{l_2} \right\}^2 \left[ 1 + \frac{\Gamma_2}{2\Gamma_1} \frac{y_2 - y_1}{l_2} \right] \\
& + \Gamma_1 \frac{l_3}{x_c} \left\{ \frac{y_3 - y_2}{l_3} \right\}^2 \left[ 1 + \frac{\Gamma_2}{2\Gamma_1} \frac{y_3 - y_2}{l_3} \right] \\
& + \Gamma_1 \frac{l_4}{x_c} \left\{ \frac{y_4 - y_3}{l_4} \right\}^2 \left[ 1 + \frac{\Gamma_2}{2\Gamma_1} \frac{y_4 - y_3}{l_4} \right]
\end{aligned} \tag{247}$$

$$C_{D_f} = \frac{2.656}{\sqrt{x_c} \sqrt{\left(\frac{N_R}{x}\right)_1}} \tag{248}$$

$$\Gamma_1 = \frac{1}{\sqrt{M_1^2 - 1}} \tag{249}$$

$$\Gamma_2 = \frac{1}{M_1^2 - 1} \left[ \frac{(\gamma + 1) M_1^4}{4(M_1^2 - 1)} - 1 \right] \tag{250}$$

$$l_3 = x_3 - x_d \tag{251}$$

In order to solve the system of equations 242, 243, 244, 245, and 246, compute  $(y_3 - y_2)/l_3$  and substitute in 243 which determines  $\lambda x_c$ . Then, compute  $(y_4 - y_3)/l_4$  from 244 and hence  $(y_2 - y_1)/l_2$  is known from 242. From these results compute  $l_2, l_3, l_4$ .

In computing the value of  $(y_4 - y_3)/l_4$  from 244 the correction to be added to a trial value of  $(y_4 - y_3)/l_4$  is

$$\delta \left( \frac{y_4 - y_3}{l_4} \right) = \frac{\delta(\lambda x_c)}{2 \Gamma_1 \frac{y_4 - y_3}{l_4} \left\{ 1 + \frac{\Gamma_2}{\Gamma_1} \frac{y_4 - y_3}{l_4} \right\}} \quad (252)$$

where

$$\delta(\lambda x_c) = - \left[ \Gamma_1 \left( \frac{y_4 - y_3}{l_4} \right)^2 \left\{ 1 + \frac{\Gamma_2}{\Gamma_1} \frac{y_4 - y_3}{l_4} \right\} + \lambda x_c \right] \quad (253)$$

Finally, compute

$$\delta x_c = (l_2 + l_3 + l_4) - \frac{\frac{1}{q} F - C_{D_o} x_c}{1/2 C_{Df} - (\lambda x_c)} \quad (254)$$

The computations of Articles 12.10, 12.11, 12.12, and 12.13 are to be carried to the  $x = x_3$  at which  $\delta x_c = 0$ .

The input data for Articles 12.13 and 12.14 include besides  $y_3, T_{s_3}^*, P_{s_3}^*, M_3$  also the constants

$$R_{p_d}, M_1, y_1, q, y_2, \left( \frac{N_R}{x} \right)_1$$

The results of Article 12.14 to be tabulated are:

$$y_3, y_4, l_2, l_3, l_4, x_c, \frac{F}{q x_c}, C_{D_o}, C_{Df}, 1$$

all at the value of  $x_3$  for which  $\delta x_c = 0$ .

12.15 Compute, finally

$$\frac{w}{x_c} = 2q \sqrt{1 - \left\{ \frac{F}{q x_c} - C_{D_o} - C_{Df} \right\}} \quad (255)$$

### 13. SOLAR ENERGY COLLECTION<sup>1</sup>

A major part of the effort on this contract has been concerned with investigating lightweight, high efficiency solar energy collectors, which can be combined with a suitable heat exchanger for the purpose of absorbing energy from the sun and transferring it to a working fluid with the highest possible efficiency. A great deal of research effort has been expended for many years in the development of various types of solar energy collectors. However, no devices had previously been developed with performance approaching the requirements of this program. The solar energy collectors to be used for the present application must conform to extremely rigid requirements if the system is to have any chance of successful operation. They must be lightweight, operate with minimum radiation losses, cause minimum disturbance of the air flow, and be able to withstand the expected environmental conditions. The types of collector now being considered appear to have the potential for accomplishing these objectives.

#### 13.1 General Characteristics of Solar Energy Collectors

An irradiated surface tends to become heated when its optical absorption is high, but, upon being heated, will tend to cool because of thermal reradiation. The spectral distribution of the absorbed and the re-emitted radiation depends on the temperature and optical absorptivity of the source of each. Thus, according to Planck's Law, a surface at temperature,  $T$ , emits energy with intensity

$$I(\lambda) = \epsilon(\lambda) C_1 \lambda^{-5} (e^{C_2/\lambda T} - 1)^{-1} \frac{\text{watts}}{\text{cm}^2} \quad (256)$$

of radiation at wavelength  $\lambda$ , where  $C_1$  and  $C_2$  are constants. The proportion of incident energy at wavelength  $\lambda$  which a surface absorbs and converts into

---

<sup>1</sup> The analyses presented in Section 4 form a self-contained unit and do not necessarily conform with the nomenclature given in the front of this report. The symbols used in this section are explained as they are introduced.

heat is given by its absorptivity,  $\alpha(\lambda)$ . The only other physical principle needed to formulate the problem is Kirchhoff's Law, which states that for any surface whatsoever, the absorptivity equals the emissivity at a given wavelength.

$$\alpha(\lambda) = \epsilon(\lambda) \quad (257)$$

Therefore, the first problem is to state the optimum absorptivity function,  $\alpha(\lambda)$ .

Any practical solar absorber not involving direct concentration of the sun's rays will attain a maximum temperature only a fraction that of the sun. The spectral energy distribution of the absorbed radiation will be largely distinct from that of the reemitted radiation since the solar spectrum is approximately that of a black body at 5500°C, with a peak at about  $\lambda = 0.5$  microns, while the peak reradiation from the absorber occurs at a wavelength of a few microns. If these two spectra did not overlap at all, then the optimum  $\alpha(\lambda)$  would obviously be

$$\begin{aligned} \alpha(\lambda) &= 1 \text{ in the solar region, and} \\ \alpha(\lambda) &= 0 \text{ in the reradiation region;} \end{aligned}$$

so that all of the incident energy would be absorbed and none reemitted. As it happens, there is some overlap as shown in Fig. 28a. In order to retain the maximum energy, an absorber with a "cutoff" characteristic like that shown in Fig. 28a is desirable.

The problem is now to find the best value for the cutoff wavelength,  $\lambda_c$ , which depends in turn on the resulting absorber temperature,  $T$ . If the "trapping efficiency",  $f$ , is defined as the ratio between the incident energy converted into heat and the total incident energy (in the equilibrium situation) then,

$$f = (f_1)(f_2) \quad (258)$$

where

$$f_1 = \frac{\int_0^{\lambda_c} I_S(\lambda) d\lambda}{\int_0^{\infty} I_S(\lambda) d\lambda} \quad (259)$$

is the fraction of solar radiation absorbed, and

$$f_2 = \frac{\int_{\lambda_c}^{\infty} I_T(\lambda) d\lambda}{\int_0^{\infty} I_T(\lambda) d\lambda} \quad (260)$$

is the fraction of black body reradiation which is not allowed to escape.

$I_S(\lambda)$  is the energy density in the solar spectrum and  $I_T(\lambda)$  is that in the reradiation spectrum. A plot of trapping efficiency vs. temperature is given in Fig. 29. The optimum value of  $\lambda_c$  is then found by selecting the desired temperature curve and noting its maximal point. For the temperature range shown here,  $\lambda_c$  should thus be about 2.5 microns.

No actual absorber can attain the characteristics shown in Fig. 28a. A more realistic, although still somewhat idealized, collector characteristic curve is shown in Fig. 28b. The trapping efficiency,  $f$ , is defined as before:

$$f = (f_1)(f_2)$$

However,  $f_1$  and  $f_2$  are now:

$$f_1 = \frac{\int_0^{\lambda_c} \alpha I_S(\lambda) d\lambda + \int_{\lambda_c}^{\infty} \alpha^* I_S(\lambda) d\lambda}{\int_0^{\infty} I_S(\lambda) d\lambda} \quad (261)$$

$$f_2 = \frac{\int_0^{\lambda_c} (1 - \epsilon) I_T(\lambda) d\lambda + \int_{\lambda_c}^{\infty} (1 - \epsilon') I_T(\lambda) d\lambda}{\int_0^{\infty} I_T(\lambda) d\lambda} \quad (262)$$

The quantities  $\alpha$ ,  $\alpha'$ ,  $\epsilon$  and  $\epsilon'$  are defined in Figure 28b. The optimum value of  $\lambda_c$  is found as before for any particular values of  $\alpha(\lambda)$  and  $\epsilon(\lambda)$ . Although no actual collector would have the precise "high-pass" characteristic illustrated in Fig. 28b, this serves to demonstrate the type of filter behavior desired for solar energy collection purposes. An absorber becomes more nearly ideal as

$$\alpha, \epsilon \rightarrow 1.0 \text{ for } \lambda < \lambda_c \text{ and } \alpha', \epsilon' \rightarrow 0 \text{ for } \lambda > \lambda_c$$

For a real surface with  $\alpha$  and  $\epsilon$  continuously varying functions of  $\lambda$ , it is necessary to integrate the products  $\alpha(\lambda)I_S(\lambda)$  and  $[1 - \epsilon(\lambda)] I_T(\lambda)$  over the entire wavelength range.

There are many types of surfaces which exhibit the absorption-emission characteristics illustrated in Fig. 28. Among these are:

1. Metallic smoke deposits
2. Chemically produced surface coatings on reflecting metal subsurfaces
3. Interference filters

Many examples of Types 1 and 2 have been produced in the Electro-Optical Systems laboratories during the present program. Methods of producing these surfaces, as well as performance results, are discussed in the succeeding sections.

Although some have very promising characteristics, the severe requirements of the present application may make it necessary to augment their performance by making use of the fact that the incident solar radiation is very nearly parallel, while the reradiation from the absorbing surfaces is diffuse. Since the incident radiation is essentially parallel, it can be focussed through a small aperture before being absorbed by a collecting

surface. The diffuse reradiation then "sees" only a small area from which to escape. Devices which operate in the above manner are termed geometric radiation traps. Examples of these have been built and tested at Electro-Optical Systems. In order to gain the maximum performance, the geometric trap is used in conjunction with a spectrally selective absorbing surface. Many different configurations are possible using the basic focussing principle to reduce reradiation.

Absorbing surfaces using the interference principle may have very good absorbing-emitting characteristics when used alone with normal incidence light. However, it is believed by the Electro-Optical Systems' staff that their usefulness in conjunction with a geometric radiation trap would be limited. Therefore, the emphasis during the present program has been based on other types of spectrally selective absorbing surfaces. The general operating characteristics of the various types of absorbing surfaces and geometric traps are discussed in the following sections.

### 13.2 Spectrally Selective Surfaces

Solar energy research in recent years has resulted in several types of surface coatings with the absorptivity versus wavelength characteristics discussed in Section 13.1. These characteristics include high absorptivity in the visible, low emissivity in the infrared, and a suitable cutoff wavelength which maximizes total energy absorption.

Aside from optical interference filters (discussed in Section 13.4) these surfaces are prepared by metallic or non-metallic smoking processes and chemical or electrochemical deposition processes.

When embarking on an experimental program in spectral selectivity, it was Electro-Optical Systems' aim to duplicate and verify the results of other workers in the field as well as to develop new coatings which would show improved characteristics. Both these aims have been accomplished on the present program. This section includes a detailed discussion of the methods of preparation, general physical characteristics, and performance of the coatings prepared in the EOS laboratory.



Several types of surfaces with suitable cutoff wavelengths have been investigated. One or more processes in each of the following areas have been tried and tested:

1. Gold smoke surfaces
2. Oxidized sprayed coatings.
3. Electrochemically deposited coatings
4. Metal oxide coatings obtained by oxidizing the substrate metal
5. Non-metallic smoked coatings
6. Metal oxide coatings on glass (NESA glass)
7. Chemically plated coatings

These types of coatings or surfaces are described in greater detail below. The surfaces are evaluated on the basis of reflectance and transmittance measurements using a 13U Perkin-Elmer spectrophotometer. All samples were evaluated from below 0.3 to above 14 microns.

Figure 31 summarizes the results obtained in the visible and infrared for the best black surfaces. Low reflectance in the visible (high absorptance or transmittance) and high reflectance in the infrared (low emittance or transmittance) are the spectral characteristics desired. An inflection point between 1.5 - 3.5 microns is optimum (see Fig. 31). Figures 32 and 33 summarize the reflectance and transmittance versus wavelength data for the best metal-oxide coated glass.

The reflectance measurements are specular reflection only (total reflection equals specular plus diffuse) from an incidence angle  $10^{\circ}$  off the normal. It is not anticipated that the wavelength dependence of reflection is a strong function of the type of reflection (specular normal instead of a total hemispherical reflection). However, since percent specular reflection is a function of surface roughness and angle of incidence, it would be desirable to obtain total hemispherical reflection data. However, the equilibrium temperature tests described in Section 13.3 serve as an over-all evaluation of total hemispherical reflection. The reflection

data obtained from the spectrophotometer, therefore, serve as adequate first approximations to the nature of the surface.

It should be emphasized that the spectral properties of many of the surfaces are strongly dependent on coating thickness. The commercial processes investigated were generally prepared in accordance with manufacturer's directions. The experimental controls were then varied to produce surfaces with optimum spectral characteristics. During this work many surfaces were improved by thinning the surface film.

#### 13.2.1 Theoretical Discussion

Several years ago it was pointed out by Tabor (Ref. 12) that the efficiency of the collecting surfaces used as solar heating devices could be increased if they were coated with a material which absorbs in the range of the solar spectrum, but is transparent at long wavelengths, corresponding to the temperature to which the collector is heated by the sun. If this coating were backed by a metallic reflector of low absorptivity (and emissivity) in the infrared, then incoming solar radiation would be absorbed by the coating and the absorbed energy transferred to the metallic substrate by thermal conduction in the solid state. Due to the poor emissivity of the metal surface, very little of this energy is reradiated from the metal at the temperature (usually a few hundred degrees) to which the surface is raised. Thus radiation losses from the collector surfaces would be almost eliminated, metal emissivities being only 3 - 4 percent.

The surfaces used by Tabor and subsequent workers in this field were black metallic oxides, usually deposited on aluminum backing. Copper oxide ( $\text{CuO}$ ) has been investigated rather thoroughly by Unger in his M.I.T. thesis (Ref. 13) and further investigations have been carried out at EOS under the present contract.

The work done so far has been limited to the development of satisfactory chemical methods for depositing oxides or other compounds on the metallic surfaces, and the measurements of reflectivities and absorptivities of the surfaces in the visible and near infrared ranges. However, Unger has mentioned the fact that optical absorption in

semiconductor materials is due to an excitation of electrons from the valence band into the conduction band, across the energy gap existing in the semiconductor. The absorption edge is given by radiation whose photon energy is equal to the minimum energy gap between valence and conduction bands. If surface scattering effects are ignored, then radiation of energy above the "gap value" will interact with electrons excited into the conduction band and absorption will occur as a result of transitions in this band.

Photons of energy less than the 'energy gap' will not excite electrons into the conduction band and the material will be transparent to them. Since  $E = h\nu$ , the low energy photons correspond to low frequency (long wavelength) radiation. This is the qualitative explanation, in terms of solid state properties, of the spectrally selective behavior of certain surfaces. This simple method is complicated by two factors--first, the effects of impurities in the semiconducting surface; secondly, the scattering action of geometrical irregularities in the surface.

In terms of the band theory of semiconductors, the first feature was treated by the transistor developers, Bardeen, Shockley and associates (Ref. 14). Atoms of a material with a valence one greater or one less than that of the pure semiconductor are added to it, producing a surplus or deficit of electrons, respectively, in the lattice structure. In terms of the band theory, the impurities introduce electrons whose energy levels lie in the gap between valence and conduction bands. Under the influence of absorbed photons of appropriate energy, electrons may be excited from these 'impurity' levels into the conduction band or from the valence band to an impurity level, leaving a 'hole' in the valence band which migrates as a current carrier in the same way as an electron in the conduction band.

Clearly, the presence of these impurity levels in the energy gap can greatly modify the absorption characteristics of a semiconductor, since the effective width of the energy gap is changed (generally reduced). Such an effect appears to occur in the ARL supported experiments on CdS as a photovoltaic cell material. However, no systematic investigation of

the effects of such impurities on absorption properties of semiconductors and the relation of these properties to their usefulness as solar collectors, has yet been carried out.

The second complicating factor, mentioned above, is the light scattering effect due to small surface irregularities. It is convenient to summarize the relevant work on this topic. The problem of the scattering of electromagnetic waves by a sphere of arbitrary size and dielectric constant was solved in 1908 by Mie (Ref. 15), using the standard methods of electromagnetic field theory. His results give intensity of scattered light in terms of initial intensity, as a cumbersome and slowly convergent series expression. However, numerical values of this have been computed over a wide range of parameters and some of the results are summarized in van de Hulst's book (ref. 16).

It is found that, as a result of interference during the scattering process, a certain percentage of light is extinguished. Final numerical results appear as graphs of the extinction percentage,  $Q$ , against a parameter  $x$  of value  $\frac{2\pi r}{\lambda}$ , where  $r$  is the radius of the scattering sphere, and  $\lambda$  is the wavelength of the incident light.

Graphs of  $Q$  against  $x$  have been made for both dielectric and conducting spheres. They indicate rather sharp peaks in the extinction coefficient at a certain value of  $x$ . This critical value differs considerably for conducting and non-conducting spheres, being considerably smaller in the case of the former. In all cases, the extinction coefficient becomes zero rapidly as  $x$  goes to zero. Beyond the critical values of  $x$ , the extinction curve drops somewhat and flattens out. The results of these scattering calculations may be applied to a rough surface by setting up an idealized model of this surface, consisting of a perfectly flat backing dotted with spheres forming a partially opaque optical layer immediately in front of the backing. On an actual surface, the various irregularities will not be spherical, nor will they necessarily be independent of their neighbors, so far as scattering effects go. Hence the discussion here can only be considered a zero-order approximation.

This result follows. When the ratio  $r/\lambda$  is in the range 0.1 to 1.0, the extinction coefficient is at a maximum. When  $r/\lambda$  is less than this, a rather sharp cutoff in extinction should be noted (in the longer wavelengths for constant  $r$ ). When  $r/\lambda$  becomes greater than this, one can expect a moderate increase in transmission of light. It may be noted that the optical properties of the colloidal gold deposit studied by Harris (Ref. 17) (and currently at EOS) are in agreement with this statement. For the limit where  $\lambda \ll r$  one gets scattering from particles in accordance with ordinary rules of geometrical optics. By multiple reflection from its surface irregularities, the normal absorptivity of the medium is increased. This seems to explain the effect of surface roughening in increasing absorptivities (and hence emissivities) of surfaces.

It is probable that the radiation reflectivity of certain white oxides and ceramic materials is due to scattering effects. As  $x$  decreases beyond the critical value (or as  $\lambda$  increases), one would get an increase in the extinction coefficient near a resonant peak and for certain values of the refractive index, this peak can be broad enough to cover a considerable wavelength region. As far as is known, no systematic investigation of the relation between surface reflectivities as various wavelengths and the size of the diffracting obstacles, namely the irregularities in the surface, has been undertaken. Such an investigation, together with a quantitative theoretical discussion, would be needed to settle the problem.

Finally, it may be pointed out that the work of Tabor and others on spectrally selective semiconductor surfaces has, to date, been carried out at low surface emission temperatures, which are appropriate for extended solar collector surfaces under atmospheric conditions. However, for solar power sources under space conditions, a considerably higher concentration of solar energy is necessary, and thus temperatures in the range  $2000^{\circ}$  to  $3000^{\circ}\text{F}$  will be encountered. The problem of developing suitable spectrally selective coatings for use under these conditions does not seem to have received much attention as yet. The only high temperature semiconductor whose optical properties have been investigated is silicon

carbide. Data on high temperature oxides and pyrites-type compounds are not presently available.

Under high temperature conditions, moreover, a significant portion of absorbed energy may go into activating the thermionic emission of electrons. How far the thermionic emission characteristics may be affected by the photoactivated transfer of electrons from valence to conduction bands, and the effect of impurities in this process, is not known. The mechanism of conversion of radiation energy to energy of thermionically emitted electrons requires investigation as this process is part of the mechanism involved in optical absorption by semiconductors.

Summarizing, this discussion has outlined two distinct spectral selectivity effects. One is due to scattering by surface irregularities. the other, and more interesting, to the peculiar electronic structure of semiconductors. The most promising line of further work seems to lie in a study of this latter effect at higher temperatures, together with the closely related thermionic emission properties of an absorbing semiconductor.

### 13.2.2 Description and Preparation of Surfaces

Various references in the literature (Refs. 13 and 18 through 26) have been investigated with the intention of duplicating the state-of-the-art and, if possible, of making improvements in spectrally selective surfaces. These include black or near black coatings on aluminum, copper, magnesium, steel, platinum, nickel, and glass; as well as electrically conductive coatings on glass.

This section describes the physical properties and methods of preparation of these surfaces. Following sections discuss their spectral properties and suitability for use in solar energy collectors.

#### 13.2.2.1 Gold Smoke on Glass

The gold smoke filter derives its spectral properties from the mechanical structure of its surface which is composed of many microscopic gold droplets. Differential scattering of short and long wave radiation gives the characteristic of high absorptance of solar

radiation but low emittance of infrared. The properties and spectral characteristics of gold smokes are described in Refs. 17, 18, and 19.

Experimental work has been undertaken at Electro-Optical Systems which is aimed at producing improved forms of the gold smoke filter. The gold smoke surfaces produced during this program have been deposited on a glass substrate in order to facilitate fabrication. However, if they were to be used in a collector they would be put on an aluminum or aluminized glass base in order to take advantage of the low metallic emissivity in the infrared. Gold smoke filters are prepared in the following manner.

Gold wire was fused to a molybdenum boat in vacuum deposition system at a pressure of 5 microns and at white heat in each case. A 2" x 2" glass sheet, which in some cases was preheated in an air oven, was then placed at 3" or 3 1/2" above the boat, and the system evacuated until an air pressure of between 80 and 95 microns was measured. Pure dry nitrogen gas was then admitted through a needle valve until a total pressure of 2 mm of Hg was measured. The boat was then electrically heated by specific currents for varying amounts of time. The system was then shut down, the glass sheet removed and its transmittance measured in the range from 0.4 $\mu$  to about 4.0 $\mu$ . Among the 25 samples thus prepared, five promising gold smoke deposits were found. A tabulation of the variables for these five samples is shown below, while their transmission spectra are reproduced in Fig. 34.

Sample Number	Air Pressure (microns)	Boat to Glass Distance	Filament Setting (arbitrary units)	Deposition Time	Glass Temp. (Preheating)
5	90	3"	15	40 sec	20°C
6	85	3"	15	40 sec	20°C
19	85	3 1/2"	15	120 sec	20°C
20	85	3 1/2"	15	until light gray	120°C
23	85	3 1/2"	15	until dark gray	120°C

One of the foremost problems in investigating gold smoke deposits is that of reproducibility. Several samples were prepared under apparently identical conditions, but showed widely differing spectral characteristics. More conclusive results will probably be obtained by the use of boats of smaller size and greater depth so that during the fusing stage of the process the gold will adhere to the boat in a more uniform and reproducible pattern.

One aspect of this work has been particularly promising, namely the temperature stability of the deposits. They have maintained their spectral characteristics and physical integrity at a temperature of  $140^{\circ}\text{C}$ , whereas previous deposits prepared by other workers were found to disintegrate at  $120^{\circ}\text{C}$ .

#### 13.2.2.2 Sprayed Cupric Oxide on Aluminum

These surfaces, first prepared by Unger (Ref. 13), are cupric oxide coatings formed by spraying cupric nitrate solution onto heated samples of reflective aluminum.

Figure 31 indicates that Unger surfaces are among the best spectrally selective surfaces which Electro-Optical Systems has found.

The optimization of high solar absorptivity and low infrared emissivity can be closely controlled.

Figure 35 from Unger's thesis indicates the range in the nature of surfaces which can be made, expressed in integrated solar absorptivities ( $\alpha$ ) and integrated  $80^{\circ}\text{C}$  black-body emissivities, ( $\epsilon$ ). Additional analysis is required to determine the optimum obtainable  $\alpha + \epsilon$  for any particular requirement, since  $\epsilon$  increases as  $\alpha$  increases.

The Unger surface is a cupric oxide on aluminum coating. It is strongly adherent, stable at high temperatures, and can be prepared under very reproducible conditions. A cupric nitrate solution is sprayed onto a heated aluminum surface. The surface is then baked, converting the cupric nitrate to cupric oxide.



The spray head is a 125 M round spray head from the Spray Engineering Company, 100 Cambridge Street, Burlington, Massachusetts. The fluid nozzle is designated F2 and the air nozzle F2081. The nozzles are integral parts of the spray head. The aluminum is 99.99 percent pure (0 or 1/2 hard temper) obtained from the Alcoa Research Laboratories in New Kensington, Pa. Unger found that this high purity aluminum was necessary in order to insure proper surface reflectivity of the aluminum base. The aluminum was used as received, requiring no surface treatment. However, the four-inch squares which were used in the heat equilibrium tests had to be drilled, and in the process they picked up oil which was cleaned off by successive dips in xylene, redistilled acetone, and ethyl alcohol.

A compressor (with a filter to remove oil from the airstream) provides the airflow at 5 - 20 psig. The aluminum sample is fastened to a hot plate (a thermocouple is also fastened to the hot plate just at the edge of the aluminum sample). The aluminum is placed in a vertical position for horizontal spraying 22 cm from the nozzle head. The solution is fed to the nozzle from a constant head flask placed 30 cm above the level of the nozzle.

Eight variables affect the low temperature emission of the Unger surface (absorptivity for sunlight is relatively insensitive to the variables). The following results were obtained by Unger and were generally verified by this laboratory.

1. Concentration of Cupric Nitrate in the Spray

0.0025 molal cupric nitrate is a near optimum concentration to give the proper particle size of deposit; 0.005 molal is acceptable.

2. Spray Particle Droplet Size

The emissivity increases as the droplets decrease in size from 60 to 12 microns. This variable is controlled by the spray rate

discussed below.

3. Spraying Rate

The optimum spray rate is about 150 cc/hour; the acceptable limits being 50 - 250 cc/hour. At this rate the droplet size and spray rate effect on the drying of the film are optimum. This rate is obtained by the screw adjustment of the fluid nozzle.

4. Drying Plate Temperature

The hot plate can be kept at any temperature high enough to prevent visible wetting of the aluminum surface. Temperatures should not exceed 170°C, since the nitrate converts to the oxide above this temperature. The range studied was from 80° to 170°C.

5. Baking Temperature

Minimum emissivity and maximum solar absorptivity are obtained by baking at 350°C. At 230°C on one extreme, and 450°C on the other, definite detrimental factors set in.

6. Time of Baking

Samples baked for at least twelve hours had lower emissivities than samples baked for shorter times. No effect on optical properties of the surface was evidenced by varying the rate of heating or cooling.

7. Interval Between Completion of Spraying and Baking

The adhesion of the coating to the aluminum is good, but the cohesion of the cupric oxide film to itself is adversely affected by a lapse in time before baking. If baked immediately after spraying the cupric oxide

film will resist strong vibrations and air currents. If alternately baked and sprayed, the coating will resist vigorous massage.

8. Amount of Deposit Per Unit Area

The optimum range is 0.275 to 0.350 mg/cm<sup>2</sup> of CuO. For an optimum spray rate, this indicates a spraying time of about one hour. This calculation is based on the fact that 150 cc/hr. spray rate gives 1.5 cc/cm<sup>2</sup>hr.

The spray covered about a square inch of surface uniformly. In order to cover 4" x 4" aluminum squares with an Unger coating the hot plate was set on a track and slowly pulled in one direction. Whereas, the spray was attached to a cam shaft operated off a heart-shaped cam which provided a constant velocity (except at the ends of the stroke) reciprocating motion. A picture of this experimental apparatus is given in Fig. 30.

13.2.2.3 Cupric Oxide on Copper by the Ebonol Process  
(Ref. 20)

A deep black surface with a velvet-like appearance can be obtained on copper by this process. The procedure for obtaining this surface is:

1. Preparation of copper base (copper used is 99+ percent pure):
  - a. Scrub with Dutch cleanser to remove grease.
  - b. Etch in 10 N. nitric acid to uniformly activate the surface.
  - c. Pickle in 10 percent sulfuric acid.
2. Preparation of Ebonol bath:
  - a. 90.0 grams of Ebonol "C" Special are dissolved in 500 ml. water.
  - b. The bath is heated to 99 - 102°C.

3. Preparation of surface:

- a. The copper is immersed in the Ebonol bath for 8 - 10 minutes.
- b. The black surface is then rinsed in warm water.
- c. The surface is air-dried.

This patented product, Ebonol, was given a cursory analysis and determined to be an alkaline hypochlorite.

The deep black of this surface is damaged by touching it, as the fine protrusions of cupric oxide are collapsed under the slightest force.

13.2.2.4 Black Chromate on Magnesium (Ref. 21)

A dark brown coating can be obtained on magnesium by this process. The preparation procedure is:

1. Preparation of magnesium base:

- a. Scrub with Dutch cleanser to remove grease.
- b. Pickel in 60 percent hydrofluoric acid at 21-32°C.

2. Preparation of chromate bath:

- a. A bath of the following composition is prepared:

Ammonium sulfate, $(\text{NH}_4)_2\text{SO}_4$	30.0 g/l
Sodium dichromate, $\text{Na}_2\text{Cr}_2\text{O}_7 \cdot 2\text{H}_2\text{O}$	30.0 g/l
Ammonium hydroxide, $\text{NH}_4\text{OH}$	2.6 ml/l
(Sp. gr. 0.880)	

- b. The pH of the bath is 5.6-6.8.
- c. The bath is maintained at 99 - 100°C.

3. Preparation of surface:

- a. The magnesium is immersed in the chromate bath bath for 30 - 40 minutes.
- b. The coated surface is rinsed several times in warm water.
- c. The surface is air- or over-dried at 93°C for 5 to 15 minutes.

A chocolate brown surface was the darkest surface which could be obtained on pure magnesium by this process. Any attempt to produce a darker surface only resulted in a powdery non-adherent coating.

13.2.2.5 Black Nickel-Iron Oxide on Steel, by the "Nickel Pentrate" Process (Ref. 22)

A blue gray-black adherent surface can be obtained on steel by this process. The procedure for obtaining this surface is as follows:

1. Preparation of steel base (magnetic steel):
  - a. Scrub with Dutch cleanser to remove grease.
  - b. Etch in 10 - 20 percent sulfuric acid.
2. Preparation of Nickel Pentrate bath:
  - a. 180 g. of Nickel Pentrate are dissolved in 250 ml. water.
  - b. The bath is maintained at 126°C. (The solution boils at 126°C although the recommended temperature at which to maintain the bath is 143.3°C. This discrepancy evidently arises from the fact that the boiling point is dependent upon the salt concentration).
3. Preparation of surface:
  - a. The steel is immersed in the Pentrate bath for 15 minutes.
  - b. The surface is rinsed.
  - c. The surface is air-dried.

In the chemical process of oxidation, the nickel becomes an integral part of the black oxide surface imparted to the steel. Spectrographic analysis and microscopic examination show the presence of the nickel contained in the black oxide finish. The appearance of this surface is similar to that of the blueing given to steel guns.

13.2.2.6 Black Nickel on Copper or Aluminum (Ref. 23)  
Blue-black and brass-colored surfaces can be

formed on copper by this electrolytic deposition method. The preparation procedure is as follows:

1. Preparation of copper base:

a. Scrub with Dutch cleanser to remove grease.

2. Preparation of black nickel bath:

Nickel sulfate, $\text{NiSO}_4$	97.5 g/l
Sodium Thiocyanate, $\text{NaSCN}$	70.5 g/l
Zinc sulfate, $\text{ZnSO}_4$	45.0 g/l
Lead acetate, $\text{Pb}(\text{C}_2\text{H}_3\text{O}_2)_2$	11.25 g/l

3. Preparation of surface:

Operating conditions:

Temperature:	27°C-38°C
Voltage:	0.75-1.5 volts
Current density:	1 - 2 amps/ft <sup>2</sup>
Anodes:	nickel or carbon
Agitation:	cathode, when necessary

A gray-black surface can be obtained on aluminum

by this method. The procedure for obtaining the surface is the same as that for black nickel on copper. In order to increase the current density, which is very low because of the thin oxide film which makes the aluminum cathode passive, the aluminum is given a zincate dip which deposits a thin, uniform coat of zinc on the aluminum. The current density, by this means, was raised to one-half the recommended current density.

13.2.2.7 Black Nickel on Nickel and Nickel-Plated Copper

Actual tests were conducted which proved that black nickel deposits on copper surfaces do not suffer any loss in optical properties when heated to 170°C in a 300 micron vacuum test chamber. However, the black nickel on nickel system has been studied in case a system with exceptionally high resistance to thermal deterioration would be required. The procedure for obtaining the black nickel on nickel surface is as follows:

1. Preparation of nickel base:

- a. 99+ percent pure nickel is polished to a near mirror-bright finish.
- b. Scrub with Dutch cleanser to remove grease.  
(See 13.2.2.6)

2. Preparation of surface;

(See 13.2.2.6)

Black nickel was deposited both on nickel and nickel-plated copper in order to determine if there were any differences in emissivity characteristics between the plate nickel and the electrolytically deposited nickel. Also it would be useful to determine whether black nickel on nickel would be more resistant to oxidation than black nickel on nickel-plated copper, since it is well known that electrolytically deposited nickel is quite porous unless special techniques of intermittent plating and buffing are employed. The procedure for obtaining black nickel on a nickel-plated copper surface is as follows:

1. Preparation of nickel-plated copper:

- a. 99+ percent pure copper is polished to a mirror-bright surface.
- b. The copper is given a flash coat of nickel in a Watts'-type nickel plating bath.

2. Preparation of black-nickel bath:

(See 13.2.2.6)

3. Preparation of surface:

(See 13.2.2.6)

13.2.2.8 Cupric Oxide on Copper by the "Dura-Black" Process (Ref. 24)

A coating similar in appearance to that produced by the Ebonol procedure can be obtained by this process, which is one of single immersion in an alkaline, organic solution. This surface does

not have the same depth of black, however, the minute protrusions of copper oxide are the same, as is the ease with which they can be damaged. The basic black coating, nevertheless, is extremely hard and adherent and will withstand bending, twisting, and forming. The procedure for obtaining this surface is as follows:

1. Preparation of copper base:
  - a. Scrub with Dutch cleanser to remove grease.
  - b. Bright dip.
2. Preparation of Dura-Black bath:
  - a. 90.0 g. of Dura-Black are dissolved in 1000 ml. water.
  - b. The black surface is then rinsed in warm water.
3. Preparation of surface:
  - a. The copper is immersed in the Dura-Black bath for 4 - 5 minutes.
  - b. The black surface is then rinsed in warm water.

#### 13.2.2.9 Platinum Black on Platinum and Nickel (Ref. 25)

A velvet-like black coating can be obtained on platinum by standard methods of electrolytic deposition. The procedure for obtaining this surface is as follows:

1. Preparation of platinum base:
  - a. Scrub with Dutch cleanser to remove grease.
  - b. Dip in aqua regia.
  - c. Rinse well.
2. Preparation of platinizing solution:
  - a. The solution is composed of 3.0 percent chloro-platinic acid and 0.2 percent lead acetate.
3. Preparation of surface:

Operating conditions:

Temperature	Room temperature
Voltage	4.0 volts
Anodes	Carbon or platinum
Agitation	Cathode, when necessary



The procedure which is generally recommended is to reverse the voltage every minute until a thick coating is obtained; however, if a power supply with an AC ripple is used the process of reversal is unnecessary.

A velvet-like black coating of finely divided platinum may also be obtained by chemical immersion techniques, i.e., by using a metal more active than platinum to replace the platinum from solution. Black coatings were obtained on nickel in this manner.

#### 13.2.2.10 Carbon Black on Aluminum

A deep black, uniform coating can be obtained on aluminum by depositing carbon from the incomplete combustion of natural gas. This system is of interest because of its ease of application and the ease with which its reflectivity can be varied over wide limits. On smooth surfaces, its adhesion is not good, but the adhesion is much improved on a microscopically rough surface.

Carbon has been deposited on dull and bright platinum, copper, and aluminum. The most successful of the carbon black systems which our laboratory has investigated is the carbon black on aluminum. The procedure for obtaining this surface is as follows:

1. Preparation of aluminum base:

The aluminum sheet which was used was obtained from the Aluminum Company of America and is their Standard Bright Finish, Grade 1100, H-14. The aluminum sheet did not require any preliminary cleaning treatment.

2. Preparation of surfaces:

The aluminum sheet test sample (2" x 2") was held for about five minutes in the tip of an 8"- 9" luminous flame from a Fisher burner which had its air supply completely sealed off. Only enough carbon is deposited to give the surface a rust-colored cast when viewed orthogonal to the plate. The surface has a deep black cast when viewed nearly parallel to the plate.

The thickness of the aluminum oxide film which forms on the aluminum surface will be a function of the plate temperature, and monitoring the temperature of the plate with a thermocouple could serve as an additional experimental control. This system has not been fully evaluated because of difficulties in measuring the carbon film thickness.

#### 13.2.2.11 Electrically Conducting Metal Oxide Coatings on Glass (NESA Glass)

Many procedures exist in the literature for preparing these conductive glasses (Refs. 26 and 27), which generally exhibit low reflection in the visible and high reflection in the infrared. They could therefore act as plates used to retain incident solar radiation within a cavity. Corning Glass Works provides commercially an infrared reflecting glass which reflects, according to their literature, from 6 - 8 percent in the visible, 30 percent at 2.2 microns, and approaches 70 percent reflection as an asymptote at 5 microns. Samples have been received and evaluated in this laboratory.

The original EOS attempts at producing electrically conducting glass coatings were made by spraying a stannic chloride-isopropyl alcohol solution from an atomizer onto a heated glass surface. Both soft glass and fused quartz were used and an optimum temperature was found at 600 - 700°C. The minimum resistance for these coatings was 200 ohms per square. For optimum spectral characteristics the resistance should be about 5 - 20 ohms per square. In another method,  $\text{SnCl}_4 \cdot 5\text{H}_2\text{O}$  was put into a heated bulge in a long Vycor blowpipe. Over this was passed air saturated with water vapor while the blowpipe was held in a horizontal position. From the tip of the tube the vapor impinged upon the glass. Optimum conditions were found for the temperature of the  $\text{SnCl}_4 \cdot 5\text{H}_2\text{O}$ , the temperature of the glass, and for the air-water ratio, which was varied by changing the temperature of the water used in saturating the air. The lowest resistance obtained in either of these methods was 200 ohms per square.

The hydrolysis of stannic chloride is very slow at room temperature and occurs mostly on the hot surface of the glass.

However, there is a large amount of hydrolysis which occurs in the heated liquid  $\text{SnCl}_4 \cdot 5\text{H}_2\text{O}$  in the blow pipe. In order to prevent this, calcium chloride was mixed with the  $\text{SnCl}_4 \cdot 5\text{H}_2\text{O}$  as a drying agent. In this manner a superior coating with a resistance of 150 ohms per square was obtained. Pure anhydrous stannic chloride was also tried but was given up since a resistance of 410 ohms per square was the lowest obtainable for very short duration spray times.

Solution No. 2 from Patent No. 2,564,706 (Ref. 13) by John M. Mochel (assigned to the Corning Glass Works) was then tried. This proved very successful since it was possible, by this method, to get resistances from less than five to about twenty ohms per square. The solution contained 50 ml. of water, 10 ml. of hydrochloric acid, 100 gm. of stannic chloride pentahydrate ( $\text{SnCl}_4 \cdot 5\text{H}_2\text{O}$ ), and 0.5 gm. of antimony trichloride ( $\text{SbCl}_3$ ). It was put into a DeVilbiss No. 15 aspirator through which air was passed from a compressor. A pressure of about 45 cm. of mercury was found necessary to produce the proper drop size for a uniform coating. For these purposes the optimum temperature was found to be between 600 and 650°C for the surface of the glass. The glass plates were laid flat on the floor of a muffle furnace and sprayed for about one minute from a distance of about one foot, with the spray directed onto the surface at a slight angle.

The cleaning of the glass plates is an important factor. The stannic oxide coating of glass plates which were uncleaned had a resistance of 1500 ohms per square; whereas those cleaned with sulfuric acid-dichromate cleaning solution had a resistance of five to twenty ohms per square.

The relationship between surface resistance and spectral properties is discussed in Section 13.2.3.

### 13.2.3 Spectral Evaluation of Surfaces

Each selective surface sample produced in the EOS laboratory was tested in the Perkin-Elmer 13U spectrophotometer in order to determine reflectance or transmittance as a function of wavelength. This

instrument is described in Section 13.5.3.

The procedures used to record the reflectance of both the black coated surfaces and the NESA glass were essentially the same. These measurements are not absolute, but are based on the known reflectance characteristic of an aluminum mirror. Therefore, after standardizing the reflectance scale in terms of the aluminum characteristic, the aluminum was replaced by the actual samples and their reflectances determined over the same range.

Gold smoke transmittance curves were obtained directly in the double beam mode of operation of the spectrophotometer. This allows an absolute transmittance curve to be recorded directly on the chart. A study was conducted to determine what effect changing the direction through which the light was passed through the NESA glass had on the transmittance in the visible region of the spectrum. Figure 36 compares the transmittance measurements when the coated side was facing the light source and when the coated side is away from the light source. On the basis of this study it can be concluded that the transmission of NESA glass is unaffected by the direction through which light is passed.

One generalization which can tentatively be made for the opaque spectrally selective surfaces produced at Electro-Optical Systems is that the solar absorption and infrared emission both increase as the thickness of the coating increases and that for certain surfaces the inflection point shifts toward the longer wavelengths. The absorption and emission can thus be controlled to some extent, but not independently. Furthermore, the quantitative functional dependence of  $\alpha$  and  $\epsilon$  on coating thickness is not now known.

This section contains brief descriptions of the spectral characteristics of each surface produced. In some cases, conclusions are drawn regarding the reasons for the results obtained.

### 1. Gold Smoke on Glass

The results of the gold smoke investigations are given in Fig. 34. It is clear from these curves that widely varying spectral characteristics may result from small changes in deposition procedure. Samples with good visible absorption also tended to show relatively poorer infrared transmission.

The better samples developed during this program showed spectral characteristics generally in accordance with those obtained by other workers (Refs. 17,18, and 19). However, considerably improved coatings may be possible by means of techniques currently being investigated at EOS on other programs.

### 2. Sprayed Cupric Oxide on Aluminum

The results obtained from these surfaces (illustrated in Fig. 37) agreed well with those obtained by Unger (Ref. 13 and Fig. 38). The best of the Unger surfaces was used in the heat equilibrium tests. The surface was examined in two areas. The reflectance data for these two areas are compared in Fig. 37 and indicate the degree of uniformity of the surface. Inasmuch as Unger carried out a careful and thorough research program on these coatings, it is unlikely that they will be greatly improved in the future. However, because of the research already expended, they are among the best spectrally selective surfaces yet produced in regard to both their spectral and physical properties.

The only additional comment which our laboratory has to make regarding the fabrication of Unger surfaces is that, in general, the spray rate, the spray time, and the method of spraying must be adjusted so that the baked coat is no darker than a very light gray. Evidently the film must be thin enough to be transparent in the infrared and allow the low emissivity characteristics of the aluminum to be the controlling factor. A reflectance versus wavelength curve (Fig. 39) for uncoated 99.99 percent pure aluminum is included so that a comparison can be made between the coated and uncoated surfaces. Aluminum Sample No. 2 was used in the preparation of this Unger surface.

A great deal of effort was spent in the selection of the proper aluminum substrate. The following types of aluminum surfaces were investigated:

Sample No. 1	99.99 percent aluminum, 0.062" thick, 1/2-H
Sample No. 2	99.99 percent aluminum, 0.062" thick, 1/2-H
Sample No. 3	99.99 percent aluminum, 0.062" thick, 1/2-H
Sample No. 4	Reflector grade aluminum, 0.040" thick

Sample No. 1 and Sample No. 2 were from the same sheet of aluminum, only Sample No. 1 was taken from a portion of the sheet which appeared to have the least visible reflectivity. Sample No. 2 was taken from a portion of the sheet which appeared to have the greatest visible reflectivity. Sample No. 3 was buffed on a buffing wheel. Sample No. 4 is what the Aluminum Company of America calls their reflector grade aluminum. Figure 39 gives a comparison of the reflectance between these four samples. Sample No. 2 was chosen to be used in the preparation of the Unger surface. Another sample of aluminum sheet which was evaluated for use as an Unger substrate was 99.99 percent pure aluminum, 0.01 inch thick, 0-H temper. This aluminum has a uniformly bright surface to the eye. The 0.01 inch thick aluminum was not spectrally evaluated with the other samples because it was too thin to be used in the heat equilibrium test unit. The 99.99 percent aluminum, 0.062 inch thick, is 1/2-H temper and has a dull coating in places (probably a thick oxide film) which may have been introduced during the tempering process.

Aluminum Sample No. 2 was preferred to aluminum Sample No. 3 because it was felt that the compound used in buffing might not be entirely removed by the organic solvents and that this might introduce another experimental variable which would require control.

### 3. Cupric Oxide on Copper by the "Ebonol" Process

As shown in Fig. 40, this system has 0 percent reflectance from 0.3 - 6 microns and becomes reflecting in the range 6 - 9 microns. No conclusions can be made as to the difference in reflectance between Samples 0, 1, 2, and 3, all of which were prepared by the same procedure. The reflectance is less than 50 percent; therefore, without further investigation it does not appear promising for the present application. Further investigations should include forming a coat as thin as possible on a highly polished substrate.

Polished copper was spectrally evaluated, and found to be as reflective in the infrared as aluminum. Etched copper has a specular-reflectance much lower than that of polished copper; it may or may not have a lower diffuse reflectance.

Although it was desirable to prepare and evaluate thin cupric oxide coatings on polished copper, this was not done since the copper substrate had to be etched prior to oxidation and, therefore, the coated surface could not be evaluated by specular reflectance.

Cupric oxide coatings using Ebonol have been prepared and evaluated by other workers in this field (Ref. 28) Gier and Dunkle claim to have produced surfaces with five percent reflectance in the visible and 80 - 85 percent reflectance in the infrared. The inflection point, however, is at only one micron which would give a trapping efficiency of only 70 percent for an equilibrium temperature of 400°C.

4. Black Chromate on Magnesium

This coating was powdery and non-adherent so spectral measurements were not conducted.

5. Black Nickel-Iron Oxide on Steel by the "Nickel Pentrate" Process (see Fig. 41)

These surfaces had 0 percent reflectance from 0.3 - 2.25 microns. The surface begins to reflect at 2.25 microns. At 8.5 microns the reflectance is 17.5 percent. The spectral characteristics of this system are not satisfactory for this application, so no further work was done on this surface.

6. Black Nickel on Aluminum

These surfaces had 0 percent reflectance from 0.9 microns to 7.5 microns. The spectral characteristics of this system are also not satisfactory for our purpose so no further work was done on this system.

7. Black Nickel on Copper

As shown in Fig. 42, this surface is one of the most promising for the present application. It has less than 10 percent reflectance in the visible and is greater than 95 percent reflecting in the infrared with a very sharp cutoff between 1.0 and 2.5 microns. The best of the black nickel surfaces was used in the heat equilibrium tests. The surface was examined in

two areas, diagonally across the plate from each other. The reflectance data for these two areas are compared in Fig. 42 and indicate the degree of uniformity of the surface.

In the course of studying the black nickel coating there was noted a considerable difference in optical characteristics between samples. (See Fig. 43). Three variables in the procedure (time of coating, current density, and bath temperature) were controlled so as to determine their effect on the optical characteristics. Fourteen samples were prepared while the experimental variables were changed within the recommended limits:

Time of coating	1 - 3 minutes
Current density	1 - 2 amps/ft <sup>2</sup>
Bath temperature	27 - 38°C

It was observed that at lower temperatures (less than 36°C), and as the bath begins to become depleted, the coating received a definitely yellow cast. It was also determined that voltage control was extremely important, 1.5 volts being the optimum. Both current and voltage should be metered during the electrolytic process. Undetermined conditions, which cause the surface to appear blue-black, also seem to produce surfaces with improved spectral characteristics for this application. Further study is required in order to determine the exact nature of the conditions which produce variations in the spectral response of these surfaces.

#### 8. Black Nickel on Nickel and Nickel Plated Copper

This surface is also very promising as shown in Fig. 44. Toward the close of the experimental work, it was concluded that in the evaluation of the spectral characteristics of surfaces, it would be helpful to determine the reflectance of the uncoated plate before the plate receives surface treatment. The inflection point on the curve of reflectance versus wavelength for several of these black surfaces can be shifted toward the visible merely by polishing the substrate. A comparison of the results of the black nickel on nickel system and the black nickel on nickel-plated copper illustrates this point. See Fig. 44. The black nickel was deposited on nickel polished to a near mirror-bright finish and on nickel-plated copper, which was, prior to plating, polished to a mirror-bright finish. The effect



of the brighter base on the shift of the inflection point toward the visible is evidenced here.

9. Cupric Oxide on Copper by the "Dura-Black" Process

This surface also showed promise for solar energy collection. As illustrated in Fig. 31, the system is 0 percent reflecting in the visible, begins to reflect at 1 micron and becomes 100 percent reflecting in the infrared.

10. Platinum Black on Platinum

To our knowledge, platinum black coatings on platinum have never before been evaluated as potential spectrally selective surfaces. Fig. 45 shows the reflectance of platinum black on a platinum surface as a function of wavelength. This surface is mechanically unstable; however, it has the unique advantage of chemical inertness and thermal stability, which would be very useful in a system in which these qualities would be very important. This surface has probably the best spectral characteristics for the purpose of trapping solar energy of any of the surfaces prepared and investigated by our laboratory. Tests have been made which indicate that the platinum black film thickness controls, to some extent, the inflection point, the degree of slope, and the infrared emission. With Unger's surface, in order to gain low emissivity in the infrared, absorptivity in the visible has to be sacrificed. In the case of platinum black on platinum there is no need to sacrifice in the visible to gain in the infrared.

Platinum black has been electrochemically deposited on platinum-plated copper; however, the substrate metal was active and contaminated the bath thus ruining the coating. In the future there should be an investigation of platinum black on a thick electroplated platinum plate.

The mechanical stability of the platinum black coating may be increased by converting the platinum black to a more adherent platinum coating, namely platinum gray. This can be accomplished by heating the platinum black coated surface to a dull redness. This conversion may or may not alter the optical properties of this system. The adhesion of platinum black to platinum may also be increased by microscopically roughening the platinum substrate.

Platinum black has been chemically plated on nickel, aluminum, and copper. Whereas platinum black on platinum is not very adherent, platinum black on nickel and copper is very adherent. Platinum black on nickel has been spectrally evaluated and does not appear promising. However, the nickel substrate, which has not been spectrally evaluated, appears dull to the eye and this may account for the poor spectral results. Further effort in this phase of the work is advised. Platinum black on copper appears very promising. It is too early to judge the promise of platinum black on aluminum.

11. Carbon Black on Aluminum

To our knowledge, carbon black coatings on highly reflective metals have never before been evaluated as potential spectrally selective surfaces. Carbon black, though mechanically unstable, offers exceptional absorptance in the visible with a good control of emittance in the infrared. See Fig. 46. It has been established, as in the case of platinum black, that the film thickness, to some degree, controls the inflection point, the degree of slope, and the infrared emission. Although film thickness could not be quantitatively controlled, it could be qualitatively determined by visual observation and by noting the coating time. Surfaces with increasingly thick deposits had increasing absorption in the visible, a decrease in slope, an inflection point shift toward the infrared, and an increase in infrared emission. It is strongly felt that the spectral characteristics of this surface can be improved by depositing extremely thin carbon films.

12. Metal Oxide Coatings on Glass (NESA Glass)

The characteristic desired with metal oxide coated glass is high solar transmittance, and high infrared reflectance. Therefore, transmittance as well as reflectance is determined for the glass. For the purposes of this program, the optical properties of thin pyrex glass are satisfactory. The metal oxide conductive coatings have also been produced by Electro-Optical Systems on fused silica test pieces at 700°C with identical results. The advantage to be gained through the use of fused silica is a slightly higher transmittance for the same thickness of glass. Spectrally, the transmittance of both types of glass is flat from 0.3 to 2.3 microns.

The characteristics of six samples of NESA glass which were the best prepared at our laboratory and one prepared at Corning Glass Works are shown in Figs. 32, 33, 47, 48, and 49. In Fig. 47, it is seen that NESA Sample No. 29 approaches both in electrical resistance and reflectance very closely to that of Corning Glass. NESA Samples No. 27, 28, and 29 were prepared on 1/16" soft glass; NESA Samples P-1 and P-2 (Figs. 48 and 49) were prepared on 1/8" Pyrex glass, and NESA Sample No. P-6 (Figs. 32 and 33) was prepared on 1/16" Pyrex glass. NESA Sample No. P-6 was selected for use in the heat equilibrium tests. Aside from the difference in glass base, the chemical formulation of the solution used in spraying and the method of preparation is the same for each of the above NESA samples.

One generalization which can tentatively be made for the transparent spectrally selective surfaces produced at EOS is in regard to the relationship between surface resistance and spectral properties. Coatings prepared with stannic chloride hydrate and pure anhydrous stannic chloride had resistances ranging from 150 to 1,300,000 ohms per square; while coatings prepared with solution No. 2 from Patent No. 2,564,706 had resistances ranging from five to twenty ohms per square. The higher resistance coatings had spectral characteristics which were unsuitable for use in a solar heat trap, whereas, the lower resistance coatings have spectral characteristics which are very satisfactory for this purpose.

The presence of antimony trichloride is necessary to produce surfaces of low resistance. Chemical compounds other than antimony trichloride have been used to produce surfaces of low electrical resistance. Patent 2,694,649 (1954) indicates that an  $\text{In}_2\text{O}_3$  coating on glass can give as low a resistance as the  $\text{SnO}_2$ ,  $\text{Sb}_2\text{O}_3$  coatings prepared from the Corning patent. It would be interesting to compare the spectral properties.

Patent 2,756,165 (1956) describes a process in which transparent plastic is coated with a material having high transmission and low reflection in the visible. It would be interesting to determine if the reflectance in the infrared is high enough to be of interest.

In order to exactly determine the optimum resistance for metal oxide coatings, a comparison must be made between energy lost from low transmittance in the visible and energy gained from high reflectance in the infrared; i.e., both reflectance and transmittance must be optimized as functions of resistance.

The reflectance of the visible part of the spectrum seems to be connected in no simple fashion with the resistance of those coatings which have resistances in the range of five to twenty ohms per square. Figure 50 is a plot of reflectance versus wavelengths for NESA glasses with resistances ranging from 4.9 to 20.0 ohms per square.

The reflectance in the infrared, however, shows a definite correlation with the resistance of the coated surface. Figure 47 shows reflectance characteristics for NESA glasses with resistances from 6.6 to 20.0 ohms. The surfaces with electrical resistances of 6.6 and 11.0 ohms per square have almost 10 percent higher reflectance than do surfaces with resistances of 14.7 and 20.0 ohms per square. This correlation of electrical resistance and infrared reflection is also borne out by another set of stannic oxide glasses. P-1 and P-2 (see Fig. 48), which were prepared here in our laboratories. NESA Sample No. P-1 which has a resistance of 16.0 ohms per square has a 15 percent lower reflectance in the infrared than does NESA Sample No. P-2 with a resistance of only 3.7 ohms. Based on limited experimental data it can be concluded that the lower the electrical resistance the higher the reflectance in the infrared portion of the spectrum.

The transmittance in the visible part of the spectrum shows a correlation with electrical resistance of the surface coating, see Fig. 49. P-1 with a resistance of 16 ohms per square has a transmittance about 30 percent higher than P-2 with a resistance of 2.7 ohms per square.

In Fig. 36, a comparison is made between the transmittance of uncoated Pyrex glass and Pyrex glass coated with stannic oxide. The stannic oxide coating decreases the transmittance of the pyrex glass in the visible region of the solar spectrum. This loss may or may not be offset by the increased reflectance of the coated glass in the infrared region, where the black surface is emitting. This comparison of the effectiveness of NESA versus uncoated glass is left for future analytical and experimental study.

#### 13.2.4 Conclusions Regarding Suitability of Surfaces

The suitability of the various spectrally selective surfaces for solar energy collection depends on their spectral characteristics, uniformity, ease of fabrication, and cost. A comparison of properties for the best opaque spectrally selective surfaces prepared at Electro-Optical Systems is given in Table IV. The description of each property is based only on a qualitative comparison between the systems listed and not upon any absolute **standard**. The solar reflectivity gives the percent reflectance in the visible portion of the spectrum. The infrared emissivity gives the percent emittance from 7 - 15 microns.

Of the systems which have been evaluated, the best, based on over-all considerations, seem to be the black nickel on nickel or copper and the cupric oxide on aluminum by the Unger process.

### 13.3 Radiation Traps

A radiation trap may be defined as a device which exhibits a high absorptance for solar energy while displaying the characteristics of a poor emitter in the long wave length region. There are two basic schemes which may be used to realize the trapping effect; one differentiates between the wavelengths of radiation, while the other distinguishes between the wavefronts of incident and reradiated energy by geometric means. A surface having the former characteristic is termed spectrally selective.

The spectrally selective trap consists of a specially treated surface which absorbs solar radiation but is a poor emitter for the long wavelength thermal radiation. Several methods for obtaining such surfaces are described elsewhere. (See Section 13.2). As an example, chemical and electrolytic deposition of thin black coatings on polished aluminum plates yield such surfaces. Another approach is the treatment of cover glasses so that they will transmit solar radiation to a black absorber plate beneath but will reflect back the thermal radiation from absorber.

Wavefront discrimination is accomplished by geometric means. A familiar example of such a trap is the use of an insulated cavity receiver in conjunction with a concentrator (lens or mirror). The parallel solar radiation is focussed through a small hole in the cavity receiver and almost totally absorbed on the walls of the cavity. Only a very small amount of the diffuse radiation from the inside walls of the cavity can escape from the small hole.

The analytical and experimental results from the collector program, as well as the over-all system requirements, have indicated a heat collector-exchanger design which may satisfy the requirements of the solar propulsion system. This design (see Section 11.3) consists of a series of airfoil shaped struts placed parallel to the airflow in the heat exchanger. Incoming radiation is focussed into the strut through a hole in the top surface by means of a Fresnel lens. After passing through the hole the energy is scattered within the strut and absorbed on the inside surface. Energy losses in this system can only occur as reradiation from the surface of the hole, or from losses in the focussing system. These losses are discussed in the first subsection. The second subsection discusses the performance of traps made

and tested in the Electro-Optical Systems, Inc. laboratory.

### 13.3.1 Energy Losses from Geometric Radiation Traps

In evaluating the energy losses of geometric heat traps it is necessary to consider the transmission efficiency of the lens-entrance hole combination and the heat loss by radiation from the hole. These factors are clearly interdependent since enlarging the hole increases the transmission efficiency but also increases the heat loss from the hole. The following will refer specifically to the airfoil-shaped geometric radiation trap. However, most of the comments are generally applicable.

Suppose the strut has a total surface area,  $A_s$ , an emissivity  $\epsilon_s$ , and is at a uniform temperature,  $T$ . If the strut is radiating to an environment whose equivalent temperature is sufficiently low, the heat loss by radiation from the strut surface,  $Q_s$ , may be written:

$$Q_s = A_s \epsilon_s \sigma T^4 \quad (263)$$

If the strut entrance hole has a diameter  $d_h$  and is radiating like a black body at temperature  $T$ , the heat loss from the hole  $Q_h$  to a low temperature environment is given by:

$$Q_h = \frac{\pi d_h^2}{4} \sigma T^4 \quad (264)$$

The diameter of the entrance hole will probably be made several times larger than the image diameter of the sun in order to account for aberrations, lens defects and misalignments. Let  $\xi$  be this factor. If  $f$  is the focal length of the lens, then the hole diameter may be written approximately as:

$$d_h = \xi \frac{f}{100} \quad (265)$$

because the sun (and, thus, the image) subtends an angle of about 1/100 radian as seen from the lens. Substituting this into the last equation and taking the ratio  $Q_h/Q_s$  yields:

$$\frac{Q_h}{Q_s} = \frac{\xi^2 f^2 \pi}{4 \times 10^4 A_s \epsilon_s} \quad (266)$$

If the lens is circular with a diameter  $d_L$  and a projected area  $A_L$ , the above equation may be written

$$\frac{Q_h}{Q_s} = \frac{\xi^2}{10^4 \epsilon_s} \frac{A_L}{A_s} \left( \frac{f}{d_L} \right)^2 \quad (267)$$

Either of the last two equations may be evaluated in order to predict the importance of the heat losses through the entrance hole. If the design parameters are taken to be as follows:

$$\frac{f}{d_L} = \frac{1}{2}$$

$$\frac{A_L}{A_s} = \frac{1}{2} \quad (\text{equal projected area})$$

and an optimistic value of 0.02 is chosen for  $\epsilon_s$  (which tends to increase  $Q_h/Q_s$ ), then even for  $\xi = 10$ , the heat loss from the entrance hole is only 6 percent of the losses from the airfoil surface. The assumption made that the heat loss from the entrance hole is negligible appears to be justified.

In evaluating the transmission efficiency of the lens-entrance hole combination it is necessary to know the distribution of flux at the focus of the lens. Once this distribution is known, the blocking effect of small entrance holes may be evaluated. Clearly, if the entrance hole is made large enough, the transmission efficiency of the combination is simply that of the lens itself. Thin sheet plastic Fresnel lenses have been made which exhibit a transmission of 75 to 85 percent.

Depending upon the emissivity of the strut surface, entrance holes whose diameters are 10 to 20 times larger than the solar image may be used without introducing serious radiation losses. (Equations 266 and 267). Hence it is reasonable to assume transmission efficiencies of the lens-entrance hole combination of about 70 to 80 percent. The exact values will, of course, depend upon the final design of the lens including the mechanical perfection achieved.



In order to reduce the heat losses from entrance holes, it is often suggested that NESAs glass covers be used over the holes. Light passes through the NESAs glass and is absorbed by the "black" surface which reaches a temperature  $T$ . Part of the energy which is reradiated from the inside of the trap structure impinges upon, and is mostly reflected by, the NESAs glass. That component which is not reflected is absorbed and serves, along with the small amount of incoming light energy which is absorbed, to raise the temperature of the glass. The NESAs glass, in turn, radiates to both the inside of the trap and to the "sky". This upward loss of energy is less than that which would be lost through the hole itself since the NESAs glass is at a lower temperature than the strut. However, a new energy loss has been introduced; approximately 30 percent of the light energy striking the NESAs glass is reflected. (Various coatings can be used to reduce reflection losses slightly). Thus, it is only for very large holes, where the radiation losses would normally be somewhat more than 30 percent of the input energy, that using the NESAs glass in this manner pays off. The crossover point can be calculated as follows:

Since the area of the NESAs window is small compared with the radiating area of the inside of the trap, the net heat transfer to the window,  $Q_w$ , may be written:

$$Q_w = \frac{\pi d_w^2}{4} \epsilon_w \sigma [T^4 - T_w^4] \quad (268)$$

where  $d_w$  is the diameter of the window,  $\epsilon_w$  is its emissivity for long wavelength radiation,  $T_w$  is the window temperature and  $T$  is the mean trap temperature. At thermal equilibrium,  $Q_w$ , must be equal to the upward heat loss from the window (neglecting the small amount of light absorption) which is given approximately by:

$$Q_w = \frac{\pi d_w^2}{4} \sigma T_w^4 \quad (269)$$

Using these two relations:

$$T_w = \left( \frac{\epsilon_w}{1 + \epsilon_w} \right)^{1/4} T \quad (270)$$

Hence, the upward radiation loss is given by

$$Q_w = \frac{\pi d_w^2}{4} \sigma \left( \frac{\epsilon_w}{1 + \epsilon_w} \right) T^4 \quad (271)$$

which is much smaller than the heat loss,  $Q_h$ , for a simple hole (Eq. 264) since  $\epsilon_w$  is small.

The total upward energy loss is given by the sum of the last equation and the reflection loss,  $rQ_s$ , where  $r$  is the effective reflectance of the window and  $Q_s$  is the total energy input to the hole. The "breakeven" point occurs when

$$Q_w + rQ_s = Q_h \quad (272)$$

or where

$$d_h^2 = d_w^2 \left( \frac{\epsilon_w}{1 + \epsilon_w} \right) + \frac{4rQ_s}{\pi T^4} \quad (273)$$

### 13.3.2 Laboratory Test Traps

Two fundamental types of radiation traps have been assembled and tested during the current Electro-Optical Systems program. Examples of the wavelength or spectrally selective type of trap, as discussed in Section 13.3, are the cupric oxide on aluminum by the Unger process, the deposition of black nickel on copper, and the use of NESA glass with a blackened absorber. The multi-element Fresnel lens fabricated from 16 individual vinyl plastic lenses (Bolsey Research and Development Corporation) was used to build a geometric

type trap. These converging lenses focus the parallel rays of incident solar radiation through 16 small holes in an aluminized sheet which is placed midway between the multi-element lens and the black absorber. (The radiation is absorbed by the collector and is trapped since the aluminized sheet has a low emissivity and reflects collector radiation while the holes are so small the negligible flux passes upward through them.)

The various black surfaces produced during the present program were laid down on metal plates, four inches on a side. A test jig was designed and constructed to hold these black surfaces with either of the radiation trap envelopes previously described. When using either the NESA glass cover, or the multi-element Fresnel lens, end losses were minimized by the provision of highly reflecting side walls of vacuum deposited aluminum on glass. The radiation trap thus consisted of either a selective black surface by itself, or a black surface discriminating envelope, and the reflecting side walls. The trap enclosure is thermally insulated from the metal supporting frame with transite spacers. The frame, in turn, slides onto four rods, attached to a circular metal collar that fits into the window throat of the vacuum test chamber. The solar flux entering the test chamber window falls normally onto the surface of the trap. Equilibrium temperature measurements on the black surfaces were affected by attaching five iron constant thermocouples to the surfaces. The back surfaces of the plates have a low emissivity and provision is made so that they may be covered with a layer of insulation if desired. Convective losses are reduced to a minimum by evacuating the test chamber to a pressure of a few microns of mercury. The trap structure is shown in Fig. 51.

#### 13.3.2.1 Estimate of Thermal Equilibrium Conditions

At thermal equilibrium, the temperature of a radiation trap may be calculated by solving the following equation:

$$\alpha_s A_p q_s = P + K + A_p \epsilon \sigma T^4 - A_p \alpha_b \sigma T_b^4 \quad (274)$$

where  $\alpha_s$  is the absorptance for solar radiation,  $A_p$  is the area of one side of the plate,  $q_s$  is the solar heat input,  $P$  is the total power withdrawn,

$K$  represents any undesirable thermal conductivity heat loss,  $\epsilon$  is the emissivity (at temperature,  $T$ ) of the plate and  $\sigma$  is the Stefan-Boltzmann constant.  $\alpha_b$  is the absorptance of the plate for environmental radiation whose temperature is  $T_b$ . (Both  $\epsilon$  and  $\alpha_b$  may be interpreted as the sum of the contributions from the front and back surfaces when the plate is not insulated on the back side.)

The heat loss due to the thermal conductivity of the air may be calculated knowing the geometry of the experiment. It is, of course, a function of  $T$  as well as the environmental temperature  $T_b$ . Using this Eq. 274 it was possible to correlate the experimental work done in the solar test facility with calculations based upon the measured emissivity characteristics of several radiation traps. (The evaluation of equivalent absorptances and emissivities requires the solution of integrals involving Planck's function.)

In order to obtain some feeling for the temperatures and power levels involved, Eq. 274 will now be investigated under the conditions likely to be encountered in a configuration. The environmental temperatures,  $T_b$ , will be very much smaller than the absorber temperature  $T$ , and since  $\alpha_b = \epsilon$ , the last term in the above equation may be ignored compared with  $A_p \epsilon \sigma T^4$ . Losses due to thermal conductivity, e.g., through support structures, can be made sufficiently small so that  $K$  may be assumed to be zero. Thus, it is assumed that the absorbed flux is partly transferred as thermal energy to the stream and partly lost by reradiation, then

$$\alpha_s A_p q_s = P + A_p \epsilon \sigma T^4 \quad (275)$$

If this equation is solved for the power transferred to the stream per unit area of the absorbing surface,  $P/A_p$ , then

$$\frac{P}{A_p} = \alpha_s q_s - \epsilon \sigma T^4 \quad (276)$$

If a collection efficiency,  $\eta_c$ , is defined as the ratio of the left-hand side of Eq. 276 to  $q_s$ , the solar input per unit area of the absorber, then the ratio of the collector efficiency to the absorptance for solar radiation can be written:

$$\frac{\eta_c}{\alpha_s} = \frac{P}{\alpha_s q_s A_p} = 1 - \frac{\epsilon}{\alpha_s} \sigma T^4 \quad (277)$$

These last two equations are plotted in Fig. 52 for  $q_s = 442 \text{ Btu/hr ft}^2$  and completely specify the operation of the solar absorbers. Note that for a two-sided collector,  $\epsilon$  represents the sum of the equivalent emissivities of the front and back surfaces. For a case where the collector is not a plane surface but some sort of airfoil,  $\epsilon$  must be increased to account for the fact that the reradiating area is somewhat larger than the normal area,  $A_p$ , which is absorbing the flux.

#### 13.3.2.2 Experimental Results

The unique solar energy test facility, described in Section 13.5 provides a means by which solar energy collectors can be evaluated throughout a range of flux densities and air pressures. It provides a direct means of supplying the following information for various collectors:

1. Stability of the emissivity and absorptance characteristics at high temperatures.
2. Equilibrium temperatures at various levels of operation.

Stability studies have been carried out by adjusting the flux input (servo controlled screen) to yield a desired temperature. This value of flux input is maintained at a constant level despite variations in the energy incident upon the searchlight by means of the feedback servomechanism controlling the screen. The temperature of the sample absorbers is monitored as a function of time and displays the stability of the surface directly.

Equilibrium is achieved when the difference between the absorbed energy and the energy withdrawn is equal to the energy lost; the equilibrium temperature for various energy levels of operation can be determined by simply varying the flux density on the absorber surface. That is to say, it is not necessary to attach any sort of heat exchanger to the surface to withdraw energy in order to study equilibrium temperatures at various levels of operation; it is only necessary to reduce the energy input.

The solar test facility has been in operation for some time. During early tests, the equilibrium temperature of an aluminum surface with a cupric oxide coating at irradiance of  $.160 \text{ Btu/sec ft}^2$  was found to be  $350^\circ\text{F}$ . However, it was found that the flux was not uniform over the surface of the sample because of optical imperfections in the secondary mirror and nonuniformity of the flux control screen. Furthermore, the conductive heat losses through the insulation of the sample holder were larger than expected.

Effort is now being exerted to improve the system by redesigning and building a new sample holder. In the interim, it has been possible to take meaningful data by:

1. Suspending the test samples with nylon thread in order to reduce conduction losses.
2. Allowing radiation to fall directly upon the vacuum test chamber without concentration in the mirror system and without the flux control screen in place in order that the flux be completely uniform.

The last factor prevents taking measurements at other than one level of operation; at about  $0.080 \text{ Btu/sec ft}^2$  net input. (This would have the same net effect as a flux input of  $0.119 \text{ Btu/sec ft}^2$  and a useful power output of  $0.039 \text{ Btu/sec ft}^2$ ).

Both the black nickel on copper collector and the cupric oxide on aluminum collector have been evaluated in the solar test facility. The latter achieved an equilibrium temperature of  $398^\circ\text{F}$  with an irradiance of  $0.0845 \text{ Btu/ft}^2 \text{ sec}$ , while the black nickel surface reached  $452^\circ\text{F}$  with an irradiance of  $0.0814 \text{ Btu/ft}^2 \text{ sec}$ . The absorbing surfaces were operated at these temperatures for thirty minutes with no apparent detrimental affects to the emissivity characteristics of the surface. (Further stability tests will be made when the problems mentioned earlier have been corrected). The equilibrium

temperatures measured were within 8 percent of the temperatures predicted from Eq. 274, the errors being mainly attributed to inaccurate graphical integration of the effective emissivity integrals and to an incomplete knowledge of the diffuse reflectance of the surface.

#### 13.4 Interference Filters

The optical interference filter offers perhaps the most versatile available method for controlling the spectral radiation properties of a solid surface.

Interference filters are composed of one or more layers of optical materials which have varying thicknesses and indices of refraction and which are placed upon a transparent or reflecting surface called a substrate. The thicknesses and refractive indices of the films are chosen in such a way that energy of some wavelengths will be largely transmitted or reflected and energy of other wavelengths will be cancelled out. Interference filters involving more than one surface layer are frequently termed multilayered films. In general, the filters of interest for solar energy collection would involve at least two surface films.

By arranging the layers in the correct manner, a filter can in principle be designed with a specific spectral characteristic. The methods by which such a design would be developed are the subject of this section.

Although interference filters with very good spectral characteristics have been developed, other types of absorbing surfaces offer more promise for the present application. Disadvantages of the interference filters include their probable directional sensitivity and the difficulty of applying them on the thin and fragile surfaces considered for this application. Therefore, the emphasis on this program has been concentrated on other types of selective surfaces. However, much analytical and survey work has been accomplished by the Electro-Optical Systems' staff, as is discussed in the following pages.

##### 13.4.1 Literature Survey

Technical literature has been reviewed (Ref. 29 through Ref. 34) which discusses both the theoretical and experimental aspects of interference filters. The literature survey indicates that interference filters, particularly of the reflection type, offer promise for solar energy collection applications. However, it is apparent also that much remains to be established concerning the general design theory necessary to produce an

arbitrary desired spectral characteristic. Methods are at hand for analyzing a particular filter with given film thicknesses and optical properties, but the direct problem of designing a filter with prescribed characteristics is still in its infancy.

#### 13.4.2 Theory of Thin Film Interference Filters

Filters of this type consist of a series of metal and dielectric films of varying refractive indices and thicknesses laid down on a substrate medium. Their principle of operation is thus:

When a light ray traverses these layers, the new rays formed at the film interfaces have controllable phases and amplitudes with respect to each other. By arranging the thicknesses and indices properly, the new waves can be added algebraically in a wavelength dependent fashion to achieve the desired amount of cancellation or reinforcement.

Interference filters are classified as either transmission or reflection types. It is presently felt that the reflection type filter offers the greatest promise for solar energy applications for the following reasons:

1. No transmission-type filters have been found which possess sufficiently wide band pass characteristics in the infrared.
2. Since transmission filters are directionally sensitive, a transmission filter would be partially ineffective in reflecting the diffuse reradiation.

The reason why reflection filters are promising may be seen by considering the general construction features of these filters. Briefly, they consist of a series of layers arranged in the following manner:

- A - Substrate
- B - Highly Reflecting Metallic Layer
- C,D- Coatings to Produce Low Visible Reflectance

In these filters the combined thickness of layers C and D is of the order of a few half wavelengths of visible light, but it is far less than a wavelength of infrared radiation. Then in the infrared region of the spectrum the phase retardation of the reflected rays is very small and all such rays add in amplitude producing high infrared reflectance and, therefore, low infrared



emissivity. At present there are two ways of constructing filters of this type. These are depicted in the table below.

	Type "A"	Type "B"
Layer C	Semiconductor $\frac{\lambda_o}{4}$	Dielectric $\frac{\lambda_o}{4}$
Layer D	Dielectric $\frac{\lambda_o}{4}$	Metal (very thin)

The notation  $\frac{\lambda_o}{4}$  means that the layer has a thickness of a quarter wavelength for some visible wavelength,  $\lambda_o$ .

It is apparent that considerable latitude is possible in the design of these filters since  $\lambda_o$  and the materials may be chosen at will. Also, there are many possible variations on the two types of design. For instance, the top two layers may be repeated several times, as in the sequence ABCDCDCD ....., etc, or a pair of dielectrics may be put on top giving the sequence ABCDE. The latter should give an additional minimum in the reflectivity versus wavelength curve and lower reflectivity throughout the visible because of better matching of the top film to free space.

The design of a filter to meet the required specifications is by no means a straight forward analytical task; but, rather, requires a long series of iterative calculations in order to determine how the best use may be made of the materials which can be deposited as films.

#### 13.4.3 Three-Layer Film

There are several basic designs which deserve consideration. However, it is most instructive to consider the simplest of these designs. A typical design and reflection characteristic are shown in Fig. 53.

Among the parameters which may be varied are:

1. Thickness and choice of metal for first layer,  $M_1$
2. Refractive index of dielectric,  $D_1$
3. Choice of metal for third layer,  $M_2$

An analytical study by Hadley and Dennison (Ref. 34) yielded equations for the performance of this filter. The things seen to be generally true were:

1. The minima in reflectivity,  $R$ , could be brought down to zero for only one value of resistance (377 ohms per square) of the top layer,  $M_1$
2. This resistance is measured between edges of any sized square of deposited film and is independent of other parameters.
3. As the refractive index of  $D_1$  increases from unity, the difference between  $\lambda_0$  and  $\lambda_1$  increases, and the local maximum in  $R$  increases.

Thus increasing the refractive index of  $D_1$  effectively moves the cutoff wavelength ( $\lambda_c$ ) farther into the infrared when  $\lambda_0$  is kept constant. For filters of this type which absorb the visible, the difference ( $\lambda_1 - \lambda_0$ ) is only about  $0.6 \mu$ . Thus, since the difference ought to be more like  $2 \mu$ , a higher index should be desirable. However, a compromise must be reached, since a higher index would make the filter less absorbing between  $\lambda_0$  and  $\lambda_1$ . For a given choice of metals, then, the results of several different choice of indices must be compared, and the best of these results for each metal must be chosen as the optimum filter.

#### 14. CONCLUSIONS AND RECOMMENDATIONS

Without considering the value of a solar powered aircraft of configuration and performance as developed in this study, the following conclusions and recommendations are offered regarding the technical feasibility of such a device:

- a. The results of this study indicate that a solar powered aircraft of large aspect ratio, 1000-foot wing chord length, flying continuously directly beneath the sun at an altitude of about 220,000 ft with wing loading of  $0.42 \text{ lbs/ft}^2$  is feasible, based on considerations of aerodynamics, heat transfer, and energy collection.
- b. However, before undertaking the large-scale experimental development required for final realization of the solar powered aircraft, a more elaborate design and performance analysis is necessary. This analysis should include complete and detailed machine performance calculations, as well as consideration of the following problems which were not included in the scope of the present study: structures, control and stability, maneuverability, launch and recovery, durability, operation non-normal to the sun direction, cost, applications, and comparison with competitive systems.

## REFERENCES

1. R. A. Minzer and W. S. Ripley, The ARDC Model Atmosphere, 1956, AFRCR. TN 56-24, ASTIA No. 110233, December 1956.
2. R. Hermann, Supersonic Inlet Diffusers and Introduction to Internal Aerodynamics, Minneapolis-Honeywell Regulator Company, 1956.
3. Antonio Ferri, Air Intake Problems in Supersonic Propulsion, p. 48, Pergamon Press, 1958
4. E. R. G. Eckert and Robert M. Drake, Jr., Heat and Mass Transfer, McGraw-Hill, 1959
5. Ascher H. Shapiro, Compressible Fluid Flow, Vol. I, Ronald Press
6. Ames Research Staff, Equations, Tables and Charts for Compressible Flow, NACA Report 1135, 1953.
7. Dean R. Chapman and Morris W. Rubesin, "... Compressible Laminar Boundary Layer ...", Jour. IAS, September 1959.
8. Hermann Schlichting, Boundary Layer Theory, Pergamon Press, 1955
9. Contract No. AF(616)-5977, Feasibility of a Solar Energy Device, EOS Report No. 220-QL-6, 31 December 1959.
10. Antonio Ferri, Elements of Aerodynamics of Supersonic Flows, MacMillan Company, 1949
11. Joseph H. Keenan and Joseph Kaye, Thermodynamic Properties of Air, John Wiley and Sons, Inc., 1945
12. H. Tabor, Proc. Solar Energy Symposium, Phoenix, 1955
13. Thomas A. Unger, The Preparation of Selectively Black Surface for Use in the Collection of Solar Energy, Ph.D Thesis, M.I.T., 1958
14. W. Shockley, Electrons and Holes in Semi-Conductors, D. von Nostrand, 1950
15. G. Mie, Ann. Physik, 25, p. 377, 1908
16. H. C. von de Hulst, Light Scattering by Small Particles, Wiley, 1957
17. L. Harris, R. McGinnis, and B. Siegel, The Preparation and Properties of Gold Blacks, J. Opt. Soc. Am., 38, p. 582, 1948

18. Plyler and Ball, Infrared Absorption of Deposited Blacks, J. Opt. Soc. Am., 38, p. 988, 1948
19. Harris and Beasley, The Infrared Properties of Gold Smoke Deposits, J. Opt. Soc. Am., 42, p. 134, 1952
20. Operating Instructions for Ebonol "C", Enthone, Inc., 442 Elm St., New Haven 8, Connecticut
21. Chemical Treatment No. 8, Metal Finishing Guidebook, 1958, Finishing Publications, Inc., 219 W. 7th St., Los Angeles, p. 513
22. Nickel Pentrate, Heatbath Corp., Box 78, Springfield, Mass.
23. A. T. Marinaro and Louis Packman, Black Nickel Plating, Metal Finishing Guidebook, 1958, p. 391-2
24. Dura-Black, Heatbath Corp., Box 78, Springfield, Massachusetts
25. G. Kortum and J. O'M. Brockris, Textbook of Electrochemistry, New York, 1951, p. 564
26. U. S. Patents 2, 756, 165; 2,695,247; 2,694,649; 2,692,836; 2,564,706; 2,467,144; 2,124,589; 2,564,987; 2,516,663; 2,475,379; 2,429,420; 2,118,795; 894,845
27. Z. Naturforsch, 9a, 508-11, 1954 (Theory of  $\text{SnO}_2$ ,  $\text{In}_2\text{O}_3$ , etc., coatings.)
28. J. T. Gier and R. V. Dunkle, Selective Spectral Characteristics as an Important Factor in the Efficiency of Solar Collectors, Transactions of the Conference on the Use of Solar Energy, Tucson, Arizona, 1955, p. 47, Fig. 8
29. O. S. Heavens, Optical Properties of Thin Solid Films, Butterworth, London
30. L. Holland, Vacuum Deposition of Thin Films, Wiley, New York
31. Haas, Turner, and Schroeder, Mirror Coatings for Low Visible and Low Infrared Reflectance, Journal of the Optical Society of America, v. 46, p. 31, (1956)
32. L. I. Epstein, The Design of Optical Filters, Journal of Optical Society of America, v. 42, p. 806, (1952)
33. Haas, Filmed Surfaces for Reflective Optics, Journal of the Optical Society of America, v. 45, p. 945, (1955)
34. Hadley and Dennison, Reflection and Transmission Interference Filters, Journal of the Optical Society of America, v. 37, p. 451, (1947), and v. 38, p. 483, (1948)

TABLE I

FLIGHT CONDITIONS FOR TWENTY-FOUR HOUR EARTH SATELLITE  
SOLAR POWERED AIRCRAFT

H	$\frac{P}{P_o}$	T	M	q	$(v/\nu)_1$	$P_R$	$T_R$	$(v/\nu)_2$
ft/1000		$^{\circ}R$		lbs/ft <sup>2</sup>	ft <sup>-1</sup>	mm Hg	$^{\circ}R$	ft <sup>-1</sup>
190	3.11	474	1.43	1.03	3550	0.738	657	1540
	$\times 10^{-4}$							
200	2.08	457	1.47	0.76	2575	0.522	643	1130
210	1.36	432	1.50	0.454	1850	0.356	613	806
	$\times 10^{-4}$							
220	8.71	410	1.54	0.307	1290	0.242	594	568
	$\times 10^{-5}$							
230	5.44	389	1.59	0.204	895	0.163	576	395
240	3.32	367	1.63	0.131	605	0.105	552	272
250	1.96	354	1.66	0.080	384	0.065	540	173
260	1.16	354	1.66	0.047	226	0.039	540	104

H = Flight altitude

$P/P_o$  = Ratio of ambient pressure to sea level pressure

T = Atmosphere temperature

M = Aircraft flight Mach number

q = Flight dynamic pressure

$(v/\nu)_1$  = Aircraft flight Reynolds number per foot

$P_R, T_R$  = Pressure and temperature, respectively for air compressed isentropically from free stream conditions to M = .3.

$(v/\nu)_2$  = Reynolds number per foot of the air at M = .3

TABLE II INPUT DATA FOR PERFORMANCE COMPUTATIONS

Case	Z Feet	M <sub>1</sub>	y <sub>1</sub> Feet	M <sub>2</sub>	R <sub>P<sub>D</sub></sub>	W/y <sub>1</sub>	$\frac{d}{dx} \left( \frac{y}{y_2} \right)$	x <sub>f</sub> /y	x <sub>p</sub> /x <sub>f</sub>	η <sub>o</sub>	E <sub>ff</sub>	E <sub>uu</sub>
I	200,000	1.468	20.000	.300	.93	2.00	0	.01142	0	.9150	.0200	.0300
II							.050	↓				
III							↓	.00285				
IV							.025	↓				
V								↓				
VI								.0457				
VII							↓	.1828				
VIII							.0125	.0457				
IX				.200			0	↓				
X							0	.01142				
XI							.025	↓				
XII							.0250	.00285				
XIII							.0375	.01142				
XIV	220,000	1.5404					0	.00285				

\*The inadvertent doubling of y<sub>2</sub>/2m in this case doubles the friction at the walls for the internal flow.

\*\*In this case, the friction of the internal flow was arbitrarily halved.

C-600-4



# INPUT DATA FOR PERFORMANCE COMPUTATIONS

$x_f/y$	$x_p/x_f$	$\eta_o$	$E_{ff}$	$E_{uu}$	$E_{ll}$	$E_{uf}$	$E_{lf}$	$E_{su}$	Remarks
.01142 ↓	0 ↓	.9150 ↓	.0200 ↓	.0300 ↓	.0300 ↓	.0200 ↓	.0200 ↓	.0308 ↓	$y_2/2m$ doubled*
.00285 ↓	↓	↓	↓	↓	↓	↓	↓	↓	
.0457 ↓	↓	↓	↓	↓	↓	↓	↓	↓	used $1/2 f/2m^{**}$
.1828 ↓	↓	↓	↓	↓	↓	↓	↓	↓	
.0457 ↓	↓	↓	↓	↓	↓	↓	↓	↓	Not completed
.01142 ↓	↓	↓	↓	↓	↓	↓	↓	↓	
.00285 ↓	↓	↓	↓	↓	↓	↓	↓	↓	
.01142 ↓	↓	↓	↓	↓	↓	↓	↓	↓	
.00285 ↓	↓	↓	↓	↓	↓	↓	↓	↓	

on at the walls for the internal flow.  
olved.

2



TABLE III

## SUMMARY OF RESULTS OF PERFORMANCE COMPUTATIONS

<u>Case</u>	<u>x<sub>c</sub></u> <u>Feet</u>	<u>Excess*</u> <u>Thrust</u> <u>Coefficient</u>	<u>w/x<sub>c</sub><sup>**</sup></u> <u>lbs/ft<sup>2</sup></u>
I	200.7	-0.004939	--
II	800	-0.001651	--
II	1000	-0.001600	--
III	300	-0.008370	--
III	1000	-0.002060	--
III	1400	-0.001455	--
III	1800	-0.001676	--
IV	400	-0.003127	--
V	1200	+0.001078	.045408
V	1400	+0.000891	.041279
V	1430	+0.000346	.025733
VI	1000	+0.000230	.020972
VI	1400	+0.000139	.016283
VII	1800	-0.000299	--
VIII	800	+0.000214	.022236
IX		Not Completed	
X	800	+0.000385	.027125
XI	800	-0.001804	--
XI	1400	+0.000254	.022023
XI	1800	+0.000850	.041797
XII	1400	+0.000489	.030580
XIII	1800	-0.000166	--
XIV	500	+0.002689	.032556

$$* \text{ Excess Thrust Coefficient} = \frac{F}{q x_c} - C_{Do} - C_{Df}$$

$$** \text{ Wing Loading} = w/x_c \text{ lbs/ft}^2$$

System	Spectral Properties			Spectral Characteristics	Stability		Uniformity	Ease of Fabrication	Cost
	Solar Reflectance %	Wavelength of Infection $\mu$	Infrared Emissivity, % Above 7 $\mu$		Mechanical	Chemical			
Cupric Oxide on Aluminum by the Unger Process	0-10	2.8	0-15	Very good	Fair	Excellent	Very good	With some difficulty	Low
Black Nickel on Copper	3-10	1.4	2-10	Very good	Excellent	Good	Very good	With some difficulty	Low
Black Nickel on Nickel	3-7	3.4-3.7	6-14	Very good	Excellent	Excellent	Very good	With some difficulty	Low
Cupric Oxide on Copper by the Dura Black Process	0	5	0	Good	Fair	Good	Very good	With ease	Low
Platinum Black on Platinum	0-1	2.5-3.0	0	Excellent	Poor	Excellent	Very good	With ease	Very high
Carbon Black on Aluminum	1-6	2.2	8-24-	Fair	Poor	Excellent	Very good	With ease	Low

TABLE IV  
COMPARISON OF PROPERTIES FOR THE BEST OPAQUE  
SPECTRALLY SELECTIVE SURFACES

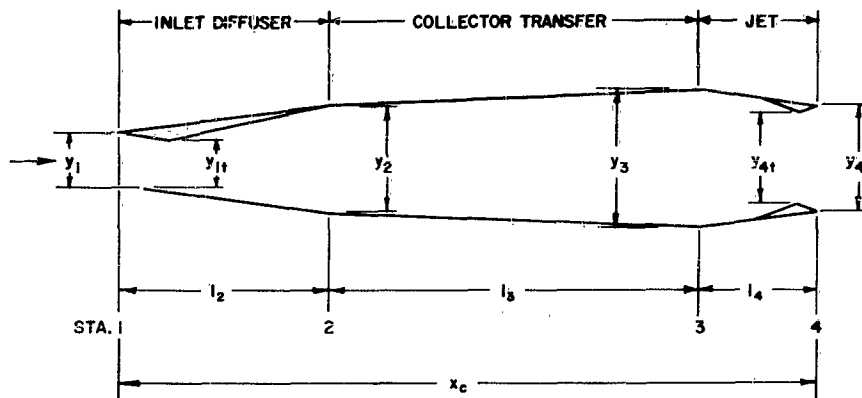


FIG. 1 SOLAR POWERED AIRCRAFT CONFIGURATION - WING CROSS SECTION

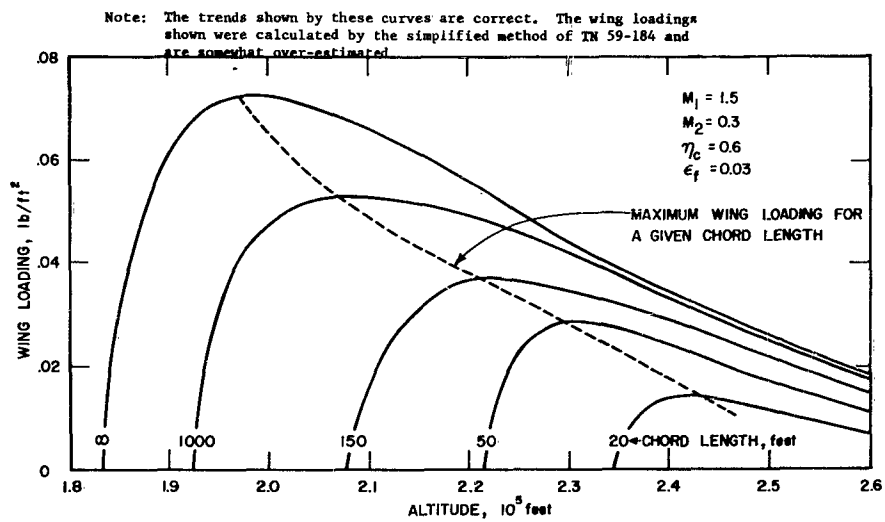


FIG. 2 WING LOADING VS ALTITUDE FOR VARIOUS VALUES OF CHORD LENGTH (FROM TN 59-184)

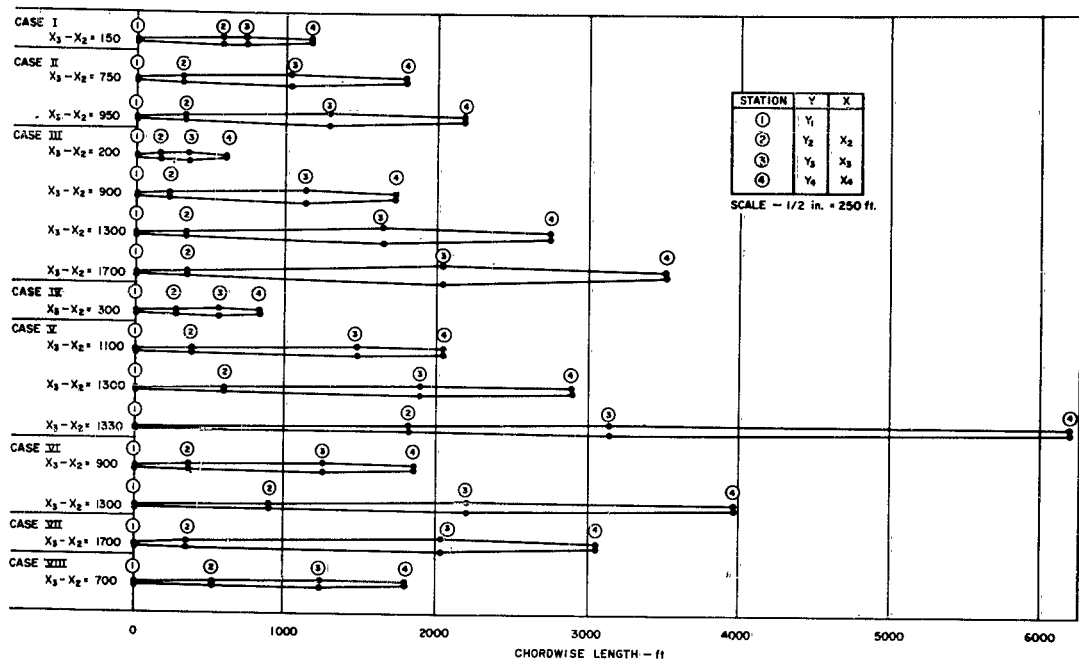


FIG. 3a SOLAR POWERED AIRCRAFT CONFIGURATIONS (WING CROSS SECTIONS)

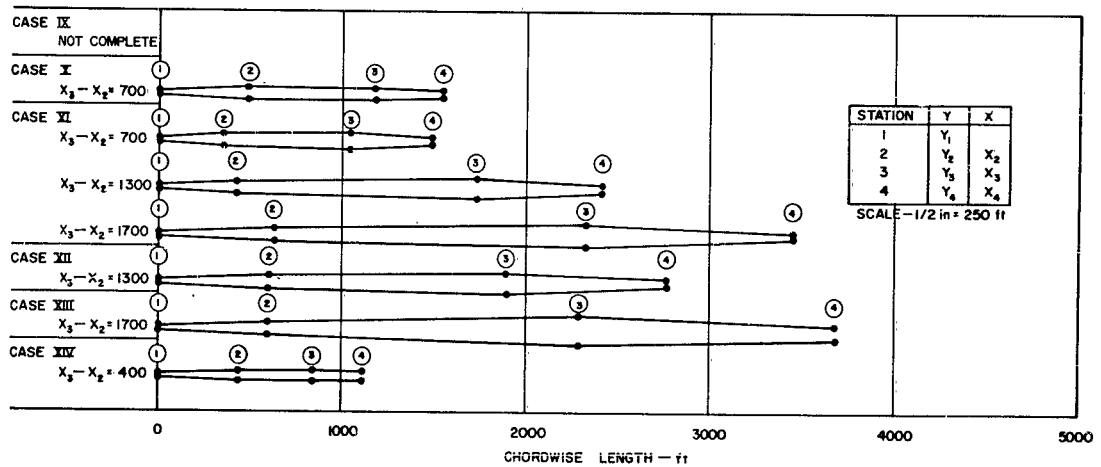


FIG. 3b SOLAR POWERED AIRCRAFT CONFIGURATIONS (WING CROSS SECTIONS)

# NOTATION FOR FIGURES 4 THROUGH 15

$F$	=	thrust per unit span, lbs/ft
$f_2$	=	$\frac{1}{q_s}$ x (energy flux transferred to the internal stream)
$M_3$	=	internal stream Mach Number
$P_s^*$	=	$\frac{P_s}{P_{s2}}$ = internal stream stagnation pressure ratio
$P_s$	=	internal stream stagnation pressure
$P_{s2}$	=	internal stream stagnation pressure at Station 2.
$T_f^*$	=	$\frac{T_f}{T_{s2}}$ = heat transfer foil temperature ratio
$T_\ell^*$	=	$\frac{T_\ell}{T_{s2}}$ = lower wing surface temperature ratio
$T_u^*$	=	$\frac{T_u}{T_{s2}}$ = upper wing surface temperature ratio
$T_s^*$	=	$\frac{T_s}{T_{s2}}$ = internal stream stagnation temperature ratio
$T_s$	=	internal stream stagnation temperature
$T_{s2}$	=	internal stream stagnation temperature at Station 2.
$T_f, T_\ell, T_u$	=	temperatures of heat transfer foils, upper and lower wing surfaces, respectively.

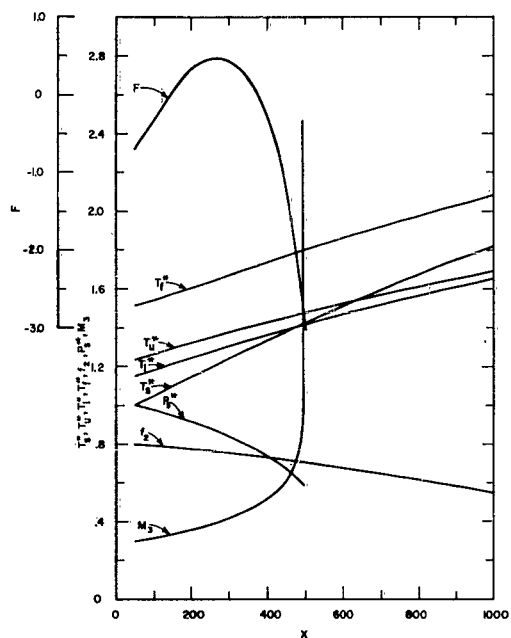


FIG. 4  
DETAILS OF PERFORMANCE  
COMPUTATION RESULTS, CASE I

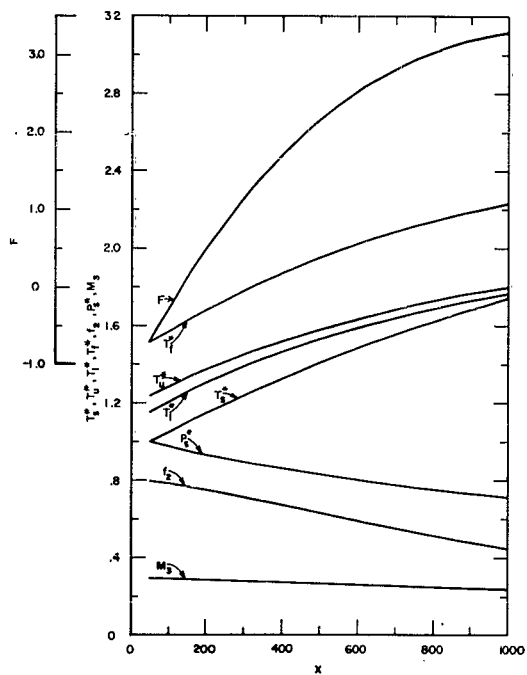


FIG. 5  
DETAILS OF PERFORMANCE  
COMPUTATION RESULTS, CASE II

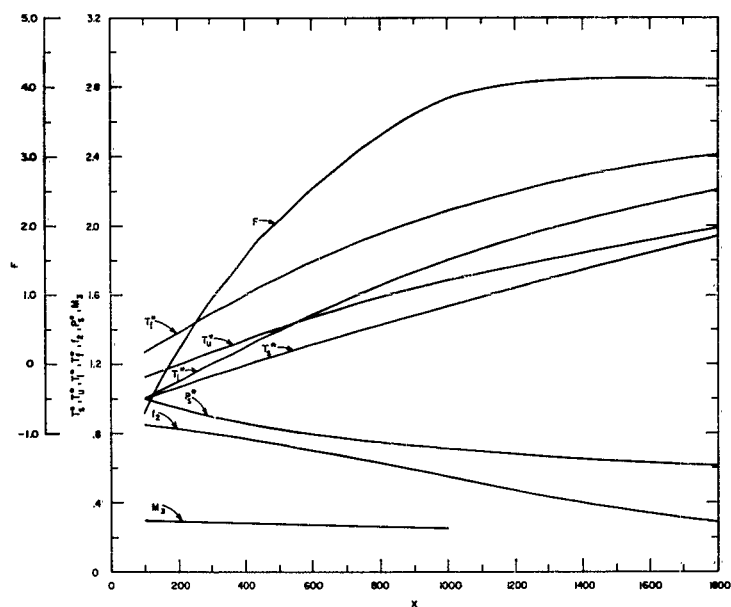


FIG. 6 DETAILS OF PERFORMANCE COMPUTATION RESULTS,  
CASE III

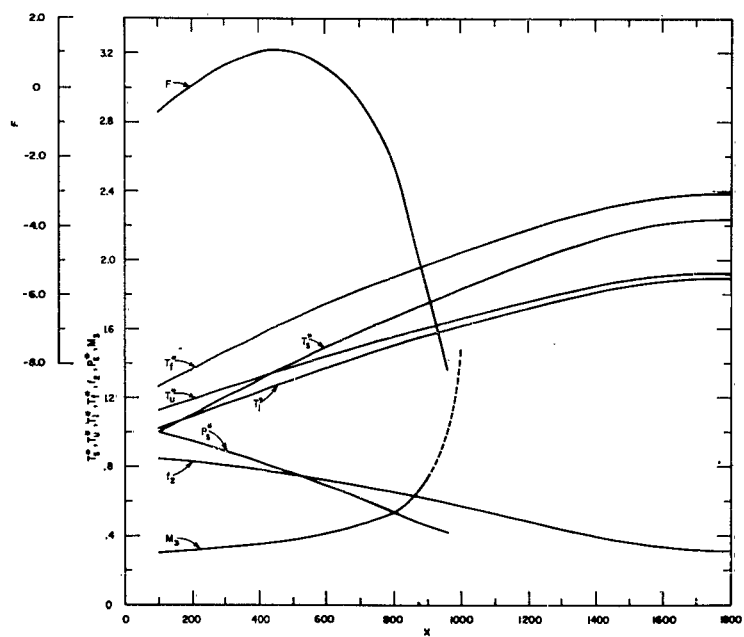


FIG. 7 DETAILS OF PERFORMANCE COMPUTATION RESULTS,  
CASE IV

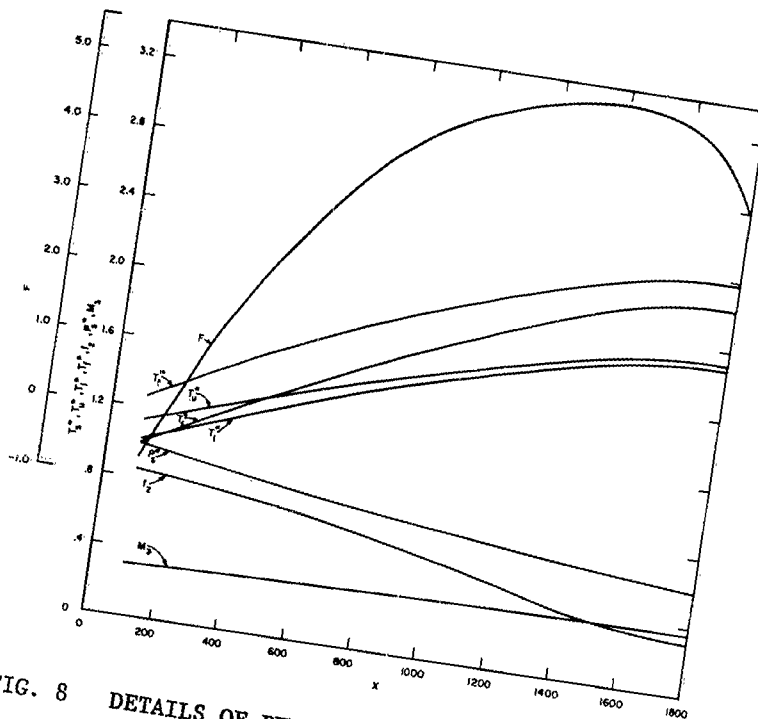


FIG. 8 DETAILS OF PERFORMANCE COMPUTATION RESULTS,  
CASE V

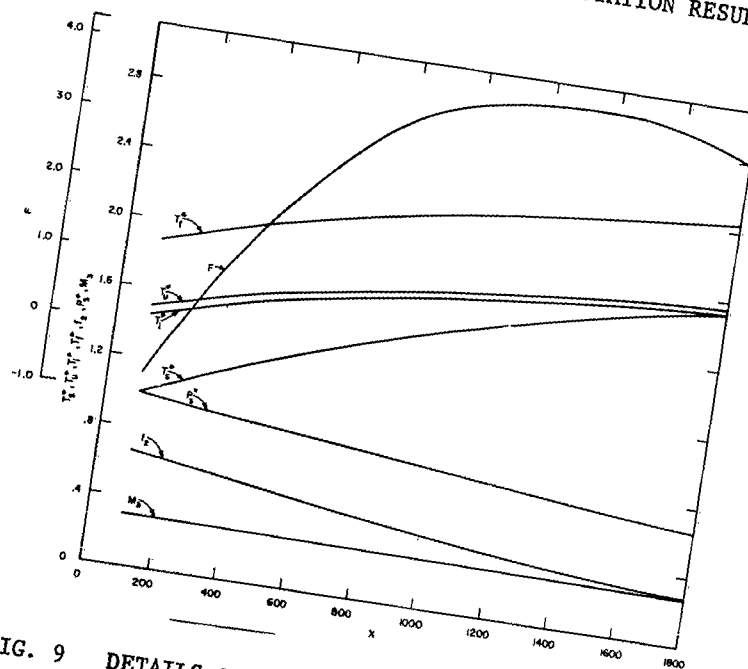


FIG. 9 DETAILS OF PERFORMANCE COMPUTATION RESULTS,  
CASE VI



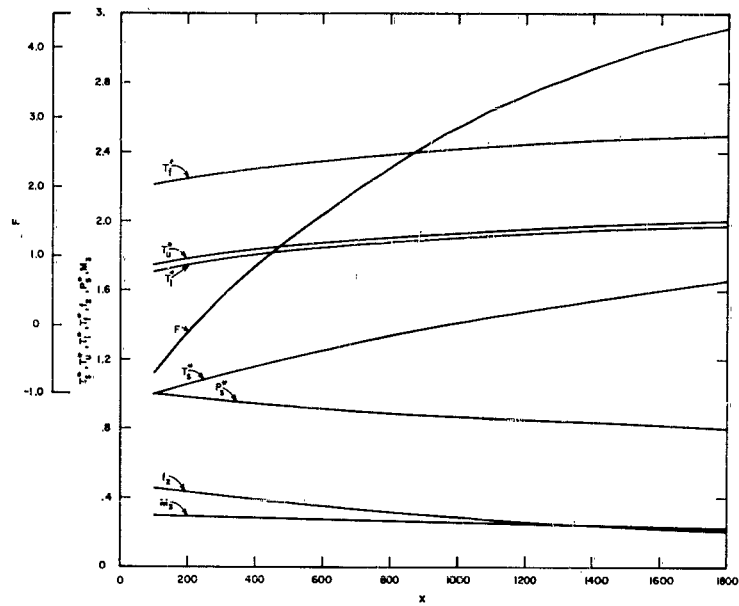


FIG. 10 DETAILS OF PERFORMANCE COMPUTATION RESULTS, CASE VII

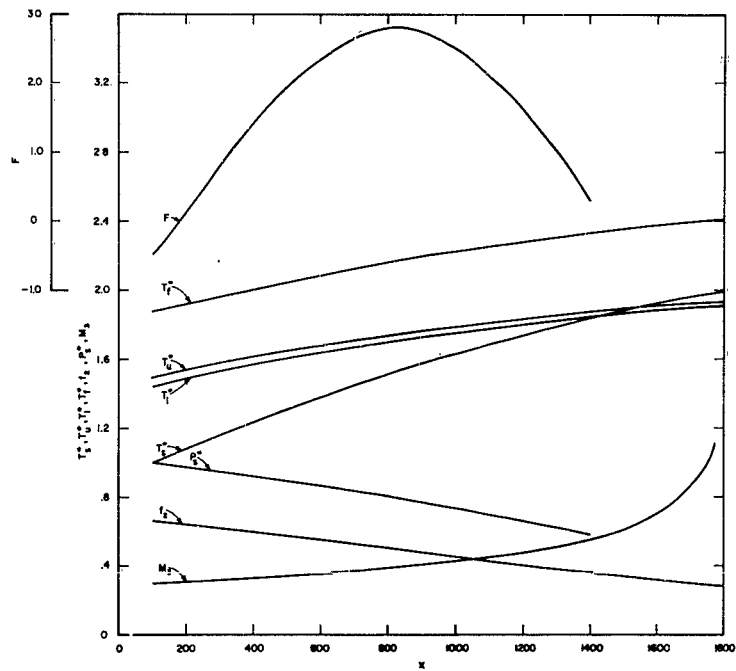


FIG. 11 DETAILS OF PERFORMANCE COMPUTATION RESULTS, CASE VIII

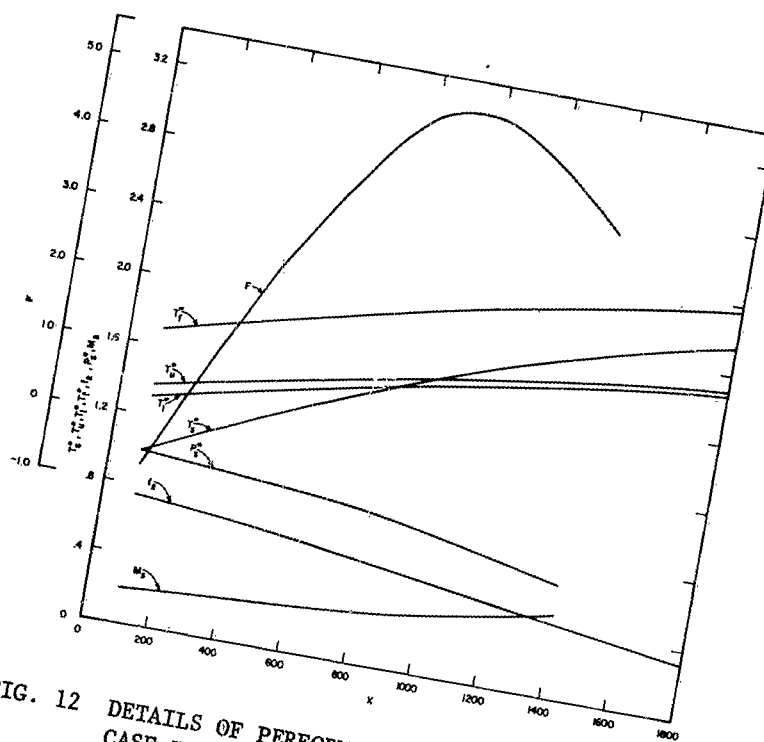


FIG. 12 DETAILS OF PERFORMANCE COMPUTATION RESULTS,  
CASE X

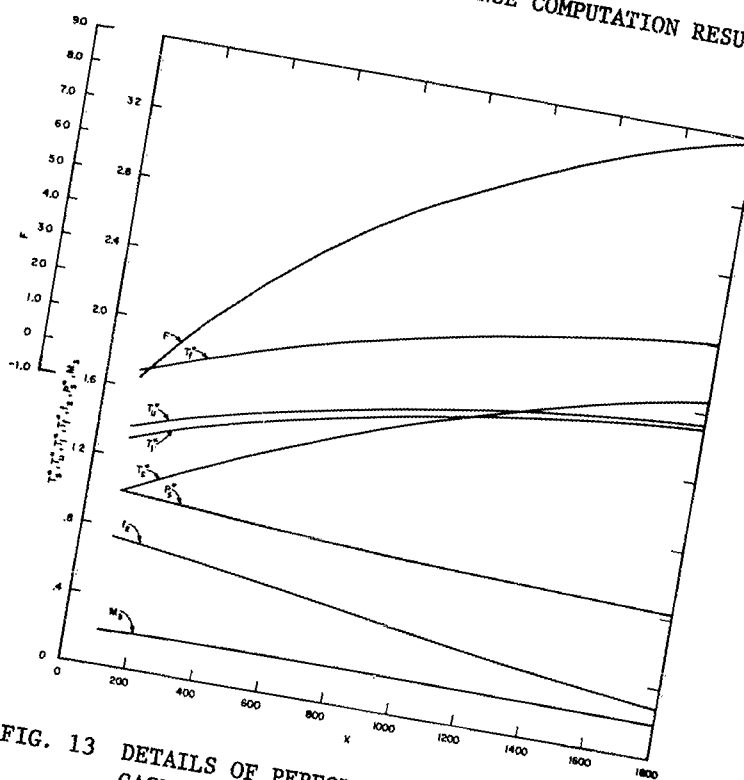


FIG. 13 DETAILS OF PERFORMANCE COMPUTATION RESULTS,  
CASE XI

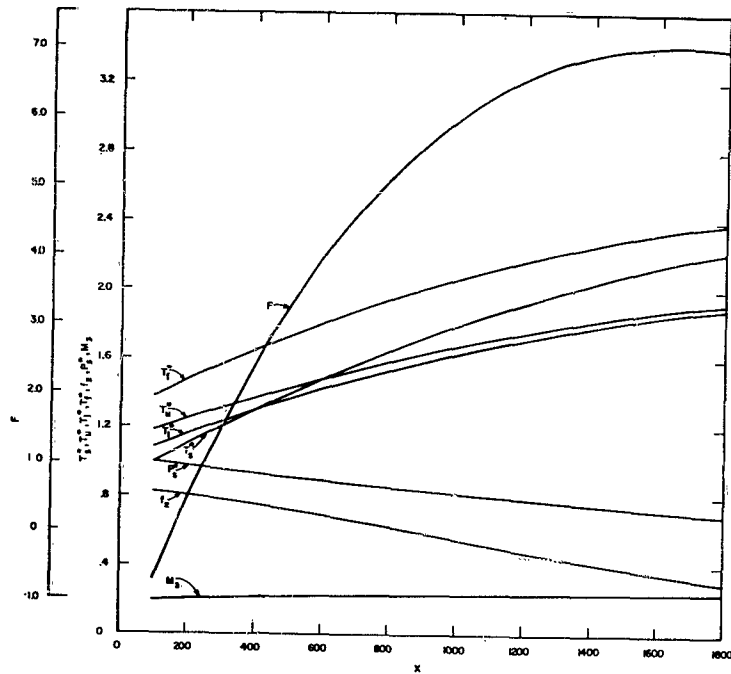


FIG. 14 DETAILS OF PERFORMANCE COMPUTATION RESULTS, CASE XII

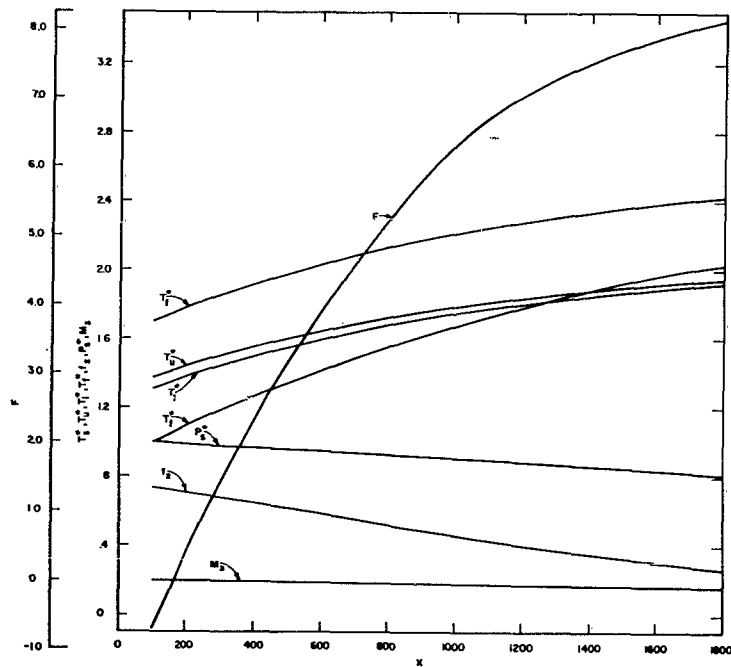


FIG. 15 DETAILS OF PERFORMANCE COMPUTATION RESULTS, CASE XIII

# NOTATION FOR FIGURES 16 THROUGH 19

- $q_s$  = insolation, ft.lbs/sec.ft.<sup>2</sup>
- $Q$  = heat transfer rate per unit span to the internal stream, ft.lbs./sec.ft.
- $\eta_o$  =  $\frac{1}{q_s} \times$  (solar energy flux absorbed by the collector-transfer section.)
- $C_{ext}$  = heat flux by convection from the wing surfaces to the external stream, ft.lbs/sec-ft<sup>2</sup>
- $C_f$  = heat flux by convection from the collector-transfer foils to the internal stream, ft.lbs/sec-ft<sup>2</sup>
- $C_{int}$  = heat flux by convection from the collector-transfer wall surfaces to the internal stream, ft.lb/sec-ft.<sup>2</sup>
- $x$  = chordal distance from wing leading edge, ft.
- $R$  = radiation flux lost from upper and lower wing surfaces, ft.lbs/sec-ft<sup>2</sup>

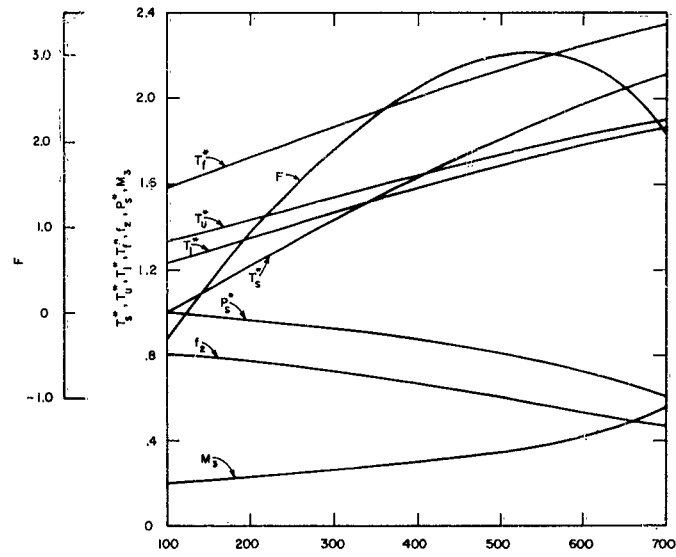


FIG. 16 DETAILS OF PERFORMANCE COMPUTATION RESULTS, CASE XIV

$$\frac{1}{q_s} \frac{dQ}{dx} = \eta_o - \frac{R}{q_s} - \frac{C_{axl}}{q_s} = \frac{C_f}{q_s} - \frac{C_{int}}{q_s}$$

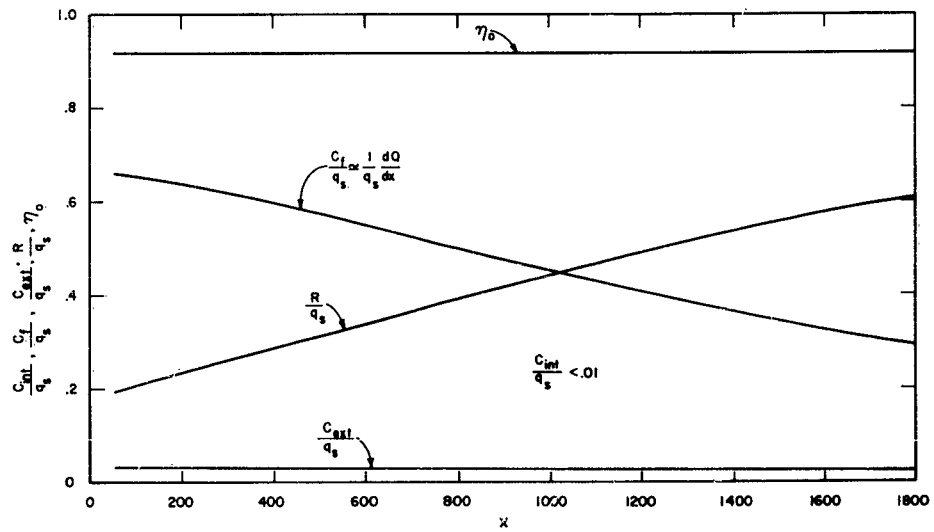


FIG. 17 ENERGY FLUX DETAILS, CASE VIII

$$\frac{1}{q_s} \frac{dQ}{dx} = \eta_0 - \frac{R}{q_s} - \frac{C_{ext}}{q_s} - \frac{C_f}{q_s} - \frac{C_{int}}{q_s}$$

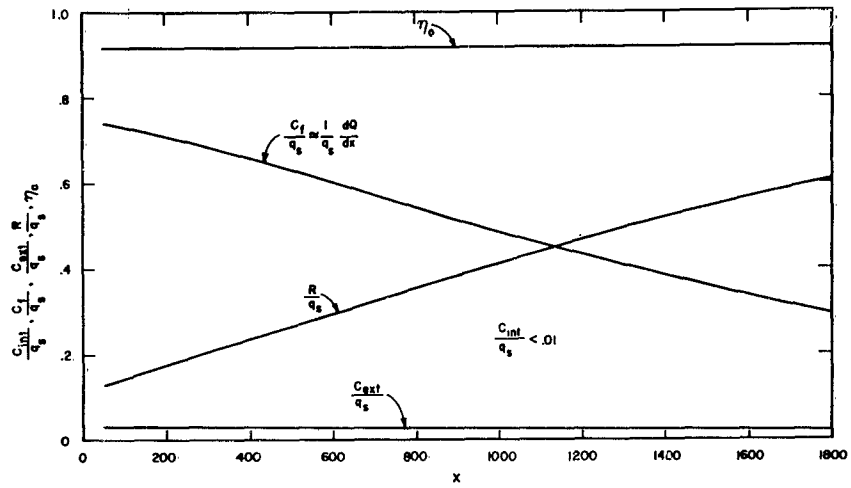


FIG. 18 ENERGY FLUX DETAILS, CASE XI

$$\frac{1}{q_s} \frac{dQ}{dx} = \eta_0 - \frac{R}{q_s} - \frac{C_{ext}}{q_s} - \frac{C_f}{q_s} - \frac{C_{int}}{q_s}$$

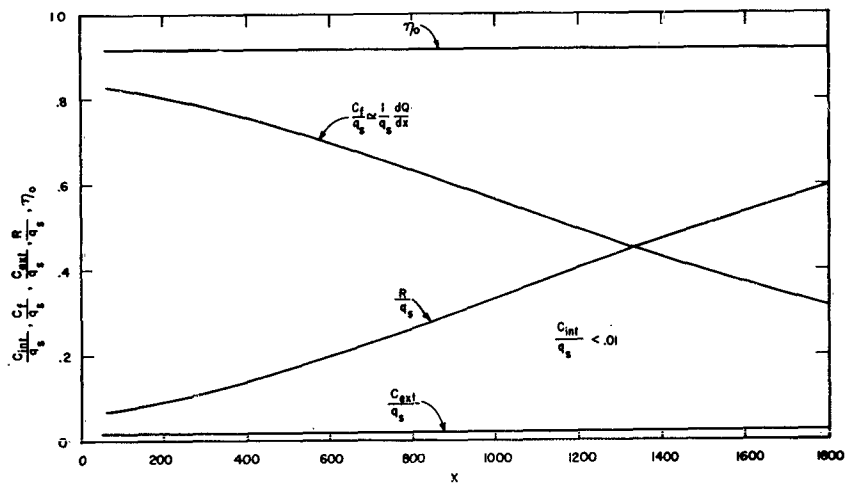


FIG. 19 ENERGY FLUX DETAILS, CASE XII

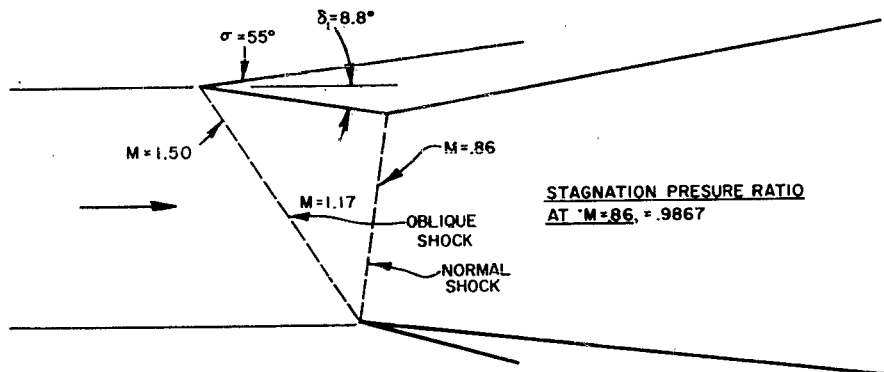


FIG. 20 INLET DIFFUSER CONFIGURATION

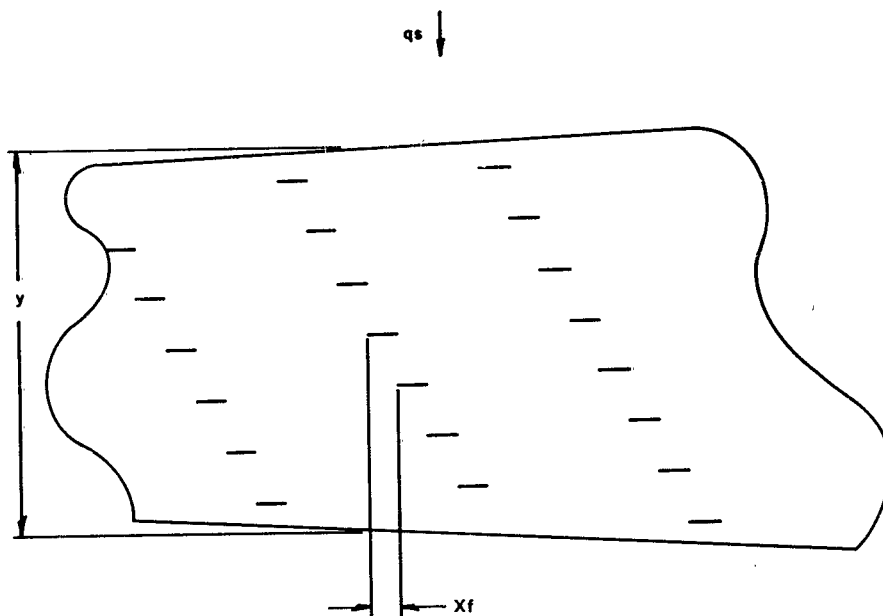


FIG. 21 ARRANGEMENT OF RADIATION COLLECTOR-HEAT TRANSFER FOILS  
IN THE COLLECTOR-TRANSFER SECTION

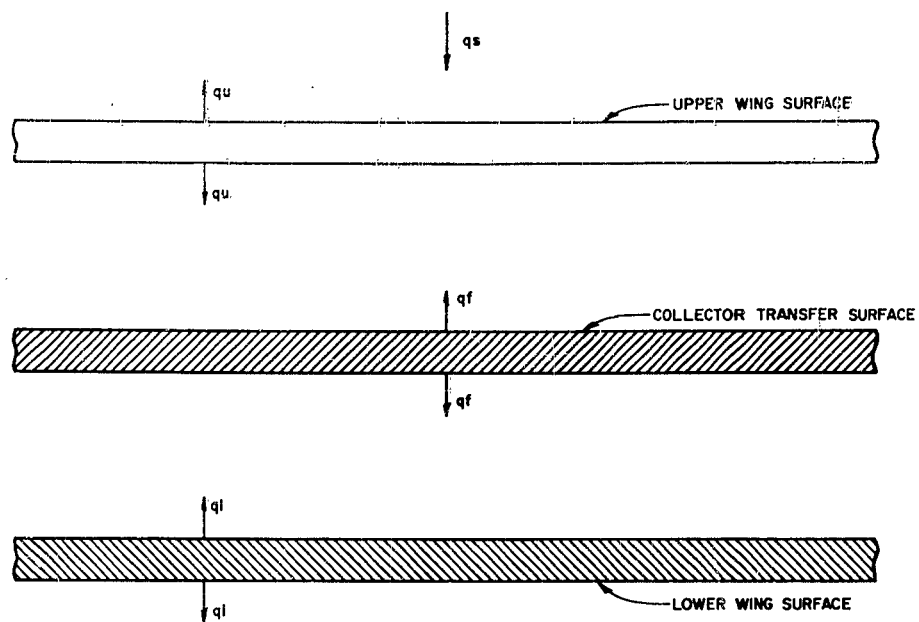


FIG. 22 ELEMENTARY RADIATION COLLECTOR CONSISTING OF INFINITE PARALLEL SURFACES

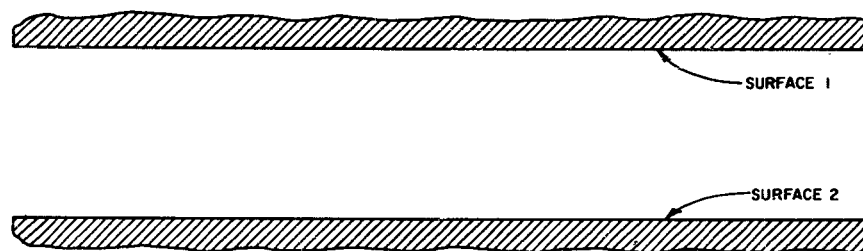


FIG. 23 RADIANT ENERGY EXCHANGE BETWEEN INFINITE PARALLEL SURFACES

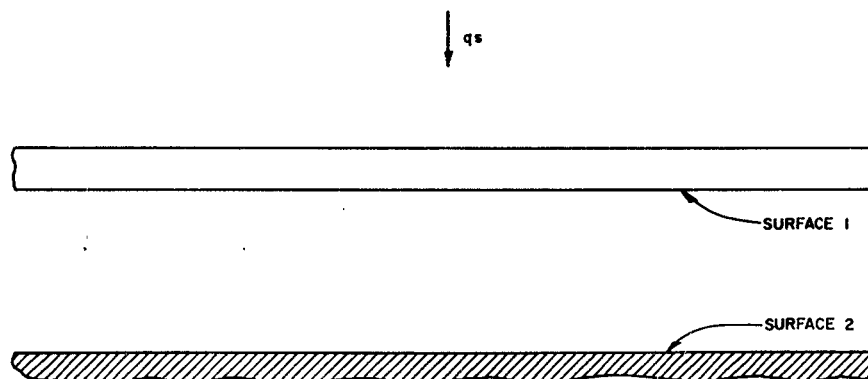


FIG. 24 "GREEN HOUSE" EFFECT BETWEEN INFINITE PARALLEL SURFACES



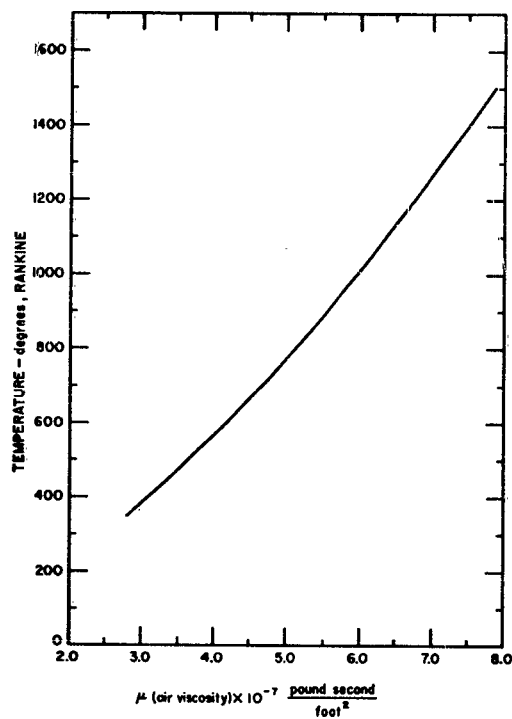


FIG. 25  
AIR, VISCOSITY

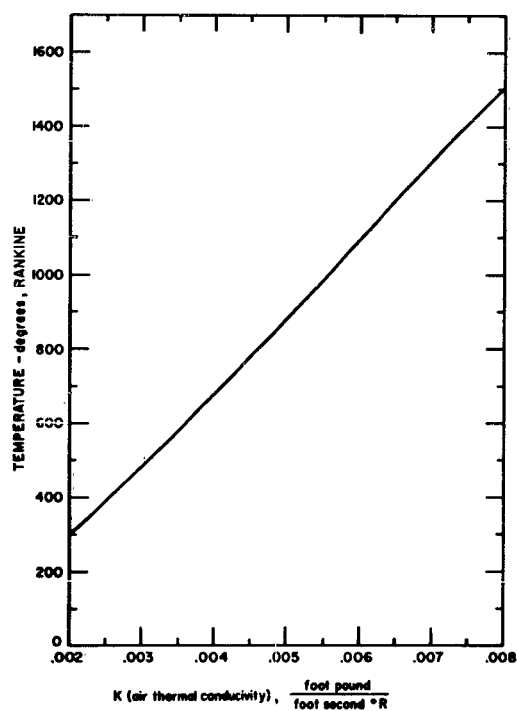


FIG. 26  
AIR, THERMAL CONDUCTIVITY

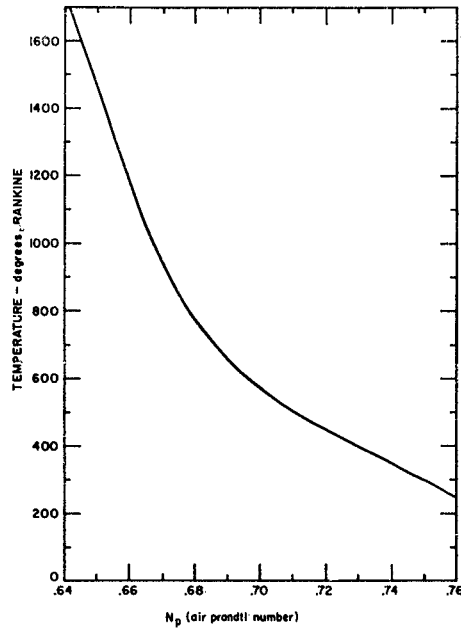


FIG. 27  
AIR, PRANDTL NUMBER

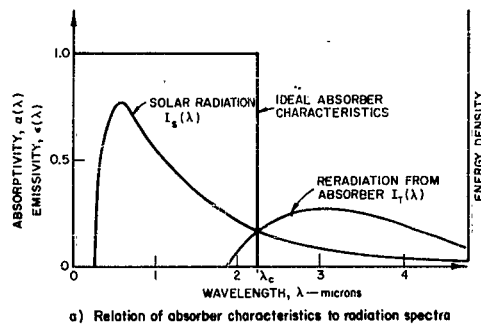
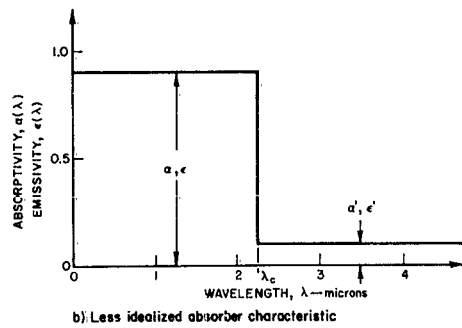


FIG. 28  
ABSORPTION-EMISSION  
CHARACTERISTICS OF SOLAR  
ENERGY ABSORBING SURFACES



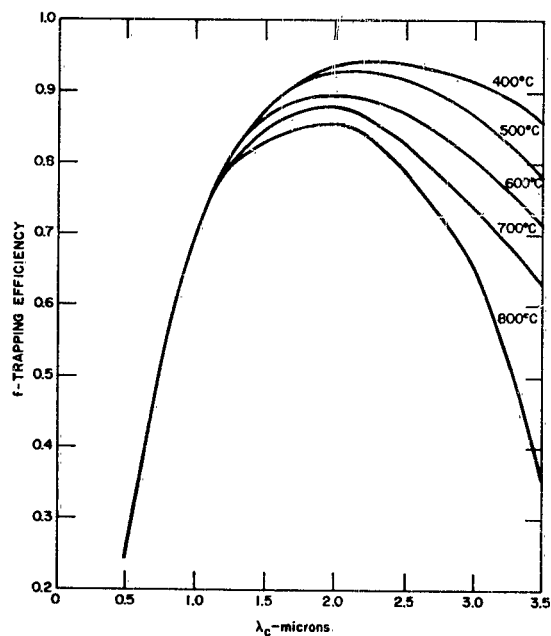


FIG. 29

TRAPPING EFFICIENCY (f) VS  
CUTOFF WAVELENGTH ( $\lambda_c$ ) FOR  
AN IDEAL COLLECTOR

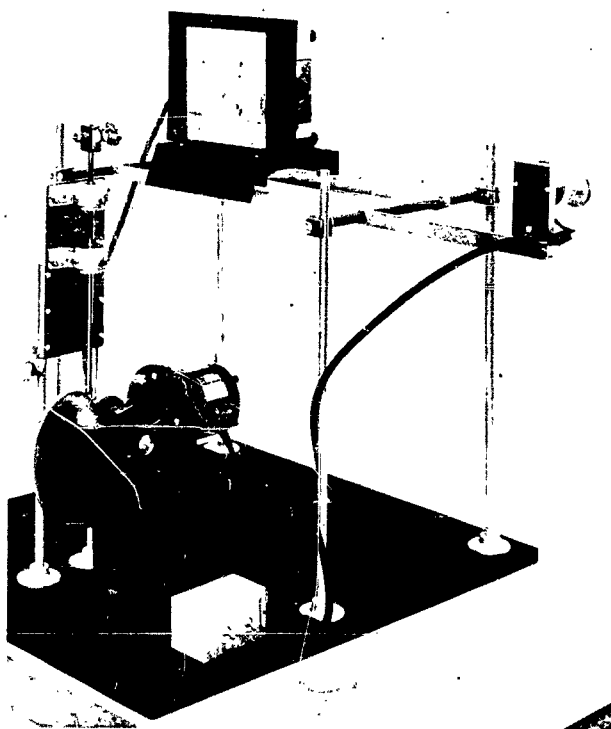


FIG. 30 SPRAYED COATINGS ARE EVENLY APPLIED  
TO TEST SAMPLES BY USE OF CAM-  
OSCILLATED NOZZLE AND TRAVELING  
HOT-PLATE

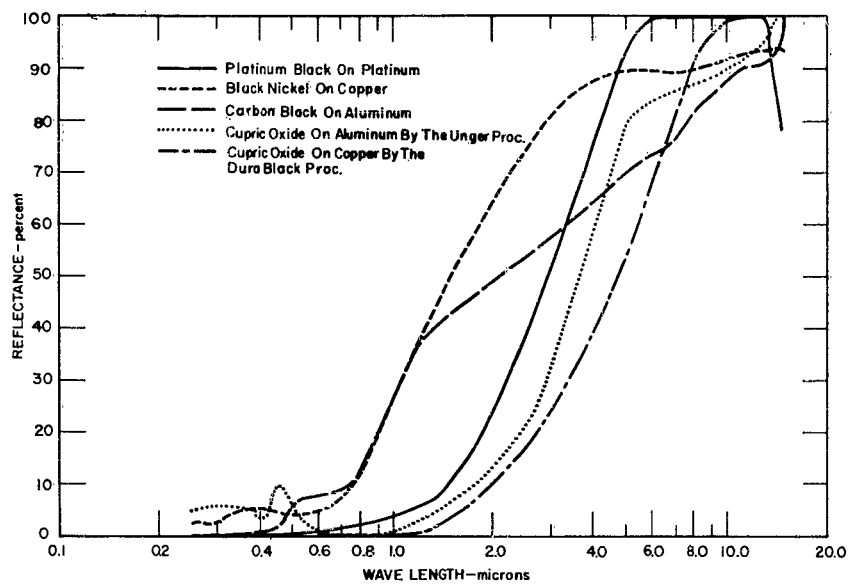


FIG. 31 COMPARISON OF VARIOUS TYPES OF BLACK SURFACES

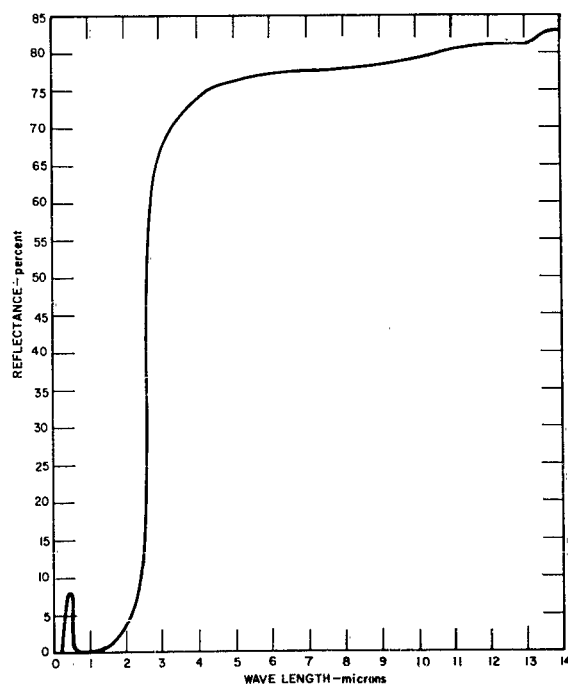


FIG. 32  
REFLECTANCE OF NESA  
GLASS, 0.25 $\mu$ -14 $\mu$   
(SAMPLE NO. P-6)  
10.5 ohms/sq.

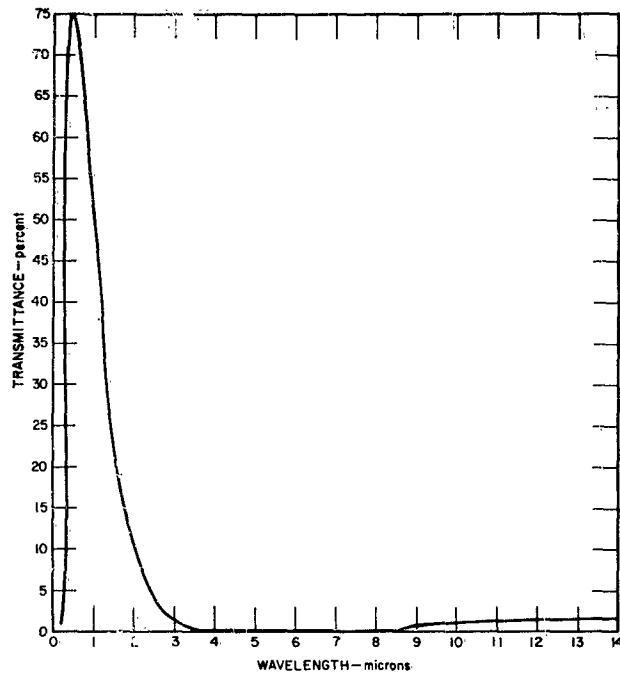


FIG. 33

TRANSMITTANCE OF NESA GLASS,  
0.25 $\mu$ -14 $\mu$  (SAMPLE NO. P-6)  
10.5 ohms/sq.

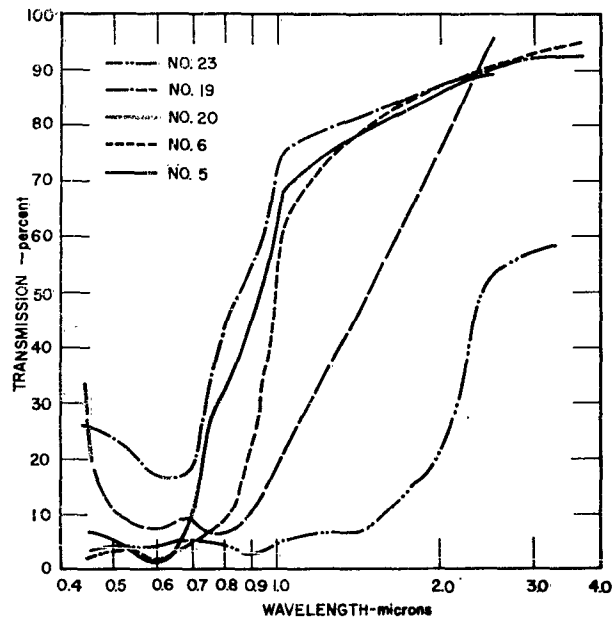


FIG. 34

TRANSMISSION CHARACTERISTIC  
OF GOLD SMOKE FILTERS

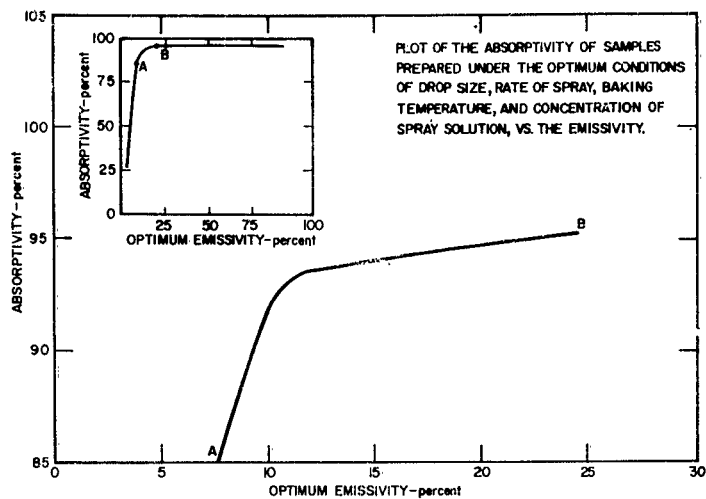


FIG. 35 OPTIMUM EMISSIVITY VS ABSORPTIVITY REFERENCE

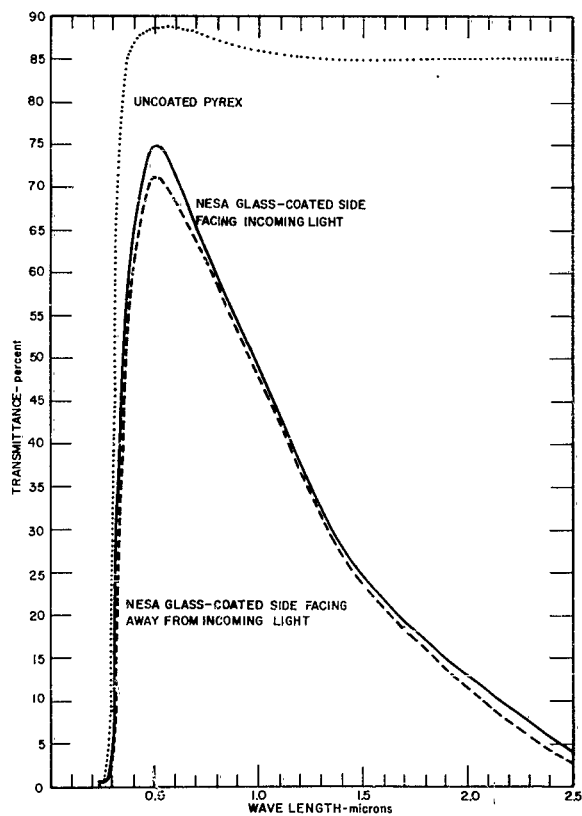


FIG. 36  
TRANSMITTANCE OF PYREX AND  
NESA GLASS

TRANSMITTANCE OF PYREX AND NESA GLASS,  $0.25\mu-2.5\mu$   
Sample No. P-6, thickness  $\frac{1}{16}$

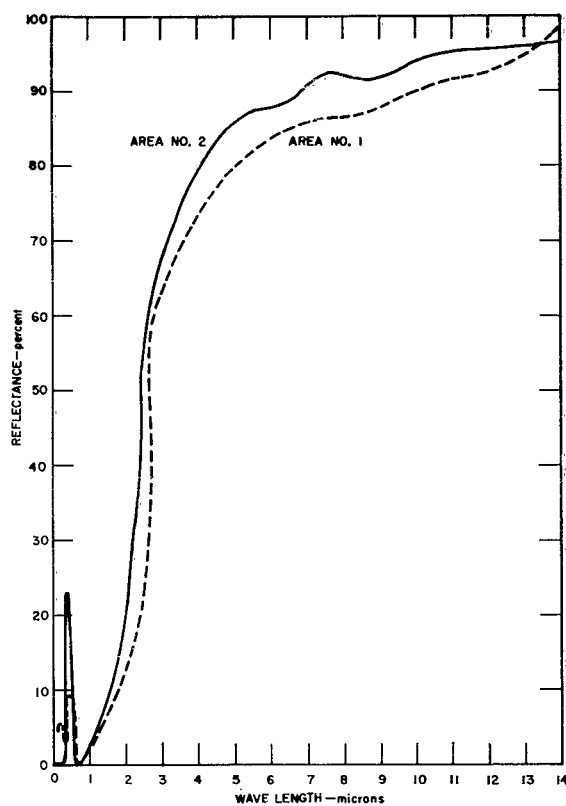


FIG. 37

CUPRIC OXIDE ON ALUMINUM  
BY THE UNGER PROCESS

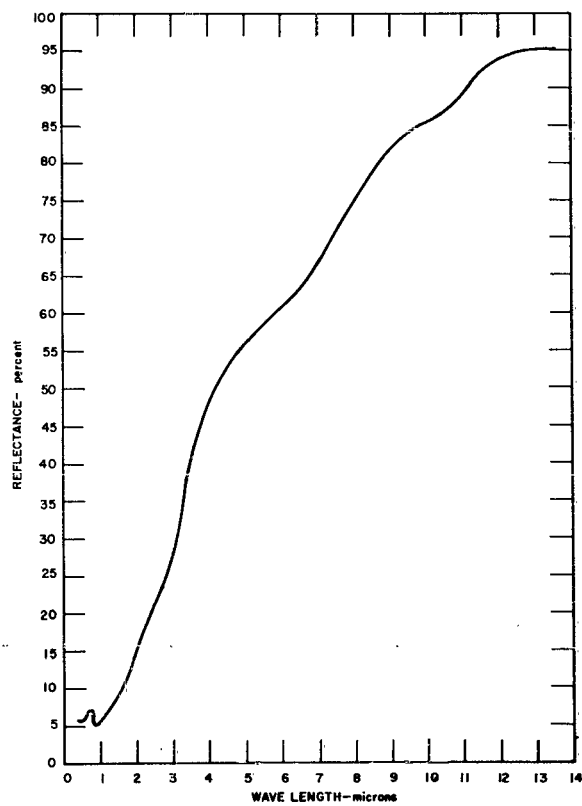


FIG. 38

CUPRIC OXIDE ON ALUMINUM  
PREPARED BY THOMAS A. UNGER

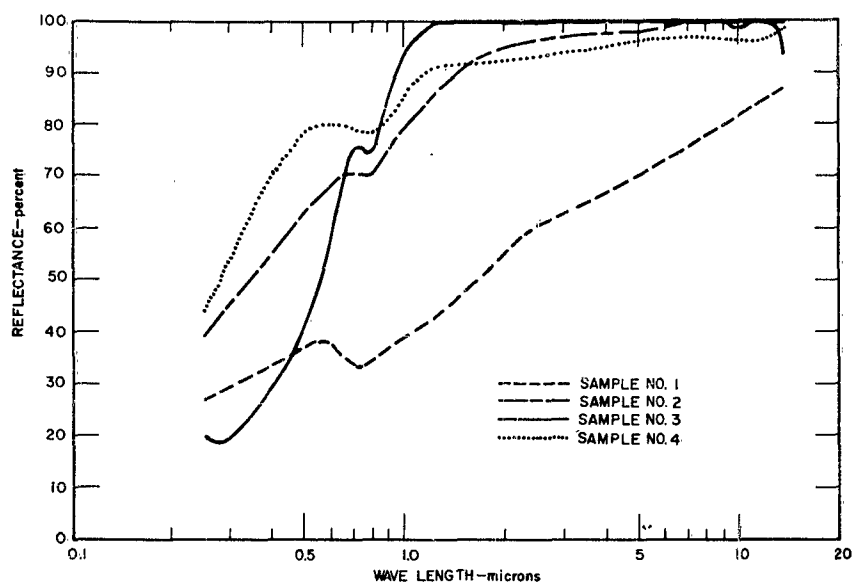


FIG. 39 REFLECTANCE OF UNCOATED ALUMINUM

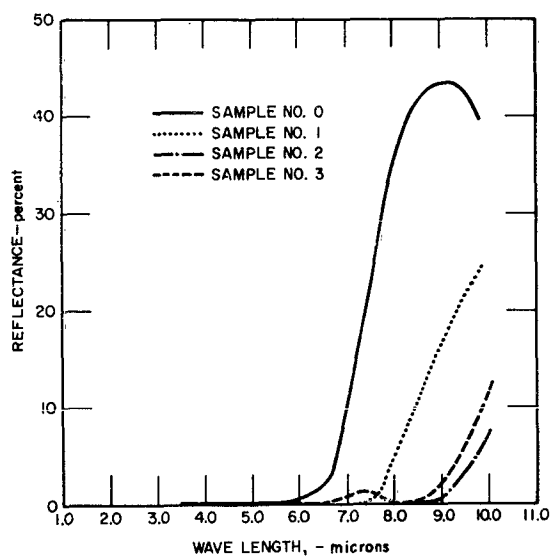


FIG. 40  
SPECTRAL RESPONSE OF CUPRIC OXIDE  
ON COPPER BY THE "EBONOL" PROCESS



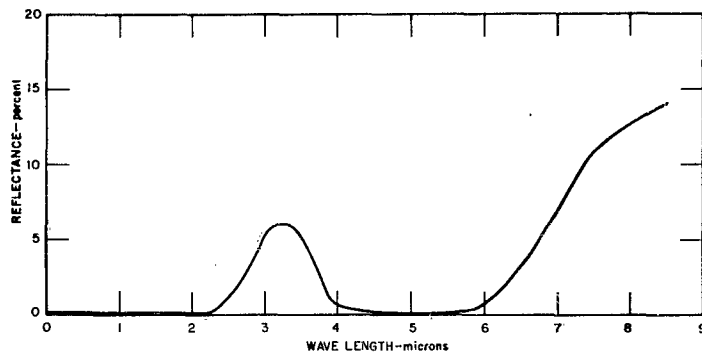


FIG. 41 BLACK NICKEL-IRON OXIDE ON STEEL BY THE "NICKEL PENETRATE" PROCESS

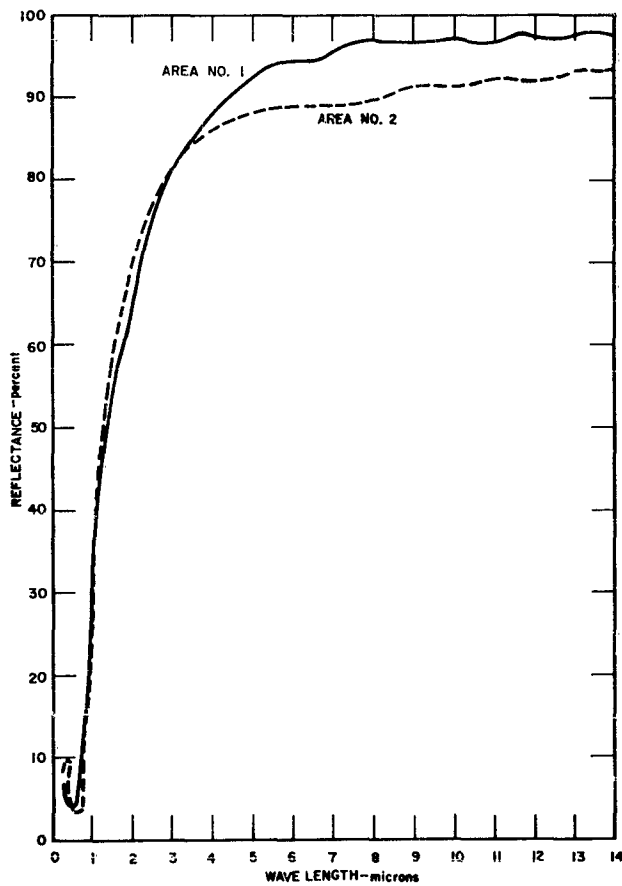


FIG. 42  
BLACK NICKEL ON COPPER

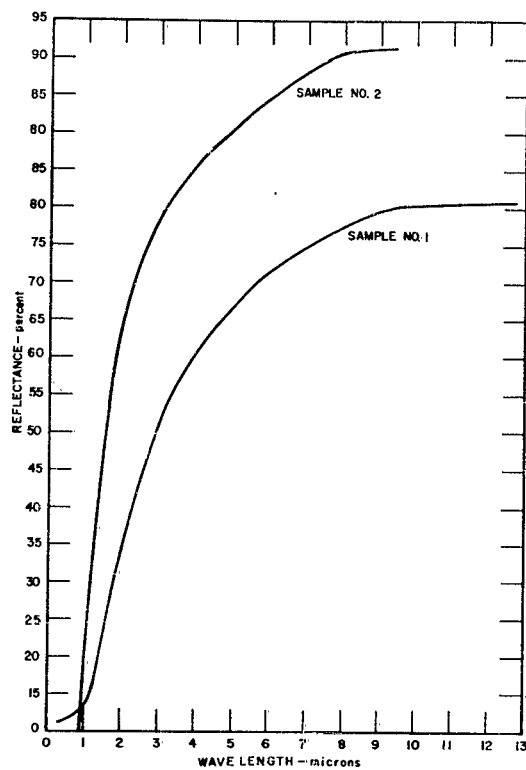


FIG. 43

BLACK NICKEL ON COPPER SHOWING THE  
EXTREMES IN SPECTRAL CHARACTERISTIC  
 $0.35\mu$ - $13\mu$

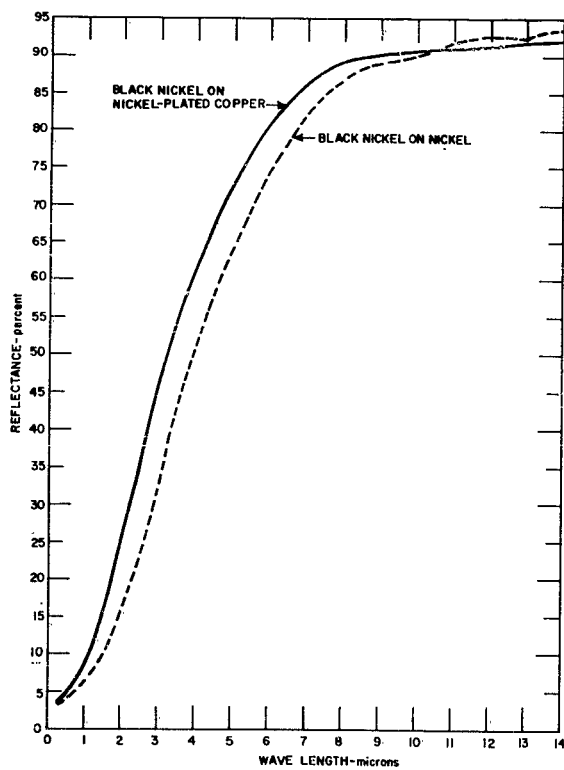


FIG. 44

BLACK NICKEL ON NICKEL AND  
NICKEL-PLATED COPPER

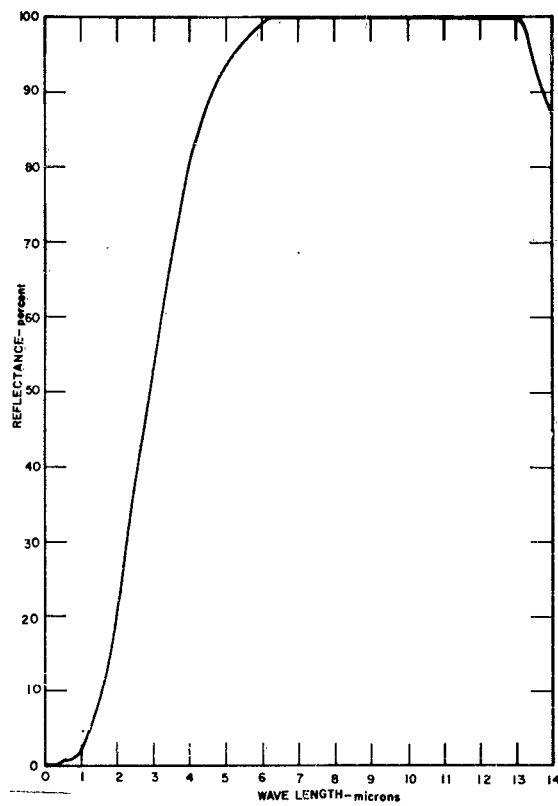


FIG. 45  
PLATINUM BLACK ON PLATINUM

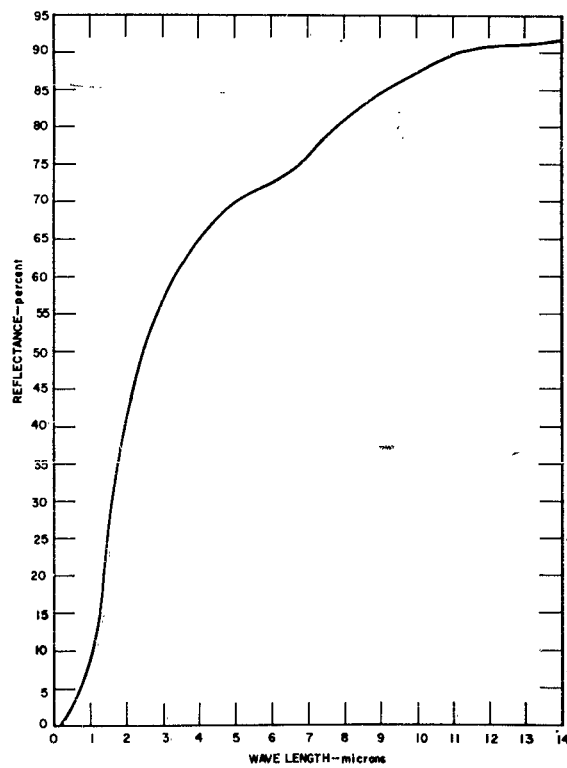


FIG. 46  
CARBON BLACK ON ALUMINUM

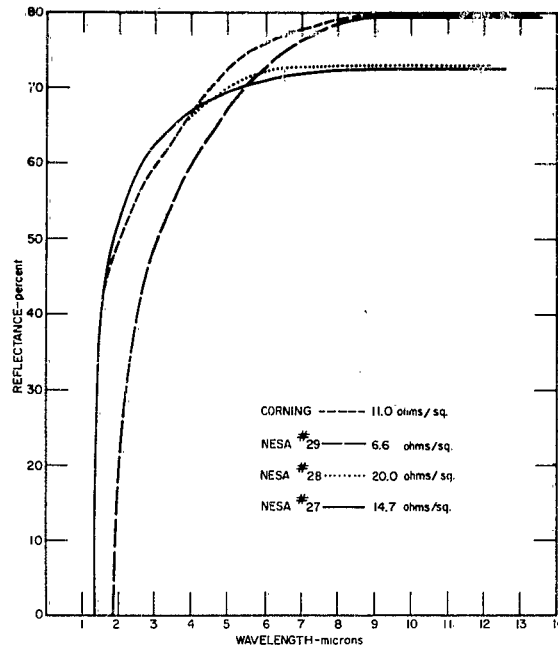


FIG. 47  
REFLECTANCE OF NESA AND  
CORNING GLASS

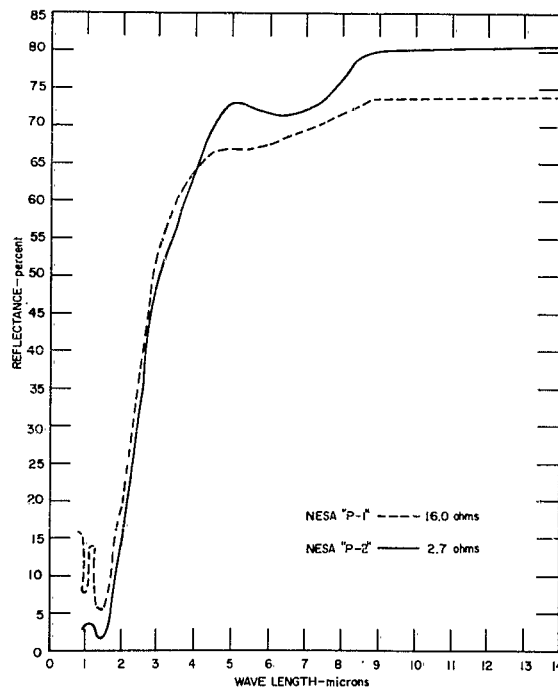


FIG. 48  
REFLECTANCE OF NESA GLASS

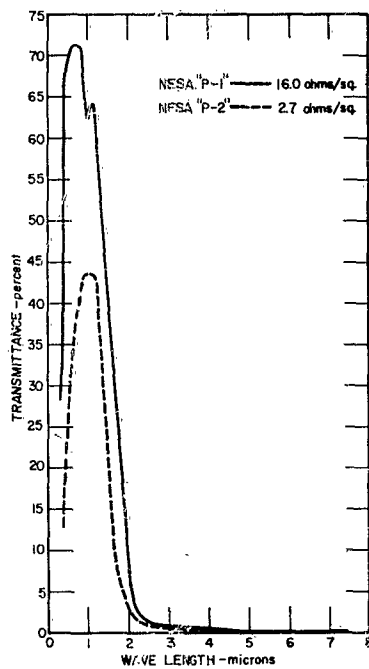


FIG. 49  
TRANSMITTANCE OF NESA GLASS,  
THICKNESS 1/8"

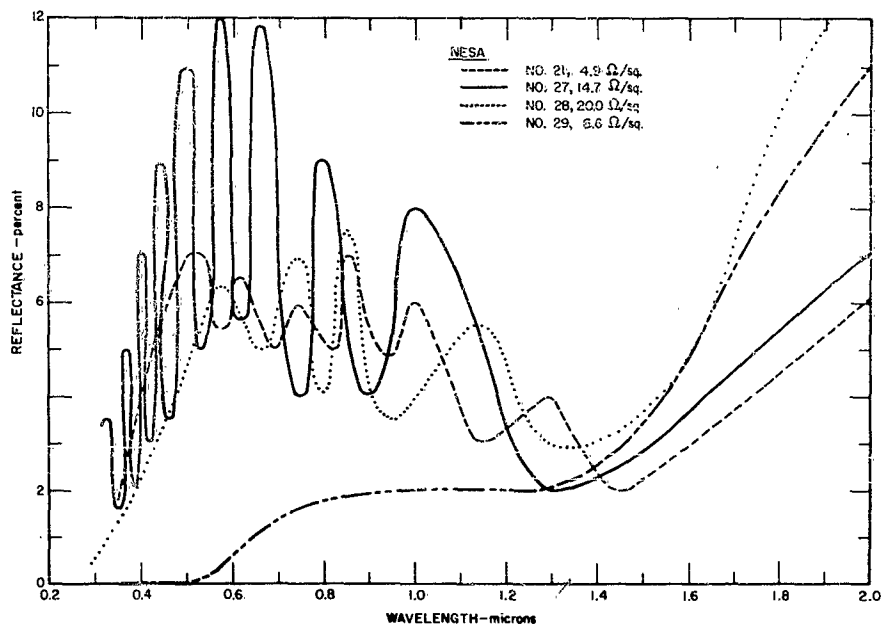


FIG. 50 TRANSPARENT SURFACES

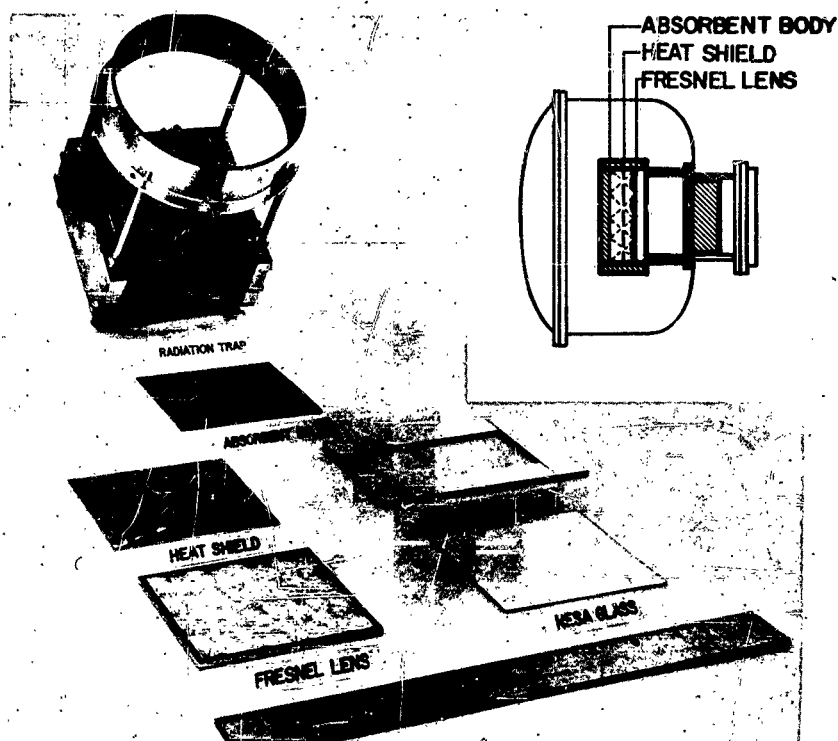


FIG. 51 FRESNEL LENS AND NESA-GLASS RADIATION TRAPS FIT INTO TEST FRAME FOR MOUNTING IN SOLAR TEST FACILITY

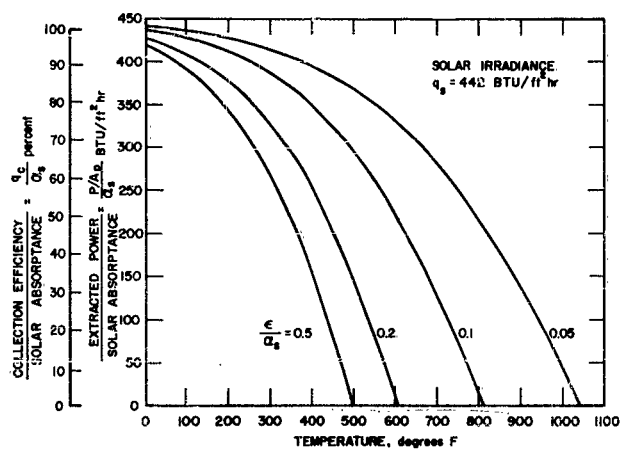
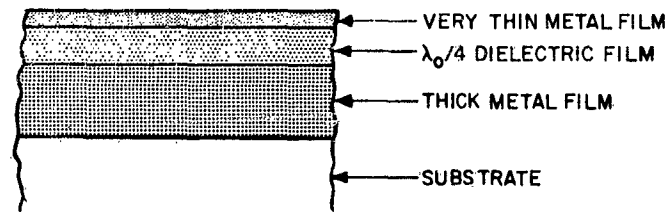
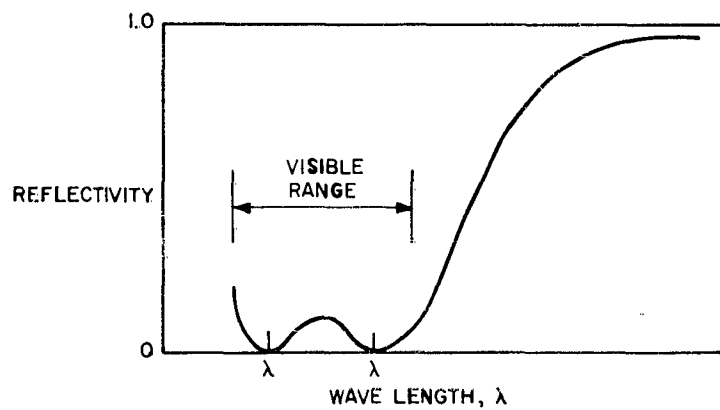


FIG. 52  
SOLAR COLLECTOR CHARACTERISTIC  
FOR SPACE APPLICATION



(a) Typical Design



(b) Typical Reflection Characteristic

FIG. 53 THREE-LAYER INTERFERENCE FILTER

<p>Aeronautical Research Laboratories, Wright-Patterson AFB, O. FEASIBILITY OF A SOLAR ENERGY DEVICE. Part I: FEASIBILITY OF A SOLAR POWERED AIRCRAFT; DESIGN AND PERFORMANCE CONSIDERATIONS by Fred-eric E. Fuller, Electro-Optical Systems, Inc., Pasadena, Calif. 150 p. incl illus. tables. (Project 7116; Task 7116-02) (Contract AF 33(616)-5977) (ARL 62-360, Part I)</p> <p>Unclassified Report</p> <p>The feasibility of a solar powered aircraft is investigated. The configuration reached is a high aspect ratio flying wing with ramjet thrust. A statement is made with respect to</p> <p>( over )</p>	<p>UNCLASSIFIED</p>	<p>Aeronautical Research Laboratories, Wright-Patterson AFB, O. FEASIBILITY OF A SOLAR ENERGY DEVICE. Part I: FEASIBILITY OF A SOLAR POWERED AIRCRAFT; DESIGN AND PERFORMANCE CONSIDERATIONS by Fred-eric E. Fuller, Electro-Optical Systems, Inc., Pasadena, Calif. 150 p. incl illus. tables. (Project 7116; Task 7116-02) (Contract AF 33(616)-5977) (ARL 62-360, Part I)</p> <p>Unclassified Report</p> <p>The feasibility of a solar powered aircraft is investigated. The configuration reached is a high aspect ratio flying wing with ramjet thrust. A statement is made with respect to</p> <p>( over )</p>	<p>UNCLASSIFIED</p>
<p>feasibility with a recommendation of a program for further work. The statement of feasibility is supported by experimental investigation of solar radiation collection and inlet air diffusion and finally by design and performance analyses.</p>	<p>UNCLASSIFIED</p>	<p>feasibility with a recommendation of a program for further work. The statement of feasibility is supported by experimental investigation of solar radiation collection and inlet air diffusion and finally by design and performance analyses.</p>	<p>UNCLASSIFIED</p>